Climate Data Record (CDR) Program

Climate Algorithm Theoretical Basis Document (C-ATBD)

Polar Pathfinder - Extended

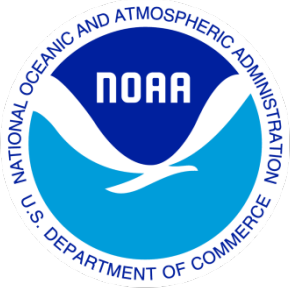

CDR Program Document Number: CDRP-ATBD-0573
Revision 3 / July 19, 2023
Configuration ID#: 01B-24b

REVISION HISTORY

Rev.	Author	DSR No.	Description	Date
1	Jeff Key, NOAA/NESDIS; Xuanji Wang, CIMSS/UW-Madison	DSR-735	Initial Submission to CDR Program	10/02/2015
2	Xuanji Wang, Jeff Key	DSR-1335	Updated algorithm descriptions for changes in APP-x v2.0; added recent updates and improvements appendix	02/07/2019
3	Xuanji Wang, Jeff Key	DSR-1809	Final update for Polar Pathfinder - Extended v3.0	07/19/2023

TABLE of CONTENTS

LIST of FIGURES

LIST of TABLES

1. Introduction

1.1 Purpose

The purpose of this document is to describe the algorithms used in the generation of the Polar Pathfinder - Extended. Polar Pathfinder - Extended is derived from Advanced Very High Resolution Radiometer (AVHRR)/ Visible Infrared Imaging Radiometer Suite (VIIRS) satellite data. It uses the standard Polar Pathfinder Fundamental Climate Data Record (FCDR) product, which was originally developed for the NASA Pathfinder Program in the early 1990s, to estimate surface, cloud, and radiative properties in both Polar Regions from 1982 to the present. There is a separate C-ATBD for the Polar Pathfinder FCDR.

1.2 Definitions

Following is a summary of the symbols used to define the algorithm.

Spectral and directional parameters:

μ = cosine of the solar zenith angle (degree) (1.1)

S_0 = Solar constant (1362 Wm^{-2}) (1.2)

I_0 = The solar radiation flux passing through the ice interior (Wm^{-2}) (1.3)

i_0 = The ice slab transmittance (0∼1, unit less) (1.4)

F_r^{clr} = Clear-sky downward solar radiation flux at the surface (Wm^{-2}) (1.5)

F_r^{cld} = Cloudy-sky downward solar radiation flux at the surface (Wm^{-2}) (1.6)

F_r *and* F_r^{all} = All-sky downward solar radiation flux at the surface (Wm^{-2}) (1.7)

F_l^{up} = Upward longwave radiation flux from the surface (Wm^{-2}) (1.8)

$F_{l,clr}^{dn}$ = Clear-sky downward longwave radiation flux at the surface (Wm^{-2}) (1.9)

F_l^{dn} = All-sky downward longwave radiation flux at the surface (Wm^{-2}) (1.10)

Atmospheric parameters:

T_a = Near-surface air temperature at 2 m above the surface (K) (1.11)

C = Fractional cloud cover (0∼1, unit les) (1.12)

T = Cloud optical depth (unite less) (1.13)

ε_0 and ε^* = The effective sky emissivity (0∼1, unit less) (1.14)

ε_c = Cloud emissivity (0~1, unit less) (1.15)

w = Air mixing ratio (kg/kg) (1.16)

q = Air specific humidity (0~1) (1.17)

w_a = Air mixing ratio at 2 m (kg/kg) (1.18)

w_{sa} = Air mixing ratio at the surface (kg/kg) (1.19)

u = Surface wind speed (ms^{-1}) (1.20)

ρ_a = Air density ($kg\ m^{-3}$) (1.21)

P_a = Surface air pressure (hPa) (1.22)

T_v = Surface air virtual temperature (K) (1.23)

R_{gas} = Gas constant (287.1 $J\ kg^{-1}\ K^{-1}$) (1.24)

C_{pd} = Specific heat of dry air at constant pressure (1004.5 $J\ K^{-1}\ kg^{-1}$) (1.25)

C_p = Specific heat of wet air at constant pressure ($J\ K^{-1}\ kg^{-1}$) (1.26)

f = Air relative humidity (%) (1.27)

Surface parameters:

α_s = Ice/snow surface broadband albedo (0~1, unit less) (1.28)

T_s = Ice/snow skin temperature (K) (1.29)

T_i = Ice interior temperature (K) (1.30)

T_f = Water freezing point temperature (K) (1.31)

σ = Stefan-Boltzmann constant ($5.6696*10^{-8}\ W\ m^{-2}\ deg^{-4}$) (1.32)

h_i = Ice thickness (m) (1.33)

h_s = Snow depth on ice (m) (1.34)

S_w = Sea water salinity (ppt) (1.35)

S_i = Sea ice salinity (ppt) (1.37)

K_s = Snow conductivity ($Wm^{-1}K^{-1}$) (1.38)

K_i = Ice conductivity ($Wm^{-1}K^{-1}$) (1.39)

C_{pv} = Specific heat of water vapor at constant pressure (1952 J K^{-1} kg^{-1}) (1.40)

e_a = Near-surface water vapor pressure (hPa) (1.41)

e_{sa} = Near-surface saturation water vapor pressure (hPa) (1.42)

C_s = Bulk transfer coefficients for turbulent sensible heat flux (0~1) (1.43)

C_e = Bulk transfer coefficients for latent heat flux of evaporation (0~1) (1.44)

F_c = Conductive heat flux within ice slab (Wm^{-2}) (1.45)

1.3 Document Maintenance

Table 1 defines the versions of the Polar Pathfinder - Extended release, the corresponding software package, and the C-ATBD. The Production software package is maintained at NCEI Subversion version control system.

Table 1. Versions of the Polar Pathfinder - Extended CDR product release, the corresponding software package, and the C-ATBD.

Release Date	Product Version	Software Version	C-ATBD Version	Subversion Branch	Remarks
2014-09-26	V01	V01	V1.0	TBD	Initial draft
2015-02-10			V1.1		C-ATBD update
2019-02-07			V2.0		C-ATBD update
2023-07-19			V3.0		C-ATBD update

1.4 Updates, Improvements, and VIIRS addition

Version 2.0 of the Polar Pathfinder - Extended climate data record has a number of important improvements, in addition to the addition of VIIRS. They are briefly described here and reflected in this updated C-ATBD. The improvements include:

- a correction for errors in the Polar Pathfinder FCDR surface type data,
- a residual heat flux estimation for ice thickness,
- a new ice thermodynamic process parameterization scheme, and
- an ice physical dynamic process parameterization.

The cloud cover different between the two versions is about 2.77%, the surface broadband albedo difference is about 0.83%, and the surface skin temperature difference is about 0.38K, mainly due to the correction of the surface type data as detailed in Appendix C. The significant improvement in this version occurred for ice thickness with the difference of about 0.35 m due to the additions of residual heat flux estimation and ice thermo- and physical dynamic processes parameterization schemes as shown in Figure C-4, making ice thickness even more close to the in-situ measurements, especially for the coastal areas along Canadian Archipelago.

These updates and improvements are outlined in sections 3.7.5, 3.7.7-3.7.9, and also illustrated in Appendix C.

The other important update is the addition of VIIRS data, starting from 2012 for AVHRR extension to VIIRS era, detailed and illustrated in Appendix D.

2. Observing Systems Overview

2.1 Products Generated

Polar Pathfinder - Extended contains 20 geophysical variables. All of them have undergone various degrees of validation, though not all of them are considered CDR quality. The variables are (those considered to be of CDR-quality are identified with an asterisk):

- Surface temperature, all-sky, snow, ice, and land*
- Surface albedo, all-sky*
- Sea ice thickness*
- Surface type
- Cloud mask*
- Cloud particle thermodynamic phase
- Cloud optical depth
- Cloud particle effective radius
- Cloud temperature
- Cloud pressure
- Cloud type
- Downwelling shortwave radiation at the surface*
- Downwelling longwave radiation at the surface*
- Upwelling shortwave radiation at the surface*
- Upwelling longwave radiation at the surface*
- Upwelling shortwave radiation at the TOA*
- Upwelling longwave radiation at the TOA*
- Downwelling net shortwave radiation at the TOA
- Shortwave cloud radiative forcing at the surface
- Longwave cloud radiative forcing at the surface

Polar Pathfinder - Extended products are mapped to a 25 km EASE grid at two local solar times: 04:00 and 14:00 for the Arctic, and 02:00 and 14:00 for the Antarctic. Using local solar time rather than standard UTC times provides better information on diurnal differences at all locations.

2.2 Instrument Characteristics

The series of NOAA Polar Orbiting Environmental Satellites (POES) started with TIROS-N (launched in October 1978), and continued with NOAA-A (renamed NOAA-6), NOAA-C (NOAA-7), NOAA-E (NOAA-8), NOAA-F (NOAA-9), NOAA-G (NOAA-10), NOAA-H (NOAA-11), NOAA-D (NOAA-12), NOAA-I (NOAA-13), NOAA-J (NOAA-14), NOAA-K (NOAA-15), NOAA-L (NOAA-16), NOAA-M (NOAA-17), NOAA-N (NOAA-18), MetOp-A, NOAA-N' (NOAA-19), and MetOp-B (Table 2) (Kidwell et al. 1995, 2009). The continuity of the instrument payload onboard the NOAA POES series provide an uninterrupted flow of global environmental information for establishing long-term data sets for climate monitoring. The Joint Polar

Satellite System (JPSS) is the nation's advanced series of polar-orbiting environmental satellites with a new and sophisticated instrument called Visible Infrared Imaging Radiometer Suite (VIIRS) having more channels in place of previous AVHRR. The five satellites scheduled in the fleet are the currently flying NOAA/NASA Suomi National Polar-orbiting Partnership (Suomi NPP) satellite, NOAA-20, previously known as JPSS-1, NOAA-21, previously known as JPSS-2, and the upcoming JPSS-3 and JPSS-4 satellites. Table 2 provides some basic details associated with each of the NOAA POES series.

Table 2: NOAA POES series

Satellite Number	Launch Date	Ascending Node[1]	Descending Node	Service Date[2]
TIROS-N	10/13/78	1500	0300	10/19/78 – 1/30/80
NOAA-6	06/27/79	1930	0730	06/27/79 – 1/16/86
NOAA-7	06/23/81	1430	0230	08/24/81 – 2/01/85
NOAA-8	03/28/83	1930	0730	05/03/83 – 0/31/85
NOAA-9	12/12/84	1420	0220	02/25/85 – 1/07/88
NOAA-10	09/17/86	1930	0730	11/17/86 – 9/16/91
NOAA-11	09/24/88	1340	0140	11/08/88 – 6/16/04
NOAA-12	05/14/91	1930	0730	09/17/91 – 8/10/07
NOAA-14	12/30/94	1340	0140	04/10/95 – 5/23/07
NOAA-15	5/13/98	1930	0730	12/15/98 - present
NOAA-16	09/21/00	1400	0200	03/20/01 - present
NOAA-17	06/24/02	2200	1000	10/15/02 - 4/10/13
NOAA-18	05/20/05	1400	0200	08/30/05 - present
NOAA-19	02/06/09	1400	0200	06/02/09 - present
MetOp A[3]	10/19/06	2130	0930	06/20/07 - present
MetOp B[3]	09/17/12	2130	0930	04/24/13 - present
Suomi NPP	10/28/2011	1330	0130	11/24/11 - present
NOAA-20	11/18/2017	1330	0130	11/29/17 - present
NOAA-21	11/10/2022	1330	0130	12/05/22 - present

[1]An ascending node would imply a northbound Equatorial crossing while a descending node would imply a southbound Equatorial crossing.
[2]Service date is according to Kidwell et al. (1995) and POES Status at Office of Satellite Operations, NESDIS. Information from the latter is used if there is any discrepancy between these two.
[3]Operated by European Space Agency (ESA) and is part of EUMETSAT's Polar System (EPS).

The Advanced Very High Resolution Radiometer (AVHRR) is one of the instruments that fly on all NOAA POES satellites. The AVHRR onboard TIROS-N, NOAA-6, NOAA-8, NOAA-10 and NOAA-12 are AVHRR/1, which has four spectral channels. The AVHRR onboard NOAA-7, NOAA-9, NOAA-11, and NOAA-14 are AVHRR/2, which operates in five spectral channels. A

version of the AVHRR with six spectral channels, AVHRR/3, is used on NOAA-15 and beyond. Channel 3a, with central wavelength at 1.61 μm, operates in the daylight part of the orbit, and channel 3b operates in the night portion of the orbit. Channel 3a and channel 3b cannot operate simultaneously. The specifications of the AVHRR channels are listed in Table 3.

The AVHRR instruments scans in the cross-track direction with a Field Of View (FOV) of ±55.37° from the nadir, with Instantaneous FOV (IFOV) of 1.1 km at nadir (1.3-1.4 milliradians by 1.3-1.4 milliradians for all channels). The AVHRR data in full resolutions are stored and processed in the High Resolution Picture Transmission (HRPT), and Local Area Cover (LAC) outputs, with the LAC being the recorded HRPT. The full resolution data is also processed onboard the satellite into the Global Area Coverage (GAC) data, in which starting with the third sample out of every five samples along the scan line are used to compute one average value, and the data from only every third scan line are processed. As a result, the spatial resolution of the GAC data is 1.1 km by 4.4 km with a 3.3 km gap between pixels across the scan line at nadir. Generally, the GAC data are considered with 4 km resolution. Details of the instruments and data can be found in Kidwell et al. (1995, 2009).

The VIIRS instrument scans in the cross-track direction with a field of view of ±56.28° from nadir. This means that the VIIRS instrument can see a swath of land that is 112.37° wide as it scans across the Earth. The swath width of the VIIRS instrument is 3,060 kilometers, so at an altitude of 824 kilometers, the VIIRS instrument can see a strip of land that is about 1,901.4 miles (3,060 km) wide. The VIIRS instrument has a spatial resolution of 375 meters at nadir in the image-resolution bands (I-bands), and 750 meters in the M band. Similar to the AVHRR GAC data creation, VIIRS data is also processed to create VIIRS GAC data called VGAC data. The VGAC data is created by a team of scientists at NOAA's National Centers for Environmental Information (NCEI). The team first downloads VIIRS data from the NOAA CLASS website. The VIIRS data is then reformatted to match the ISCCP data format. The data is also reprojected to a common coordinate system.

Table 3: Spectral specifications of AVHRR/1, /2, /3, and VIIRS

CH	TIROS-N	NOAA-6,8,10	NOAA-7,9,11,12,14	NOAA-15 and onward	Suomi NPP, NOAA-20, and NOAA-21	GAC/VGAC nadir resolution (km)
	AVHRR/1	AVHRR/1	AVHRR/2	AVHRR/3	VIIRS	4.0
1	0.55-0.90 μm	0.58-0.68 μm	0.58-0.68 μm	0.58-0.68 μm	0.60-0.68 μm	4.0
2	0.725-1.10 μm	0.725-1.10 μm	0.725-1.10 μm	0.725-1.00 μm	0.85-0.88 μm	4.0
3A				1.58-1.64 μm		4.0
3B	3.55-3.93 μm	3.55-3.93 μm	3.55-3.93 μm	3.55-3.93 μm	3.61-3.79 μm	4.0
4	10.50-11.50 μm	10.50-11.50 μm	10.30-11.30 μm	10.30-11.30 μm	10.26-11.26 μm	4.0
5	Ch4 repeated	Ch4 repeated	11.50-12.50 μm	11.50-12.50 μm	11.06-12.96 μm	4.0

The AVHRR GAC data are the inputs to generate the APP CDR. Any variations of the equatorial crossing time (ECT) of a satellite will impact the time series of the data due to

potential diurnal cycles of the data. There have been considerable drifts in the NOAA POES ECT as shown in Figure 1. To keep the data set consistent and the satellite equatorial crossing time as close as to the Solar Local Times (SLT) that the APP is composited at, the following satellites shown in Table 4 with the AVHRR having 5 channels are selected. It should be noted that NOAA-16 has Channel 3A/3B switch, while NOAA-18 has only Channel 3B after August 5, 2005. The 5 AVHRR-like VIIRS channels have been selected from Suomi NPP, NOAA-20, and NOAA-21 satellites to match NOAA-19 AVHRR channels, and also calibrated to NOAA-19 5 AVHRR channels as described later in this document.

Table 4: NOAA satellites used in the Polar Pathfinder FCDR and Polar Pathfinder - Extended CDRs

NOAA satellite	Time range	Note
NOAA-7	01/01/82 – 12/31/84	
NOAA-9	01/01/85 – 11/07/88	
NOAA-11	11/08/88 – 12/31/94	
NOAA-14	01/01/95 – 12/31/00	
NOAA-16	01/01/01 – 08/09/05	NOAA-16 has Channel 3A/3B switching
NOAA-18	08/10/05 – 12/31/2014	On 08/05/05, automatic 3A/3B channel switching was disabled. Channel 3B is permanently on NOAA-18.
NOAA-19	1/1/2015-present	
Suomi NPP, NOAA-20, NOAA-21	1/5/2012-present	

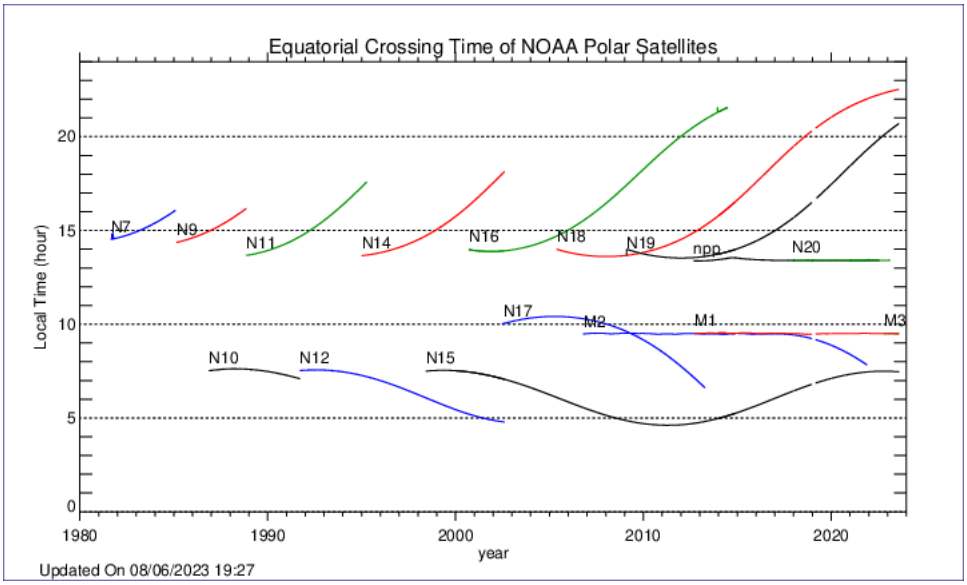

Figure 1: Equatorial Crossing Time (ECT) of NOAA POES (Figure is from www.star.nesdis.noaa.gov/smcd/emb/vci/VH/vh_avhrr_ect.php. The original ECT data are from www.ospo.noaa.gov/Products/ppp/navpage.html.)

3. Algorithm Description

3.1 Algorithm Overview

Polar Pathfinder - Extended processing starts with input from the standard Polar Pathfinder FCDR product (see corresponding Polar Pathfinder FCDR C-ATBD) and ancillary data. Cloud detection is then performed, as the cloud mask feeds into most of the other algorithms. Cloud properties and surface temperature and albedo are then retrieved. Cloud and surface properties are used as input to a parameterization of a radiative transfer model (a neural network) to calculate radiative fluxes and cloud radiative forcing, and also used as input to an ice thickness model called One-dimensional Thermodynamic Ice Model (OTIM) to estimate ice thickness. All variables are then output.

3.2 Processing Outline

The overall processing for Polar Pathfinder - Extended is shown in Figure 2. The blue boxes indicate output parameters.

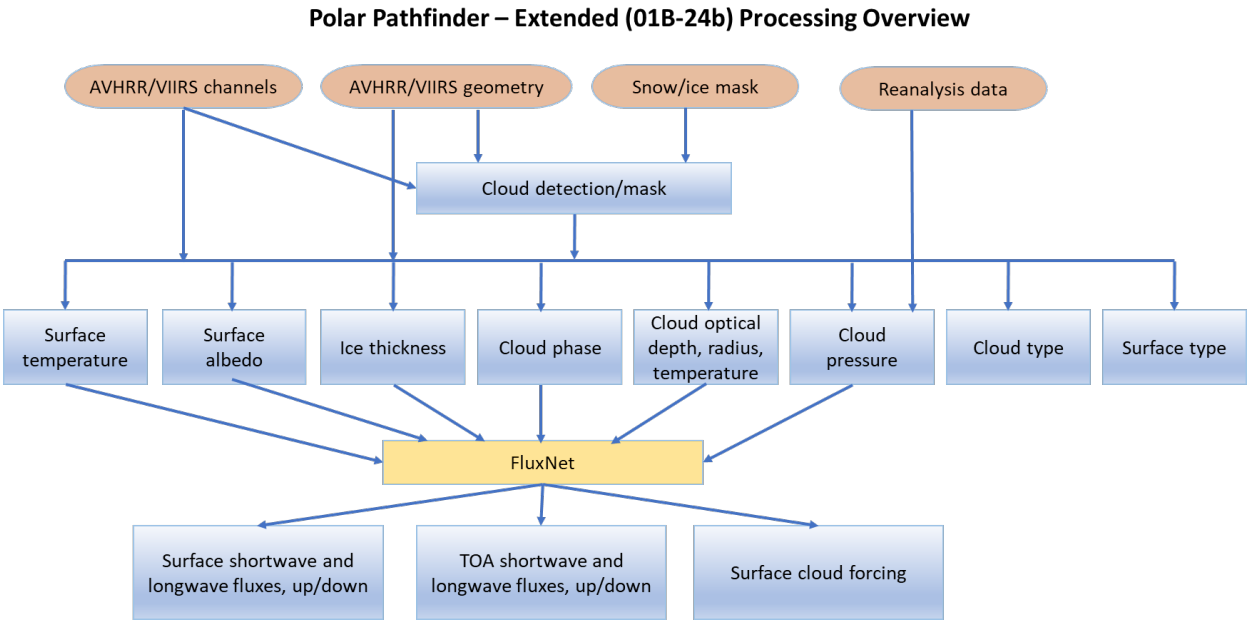

Figure 2: High-level processing flow for the production of Polar Pathfinder - Extended. Blue boxes are output parameters.

3.3 Algorithm Input

3.3.1 Primary Sensor Data

The list below contains the primary parameters data used by the Polar Pathfinder - Extended:

- Channels 1-5 reflectances (channels 1, 2) and brightness temperatures (3-5)
- Sensor viewing zenith angle
- Solar zenith angle
- Relative azimuth angle
- Temperature and humidity profiles, surface winds

All of the above quantities except for the atmospheric data (temperature and humidity profiles, winds) are provided by the standard Polar Pathfinder FCDR, which is the primary input for Polar Pathfinder - Extended processing. Atmospheric data are from a climate reanalysis product (see next section). The Polar Pathfinder FCDR product is described in a separate C-ATBD.

3.3.2 Ancillary Data

The following lists and briefly describes the ancillary data required for Polar Pathfinder - Extended. These are supplied by reanalysis products. Currently the NASA MERRA product is employed.

- Surface air pressure
- Surface air Temperature
- Surface Humidity
- Surface Wind
- Atmospheric temperature profiles
- Atmospheric humidity profiles

3.3.3 Data Merging Strategy

The Polar Pathfinder - Extended uses the Polar Pathfinder FCDR data products that are mapped from 5 km to 25 km EASE grid at two local solar times (LST): 04:00 and 14:00 for the Arctic, and 02:00 and 14:00 for the Antarctic. Using local solar time rather than standard UTC times provides better information on diurnal differences at all locations. The mapping from 5 to 25 km is done by taking every fifth Polar Pathfinder FCDR pixel in the row and column directions. It is subsampling, not an averaging. The final Polar Pathfinder - Extended is also twice daily on the 25 km EASE grid for both poles.

In addition, the NASA Modern Era Retrospective-analysis for Research and Applications (MERRA) (Rienecker et al, 2011) data products are also used in various parts of Polar

Pathfinder - Extended processing. Surface air pressure, surface air temperature, surface air humidity, surface wind speed, and atmospheric temperature and humidity profiles as well as ozone profile data are used. The MERRA daily data are on its native grid of the Finite-Volume dynamic core with a resolution of 2/3 degree longitude by 1/2 degree latitude. The daily MERRA data are re-gridded to APP-x/VPP-x 25 km EASE grid for using with APP-x/VPP-x data to generate Polar Pathfinder - Extended.

3.3.4 Derived Data

The characteristics of the merged data product are given in Table 5.

Table 5. Characteristics of the Polar Pathfinder - Extended dataset.

Name	Twice Daily APP-x/VPP-x
Content	Twice daily suite of surface, cloud, ice thickness, and radiative properties on 25 km x 25 km EASE grid for the Arctic and Antarctica from 1982 to 2017, (currently).
File Format	NetCDF4
Specific Data	appx_s025_2012354_0200_v02r00.nc or vppx_s025_2012354_0200_v02r00.nc (note that "s" stands for the Antarctic, and "n" for the Arctic, "2012354" designates Julian day no. 354 of the year 2012, and "0200" means local solar time of 02:00, they all will change accordingly)
Size	40MB per day, four files per day (two times, two poles), for approximately 500 GB for 36 years.

3.3.5 Forward Models

A radiative transfer model, "Streamer", was used to generate reflectances and brightness temperatures in the AVHRR channels over a broad spectrum of surface, cloud, and atmospheric conditions. The simulated data are used in a number of lookup tables for cloud and surface property retrieval. The model is not part of the algorithms, but rather was an off-line tool.

A neural network implementation of a radiative transfer model is used to compute radiative fluxes and cloud forcing. The model, called "FluxNet", is used because it is approximately 10,000 times faster than a 2-stream radiative transfer model, and is therefore ideal for processing large satellite datasets. See Key and Schweiger (1998) for a detailed description of the model.

A number of separate algorithms, e.g. OTIM, are used to derive the 19 output quantities. They are each described in Section 3. They are collectively contained in a software package call the "Cloud and Surface Parameter Retrieval (CASPR) System for AVHRR (Key 2002). Many algorithms or algorithm components have been published. They are referenced in the appropriate algorithm description sections below.

3.4 Algorithm Output

The following quantities are derived and output:

- Surface temperature, all-sky, snow, ice, and land*
- Surface albedo, all-sky, snow, ice, and land *
- Sea ice thickness*
- Surface type
- Cloud mask*
- Cloud particle thermodynamic phase
- Cloud optical depth
- Cloud particle effective radius
- Cloud temperature
- Cloud pressure
- Cloud type
- Downwelling shortwave radiation at the surface*
- Downwelling longwave radiation at the surface*
- Upwelling shortwave radiation at the surface*
- Upwelling longwave radiation at the surface*
- Upwelling shortwave radiation at the TOA*
- Upwelling longwave radiation at the TOA*
- Downwelling net shortwave radiation at the TOA
- Shortwave cloud radiative forcing at the surface
- Longwave cloud radiative forcing at the surface

Those marked with an asterisk (*) are considered to be of CDR-quality based on validation studies.

3.5 Theoretical Description: Surface Temperature

3.5.1 Physical and Mathematical Description

For the retrieval of clear sky surface temperature, a simple regression model is used to correct for atmospheric attenuation. For high-latitude ocean and snow-covered land we use the equation

$$T_S = a + bT_4 + c(T_4 - T_5) + d[(T_4 - T_5)(\sec\theta - 1)]$$

where T_S is the surface temperature, T_4 and T_5 are the satellite measured brightness temperatures in channels 4 and 5, θ is the sensor scan angle, and *a*, *b, c,* and *d* are regression coefficients. To determine the empirical relationship above, radiosonde data from drifting ice and land stations in the Arctic and Antarctic were used with a radiative transfer model to simulate the sensor brightness temperatures.

The regression method of relating modeled brightness temperatures to surface temperature was also used for a snow-free land algorithm. But because spectral emissivities for vegetation in channels 4 and 5 are variable and generally unknown, they are variables in the regression. Additionally, scan angle is not a variable in the regression since its dependence on angular emissivity is unknown. The regression equation for snow-free land has the form:

$$T_S = a + bT_4 + cT_5 + d\varepsilon_4 + e\varepsilon_5$$

where ε_i is the emissivity in channel *i*. The surface temperature retrieval methods for both sea ice/snow and snow-free land are described in detail in Key, et al. (1997).

The cloudy sky surface temperature calculation is based on empirical (linear regression) relationships between the clear sky temperature, wind speed, and solar zenith angle (daytime), determined using surface observations from the SHEBA (Surface HEat Budget of the Arctic) experiment. **It applies only to sea ice.** The clear sky surface temperatures are interpolated to cloudy pixels with a kriging function, and then the cloudy sky temperatures are estimated from the clear temperatures and one or two other variables, depending on the time of year. For the polar night and before the melt season (November through April) there are two equations:

solar zenith angle 80 degrees or more: $T_{cld} = a1 + b1*T_{clr} + c1*u_{cld}$
solar zenith angle less than 80 degrees: $T_{cld} = a2 + b2*T_{clr} + c2*\cos(Z) + d2*u_{cld}$

During the warm season, defined as May-September with the surface temperature greater than 255K, the following apply:

solar zenith angle less than 90 degrees: $T_{cld} = a3 + b3*T_{clr} + c3*\cos(Z) + d3*t_{cld}$
or if t_{cld} is not known: $T_{cld} = a3 + b3*T_{clr} + c3*\cos(Z)$
nighttime only: $T_{cld} = a4 + b4*T_{clr} + c4*u_{cld}$

where T_{cld} is the cloudy sky surface temperature (K), T_{clr} is the clear sky surface temperature (K), u_{cld} is the cloudy sky wind speed (m s^{-1}), Z is the solar zenith angle, t_{cld} is the number of hours that it has been cloudy. Because t_{cld} will not generally be known to better than six hours with satellite data, the alternate equation is used.

3.5.2 Numerical Strategy

Not applicable.

3.5.3 Calculations

AVHRR/VIIRS reflectances, brightness temperatures, and viewing geometry are used in the application of the equations above. Surface temperature is the output.

3.5.4 Look-Up Table Description

There are no lookup tables in the surface temperature algorithm.

3.5.5 Parameterization

There are no parameterizations beyond those that are described above.

3.6 Theoretical Description: Surface Albedo

3.6.1 Physical and Mathematical Description

The retrieval of surface albedo involves four steps:

1. Convert channels 1 and 2 narrowband reflectances to a broadband reflectance.
2. Correct the top-of-atmosphere (TOA) broadband reflectance for anisotropy.
3. Convert the TOA broadband albedo to a surface broadband albedo.
4. Adjust the surface clear sky broadband albedo for the effects of cloud cover in cloudy pixels (over snow/ice only).

The general methodology described by steps 1-3 was used by Csiszar and Gutman (1999) for global land studies. Relationships for land and ocean were developed independent of that study, and methods for snow/ice and ocean were added. DeAbreu et al. (1994), Lindsay and Rothrock (1994), and earlier versions of this algorithm used a procedure where the anisotropic reflectance correction was applied to channels 1 and 2, an atmospheric correction was done on those channels, then narrowband albedos were converted to broadband. That procedure tended to overestimate the albedo of snow/ice.

Terminology for albedo varies. Here it is important to distinguish between "inherent" and “apparent” surface albedos. The inherent albedo is the “true”, no-atmosphere albedo of the surface and is independent of changes in atmospheric conditions. It is also called the “black-sky” albedo or the directional hemispherical reflectance. The apparent albedo - also called the “blue-sky” albedo - is what would be measured by up- and down-

looking radiometers in the field. It varies with atmospheric conditions. Both vary with solar zenith angle and are directional in that regard. The difference between them is very small for the ocean but can be large for vegetation and snow. Figure 3 gives an example of the difference between these two albedo types for ocean, vegetation, and snow. As the figure illustrates, differences can be up to 10%. **Polar Pathfinder - Extended contains the apparent, or blue-sky albedo**. After the apparent albedo is calculated it is adjusted for cloud cover. The complete procedure is detailed in Key et al. (2001).

The first step is to convert the narrowband reflectances in AVHRR channels 1 and 2 to a TOA broadband reflectance. This is necessary because the anisotropic reflectance correction in step 2 requires a broadband reflectance. The narrow-to-broadband conversion takes the form:

$$\rho_{toa} = a + b\rho_{1,\,toa} + c\rho_{2,\,toa}$$

where $\rho_{1,toa}$ is the channel 1 reflectance, $\rho_{2,toa}$ is the channel 2 reflectance, ρ_{toa} is the broadband TOA reflectance, and *a*, *b*, and *c* are regression coefficients. To develop the regression relationship *Streamer* (Key and Schweiger, 1998) was used to simulate the TOA reflectances over a broad range of viewing and illumination angles, atmospheric conditions (aerosol optical depth and water vapor amount), and surface types and albedos. Separate sets of coefficients were determined for snow/ice and snow-free land (generic vegetation in *Streamer*). For open ocean the broadband reflectance is set to the channel 1 reflectance.

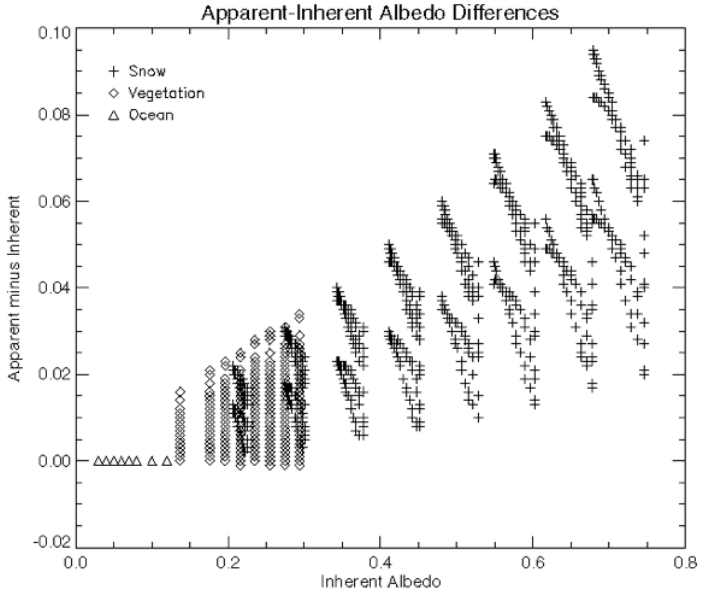

Figure 3. The difference between the apparent (atmosphere dependent) and inherent surface albedos of unfrozen ocean, snow-free land (vegetation), and snow. Data are

from radiative transfer model calculations (Streamer) for two precipitable water amounts (0.5 and 5 g cm^{-2}), two aerosol optical depths (0.05 and 0.5), and solar zenith angles from 0 to 87 degrees.

The next step is to correct for the dependence of the sun-satellite-surface geometry on reflectance. This is done with data presented in Suttles et al. (1988). That study used ERBE and GOES data to determine TOA anisotropic reflectance factors (ARF) for the broad shortwave band over various surfaces. It updates the earlier work of Taylor and Stowe (1984). Both the ERBE and GOES instruments measure radiances and are therefore a function of viewing and illumination geometry. To convert the directional reflectance to albedo, the ERBE/GOES ARFs are used:

$$\alpha_{toa} = \frac{\rho_{toa}}{f}$$

where ρ_{toa} is the reflectance observed at the sensor (simulated by *Streamer* in step 1), *f* is the anisotropic reflectance factor, and α_{toa} is the TOA albedo, which is only a function of solar zenith angle. A trilinear interpolation routine was used to retrieve f as a function of satellite zenith angle, solar zenith angle, and the relative azimuth angle.

Next, the broadband, clear sky, apparent surface albedo is estimated with a regression relationship of the form:

$$\alpha_{toa} = a + b\alpha_s$$

where α_s is the surface reflectance, and *a* and *b* are a function of water vapor, aerosol amount, and solar zenith angle. There is a different set of coefficients for each solar zenith angle, aerosol optical depth, and precipitable water bin. This method was used by Koepke (1989) for AVHRR channels 1 and 2 separately. Here the coefficients were determined with *Streamer* for a variety of surface and atmospheric conditions and illumination angles. Viewing geometry is not important in this step. Snow/ice and vegetation surface types were used in the radiative transfer calculations, and the regression coefficients are based on the combined surface type data. For ocean surface albedo a simpler approach is used:

$$\alpha_S = a + b\alpha_{toa} + c\cos Z + dPW + e\tau_{aer}$$

where *PW* is precipitable water (cm), τ_{aer} is aerosol visible optical depth (unitless), *Z* is the solar zenith angle, and *a, b, c, d,* and *e* are regression coefficient based on modeled albedos.

The surface albedo under clear and cloudy conditions can be very different. This is illustrated in Figure 4, which shows the change in surface albedo with increasing optical depth. The values are fractional change, where 1 means no difference between clear and cloudy values. While the cloudy sky albedo can be 15% more or less than the clear sky value for both surface types, it is consistently higher for snow, with a mean difference near 10%. For vegetation, the cloudy albedo may be higher or lower, so that the mean difference is very small. For this reason, only the snow albedo is adjusted for cloud cover.

The albedo of cloudy pixels is determined using the clear sky albedo, interpolated to fill in the entire image, and adjusted by the cloud optical depth and the solar zenith angle. This conversion is also based on model calculations, where *Streamer* was used to compute upwelling and downwelling fluxes for a snow/ice surface over a range of cloud and atmospheric conditions. The empirical relationship between the clear sky broadband albedo, cloud optical depth, and the cloudy sky broadband surface albedo is

$$\alpha_{s,\,cld} = a + b\alpha_{s,\,clr} + c\ln(\tau + 1) + d\cos Z$$

where τ is the cloud visible optical depth (unitless), $\alpha_{s,clr}$ is the clear sky **apparent** albedo (see above), Z is the solar zenith angle, and a, b, and c are regression coefficients. As aerosol and water vapor amounts are not explicit in this relationship, this adjustment assumes that their effect on the surface albedo is small relative to that of clouds. Note, however, that this adjustment is to the apparent albedo, which is a function of aerosol and water vapor amounts. No distinction is made between water and ice clouds, although both were included in the model data for the regression analysis. This relationship works best when the snow surface is bright ($\alpha > 0.5$) and clouds have small to moderately large optical depths ($1 < \tau < 50$). For snow-free land and open water the cloudy sky broadband albedo is set to the clear sky broadband value.

In the model calculations of steps 1, 3, and 4, the variable ranges were as follows: solar zenith angle: 0 - 87 degrees, aerosol visible optical depth: 0.05 - 0.5, precipitable water: 0.5 – 5 g m^{-3}, snow visible albedo: 0.5 - 0.99, and vegetation visible albedo: 0.07 - 0.15. In all cases ozone amount was prescribed 325 Dobson units.

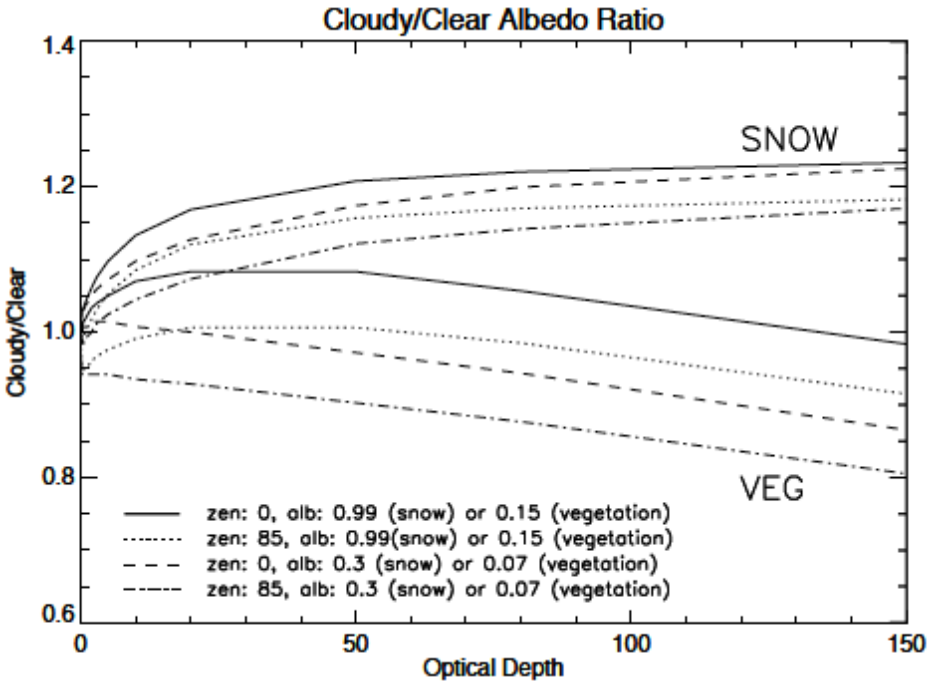

Figure 4. Differences between clear and cloudy surface albedos expressed as a fraction (cloudy divided by clear; 1 means no difference) for snow (top set of lines) and generic vegetation (bottom set), given as a function of cloud optical depth. Results were generated with a radiative transfer model for water and ice cloud under varying atmospheric conditions. The lines are for different solar zenith angles (0 and 85 degrees) and visible surface albedos (0.3 and 0.99 for snow; 0.07 and 0.15 for vegetation.

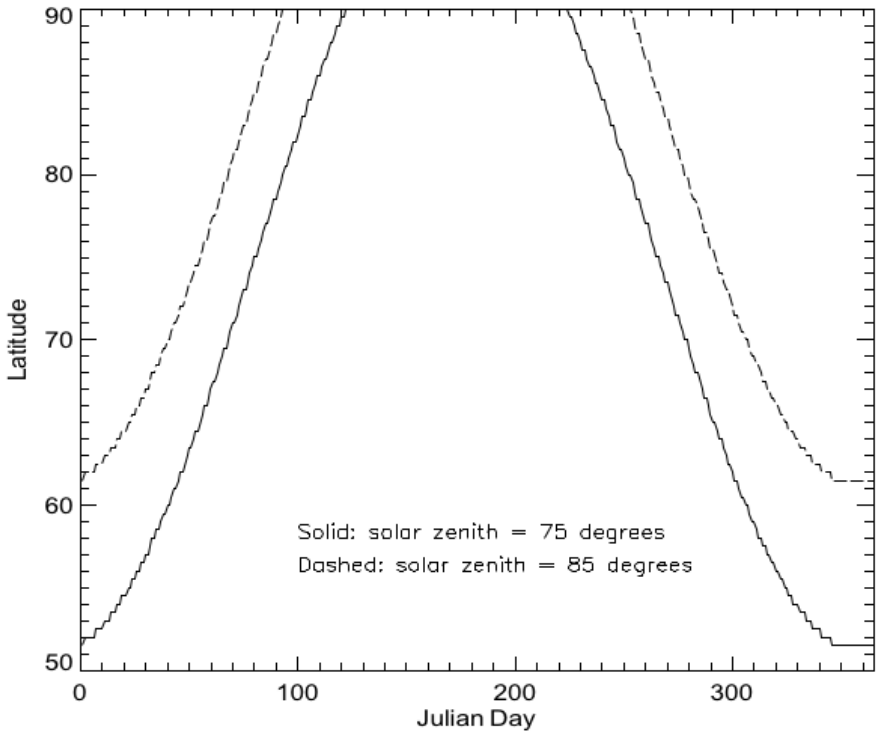

Figure 5. Latitudes and times of the year where zenith angles greater than 85 degrees and greater than 75 degrees are experienced at solar noon. All latitudes poleward of those shown will have solar zenith angles larger than 85 or 75 degrees. The 85 degree line is relevant to albedo retrievals; the 75 degree line is relevant to cloud optical depth retrievals.

3.6.2 Numerical Strategy

Not applicable.

3.6.3 Calculations

AVHRR/VIIRS reflectances, viewing and illumination geometry, and cloud optical depth are used in the application of the equations above. Broadband, all-sky surface albedo is the output.

3.6.4 Look-Up Table Description

There are no look-up tables in the albedo algorithm.

3.6.5 Parameterization

Anisotropic reflectance at the top of the atmosphere was parameterized by Suttles et al. (1988) and used as described above.

3.7 Theoretical Description: Ice Thickness

3.7.1 Physical and Mathematical Description

The ice thickness retrieval will use the OTIM (Wang et al, 2010). The OTIM is based on the surface energy balance at thermo-equilibrium and contains all components of the surface energy budget to estimate sea and lake ice thickness up to 5 meters, though the uncertainty increases for very thick ice.

The advantage of this approach is that there is a solid physical foundation with all components of surface energy budget considered. It's capable of retrieving daytime and nighttime sea and lake ice thickness under both clear and cloudy sky conditions. Very computationally efficient compared to more complex models such as the Climate System Model (CSM) and Sea Ice Model (CSIM). Its sole objective of retrieving ice thickness makes it easy to implement with the application of satellite products, flexible, fast and easy to maintain and improve later with more and accurate satellite derived products like radiative fluxes, ice surface temperature and snow depth on ice.

The disadvantage of this approach is that the accuracy of input parameters, e.g., snow depth, surface air humidity, temperature, and wind, can significantly impact the accuracy of ice thickness estimates. Daytime retrieval is sensitive to ice and snow optical properties associated with ice type and thickness, and is less reliable than nighttime retrievals.

The One-dimensional Thermodynamic Ice Model (OTIM) developed by Wang et al (2010) was recently improved and evolved into a physical-statistical hybrid model by the parameterizations of residual heat flux and ice physical-thermodynamic processes. It is applied to the APP/VPP data to generate all-sky sea and lake ice thickness products twice daily for the Arctic and the Antarctic. The current ice thickness algorithm, i.e. OTIM, has the ability to estimate sea and lake ice thickness up to 5 meters under both clear and cloudy conditions for both day and night.

Ice thickness is produced for each pixel that is identified as being ice covered. There are no direct AVHRR/VIIRS channel data related to the algorithm for ice thickness retrieval with the OTIM. The OTIM actually relies on some other retrieved products from APP-x/VPP-x as well as built-in parameterization schemes such as for radiation and residual heat flux calculations. The algorithm operation is shown graphically in Figure 6.

The OTIM relies on the accuracy of the other products and parameterization schemes such as the cloud mask, ice surface temperature, ice surface albedo, and radiation fluxes. The performance of the ice thickness algorithm is therefore sensitive to the accuracy of the APP-

x/VPP-x retrieved products. We will detail the required input parameters and current validations in the following sections, and the algorithm sensitivity to input uncertainties.

Physical and statistical approaches are employed to estimate sea and lake ice thickness. In this document, the One-dimensional Thermodynamic Ice Model (OTIM) (Wang et al, 2010) based on the surface energy budget, containing all components of the surface energy budget has been developed to estimate sea and lake ice thickness. It inevitably involves parameterizations and assumptions of the sea and lake ice and associated snow characteristics, such as ice and snow conductivities, densities, and transmittances.

A slab model proposed by Maykut and Untersteiner (1971) is used here as a prototype model, the equation for energy conservation at the top surface (ice or snow) is

$$(1-\alpha_s)(1-i_0)F_r - F_l^{up} + F_l^{dn} + F_s + F_e + F_c - F_a = 0 \qquad (3.7.1)$$

where α_s is ice surface broadband albedo where ice may be covered with a layer of snow, F_r is downward solar radiation flux at the surface, i_0 is ice slab transmittance, F_l^{up} is upward longwave radiation flux from the surface, F_l^{dn} is downward longwave radiation flux from the atmosphere towards the surface, F_s is turbulent sensible heat flux at the surface, F_e is turbulent latent heat flux at the surface, F_c is conductive heat flux within the ice slab, F_a is residual heat flux that could be caused by ice melting and/or heat advection in ice. By the definitions of the terms in the equation (3.7.1), α_s, F_r, i_0, F_l^{up}, F_l^{dn} should be always positive, and F_s, F_e, and F_c would be positive or negative in terms of the operational symbols used in the equation (3.7.1), and F_a is zero in the absence of any phase change and heat advection in ice. The details of each term will be addressed in the following subsections.

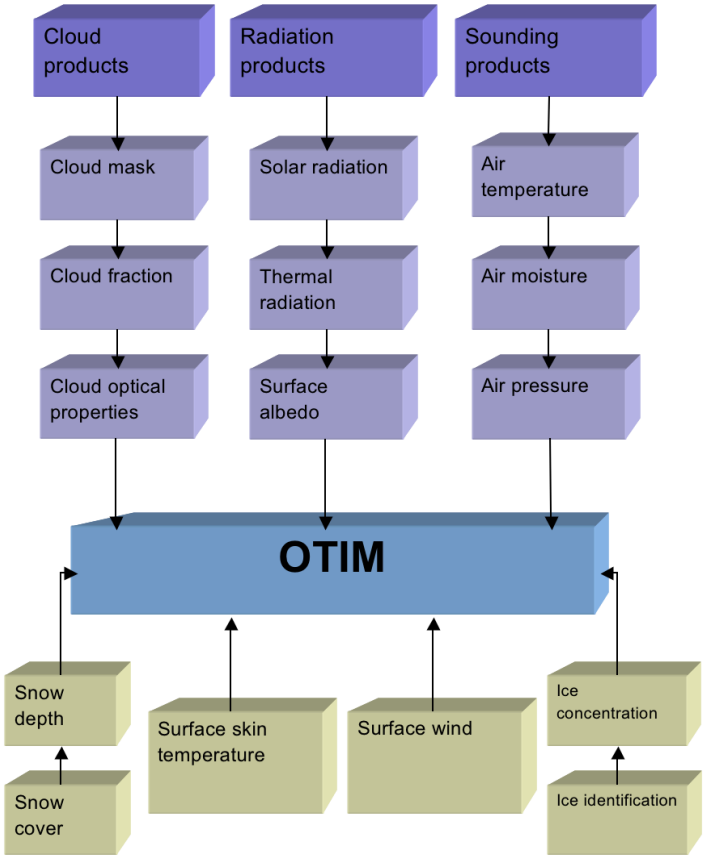

Figure 6. High-level flowchart of the OTIM illustrating the main processing sections.

3.7.2 Numerical Strategy

The ice thickness output could have missing values if the input APP-x/VPP-x data and/or MERRA data have missing and/or bad values for a pixel.

3.7.3 Calculations

The sea ice thickness (SIT) CDR production includes the following steps:

1) Run the Cloud and Surface Parameter Retrieval (CASPR) system (Key, 2002) package with the input APP/VPP data and MERRA data to generate twice daily APP-x/VPP-x data products on 25km EASE grid.

2) Input APP-x/VPP-x data products to the OTIM main routine. This can be done at the same time of processing Polar Pathfinder FCDR data for Polar Pathfinder - Extended data products.

3) Generate ice thickness.

3.7.4 Look-Up Table Description

Surface Broadband Albedo Estimation Coefficients

Origin	Thomas C. Grenfell (1979)
Construction	3 x 2 x 4 in ASCII, 4 sets of coefficients, each is 3 x 2 array.
Usage	Define surface broadband albedo model in case it's unknown.

Ice Slab Transmittance Estimation Coefficients

Origin	Thomas C. Grenfell (1979)
Construction	3 x 2 x 4 in ASCII, 4 sets of coefficients, each is 3 x 2 array.
Usage	Define ice slab transmittance model in case it's unknown.

3.7.5 Surface Type Correction

The Polar Pathfinder FCDR data product is the main input for Polar Pathfinder - Extended data processing. A surface type (mask) is included in the Polar Pathfinder FCDR output. For years prior to 1995, the surface type data are generated with the 25 km EASE Grid data from the daily averaged Polar Gridded Brightness Temperature of Special Sensor Microwave/Imagers (SSM/I) onboard the Nimbus-7 Scanning Multichannel Microwave Radiometer (SMMR) and the Defense Meteorological Satellite Program (DMSP). After the year 1995, the surface type data are from the Near-Real-Time SSM/I-SSMIS EASE Grid Daily Global Ice Concentration and Snow Extent, Version 4 (Nolin et al. 1998).

In some cases, atmospheric effects such as clouds, temperature inversions, and wind roughening of the ocean cause false ice concentration retrievals over the Arctic Ocean. Some areas will appear as incorrectly mapped areas of sea ice, and/or vice versa in the surface typing. The incorrect surface typing will affect Polar Pathfinder - Extended cloud detection and everything else that depends upon it, such as surface albedo and temperature. It is therefore very important to correct the surface type when and where possible. For daytime cases, the surface is classified as ice or snow if AVHRR channel 1 reflectance is greater than 0.30 under clear sky conditions over water and land areas, respectively. For nighttime cases, if the surface temperature is greater than 273 K, the ocean surface should be ice free. In addition, if the daytime surface temperature is less than 268 K, the ocean surface should be ice covered.

3.7.6 Radiation and Salinity Parameterizations

1) Solar Radiation at the Surface

In daytime, surface broadband albedo and ice slab transmittance play important role on the incoming solar radiation for the thermo-equilibrium state at the surface. If the OTIM hybrid mode is not called or used, and the surface albedo and ice slab transmittance are unknown, then they can be estimated using the methods developed by Thomas C. Grenfell (1979):

$$\alpha_s = 1 - A\ exp(-Bh) - C\ exp(-Dh)$$

$$i_0 = A\ exp(-Bh) + C\ exp(-Dh)$$

where *A, B, C, and D* are coefficients, respectively, and *h* is ice thickness or snow depth if ice is covered by snow. When the OTIM mode sets to using hybrid mode, which is recommended, those two formulas will not be used, and surface albedo and ice transmittance need not be known.

2) Upward Longwave Radiation from the Surface:

$$F_l^{up} = \varepsilon\ \sigma\ T_s^4$$

where ε is longwave emissivity of ice or snow surface, σ = 5.6696*10-8 W m^{-2} deg^{-4} is the Stefan-Boltzmann constant. Here ice emissivity of 0.988 is used because snow emissivity at 0^o look angle is 0.995, very close to the value of 0.987 for ice and 0.988 for water (Rees, 1993).

3) Downward Longwave Radiation towards the Surface:

$$F_{l,clr}^{dn} = \sigma\ T_a^4\ (8.733*10^{-3}\ T_a 0.788)$$

$$F_l^{dn} = F_{l,clr}^{dn}\ (1 + 0.26\ c)$$

where Eq. (3.4) was developed by Ohmura (1981), and Eq. (3.5) by Jacobs (1978), and *c* is cloud fractional cover.

4) Downward Solar Radiation towards the Surface (Bennett, 1982):

$$F_r^{clr} = 0.72\ S_0\ \mu$$

$$F_r^{all} = F_r^{clr}\ (1 - 0.52\ c)$$

where *c* is cloud fractional cover.

5) Sea Ice Salinity:

$$S_i = 2.619 + 1.472/h_i, \quad for\ 0.10\ m \le h_i \le 5.0\ m$$

where h_i is sea ice thickness. This is based on the work done by Jin et al (1994) and Kovacs (1996).

3.7.7 Residual Heat Flux Estimation for Sea Ice Thickness

The largest uncertainty in the estimation of ice thickness for daytime retrievals is that the unknown residual heat flux F_a in equation (3.7.1) is not zero. It is, in fact, large enough to be considered as an important term in OTIM. Physically, F_a should be related to the surface and atmospheric conditions such as surface skin temperature, broadband albedo, air temperature, air humidity, surface wind speed, horizontal heat advection within ice and snow, and surface solar radiation during the daytime. Here we set $F_A = F_a - (1-\alpha_s)(1-i_0)F_r$ as a function of some surface and atmospheric variables including the cosine and sine of ice melting and freezing days (cosmel, sinmel, cosfre, sinfre; see below), snow depth (h_s), cosine of the solar zenith angle (cossol), surface downward longwave radiative flux (F_l^{dn}), and surface upward longwave radiative flux (F_l^{up}), surface downward solar radiative flux (F_r), surface sensible heat flux (F_s), and surface latent heat flux (F_e).

A regression equation for the calculation of the residual heat flux was developed using in-situ measurements of ice thickness from the surface, submarine, buoy, mooring, and field campaigns to calculate F_A first using OTIM, and then using a stepwise regress technique for the F_A predictand calculation with the above-mentioned variables as predictors. There are four regression equations for estimating F_A for four conditions: daytime with and without profile data, and nighttime with and without profile data.

1) Daytime case with profile data

$$F_A = 54.65025 - 4.781119*cossol - 5.432518*cosfre + 4.144333*sinfre -174.5416*h_s + 2.610399*F_r + 1.034201*F_l^{dn} - 1.107273*F_l^{up} + 0.9960775*F_s + 1.054412*F_e$$

2) Daytime case without profile data

$$F_A = 18.82845 + 3.701520*sinmel - 6.441864*cosfre - 135.1727*h_s -3.261515*F_r - 0.03905455*F_l^{dn} - 0.4591621*F_s - 1.368342*F_e$$

3) Nighttime case with profile data

$$F_A = 75.38058 + 13.53732*cossol - 58.50422*sinsol - 3.827107*cosmel + 9.249864*h_s + 1.052007*F_l^{dn} - 1.098335*F_l^{up} + 1.078749*F_s + 0.9728903*F_e$$

4) Nighttime case without profile data

$$F_A = 64.52647 - 13.80995*sinsol - 4.028092*cosmel + 0.9453123*F_l^{dn} - 1.108553*F_l^{up} + 1.118411*F_s$$

where cosmel = COS($2\pi \cdot J_m/366$), sinmel = SIN($2\pi \cdot J_m/366$), cosfre = COS($2\pi \cdot J_f/366$), and sinfre = SIN($2\pi \cdot J_f/366$). J_m and J_f are the Julian day numbers from the melting and freezing start dates, respectively. For example, if the melting date is May 1, then $J_m = 10$ means the actual date is May 11.

3.7.8 Thermodynamic Process Adjustment

The One-dimensional Thermodynamic Ice Model (OTIM) used in APP-x/VPP-x processing for ice thickness estimation has been further improved by including a parameterization scheme for the ice thermodynamic process of seasonal freeze-up and melt. To explicitly express this in OTIM, a parameterization scheme was developed and implemented. This is in addition to the residual heat flux adjustment, from which the ice thermodynamic influence was removed. In the new parameterization, ice thickness is adjusted by a factor, called the thermodynamic factor f_{td}, which is a function of the freeze-up and melt dates at a particular location. This significantly improves the ice thickness retrieval, especially for the melt season, though it also affects the freeze-up season. Ice growth/melt will follow the modeled exponential curve, and f_{td} can be estimated by an exponential function of location (latitude/longitude), melting/freezing start dates (month/day), current date (month/day), and modeled maximum/minimum melting/freezing rates at the location. The steps and equations to calculate the f_{td} are:

1) Get the changing rate at a location x by using two known rates and locations.

$$R_x = (R_0*L_1 - R_1*L_0)/(L_1 - L_0) + ((R_1 - R_0)/(L_0 - L_1))*L_x ,$$

where L_1 and L_0 are the two latitudes with changing rates R_0 and R_1. By default, latitudes L_0=50°N/S, L1=90°N/S, and the R_0=1.0 and R_1=2.0.

2) Get the f_{td} at a location by using an exponential function

The normalized Julian day fraction number is $D_x = (D_j - D_{m/f})/D_{period}$, where D_x is from 0∼1 (normalized by period) based on the actual Julian day number D_j, $D_{m/f}$ is the Julian day number when melting/freezing starts, and the D_{period} is the total number of days for the melting/freezing period. By default, the melting/freezing date at a location L_x can be estimated by two known dates at two known locations as in step 1. Once we know D_x, then the thermodynamic factor f_{td} can be estimated in terms of melting/freeing period as below.

For the D_x in a freezing period,

$Y = X**(S*D_x)$, where X is exponential base X=10, and S is the shape control number

S=1, therefore $f_{td} = (Y-1.0)*(R_x - R_0)/(X**S - 1) + R_0$.

For the D_x in a melting period,

$Y = X**(-1.0*S*D_x)$, where X is exponential base X=10, and S is the shape control

number S=1, therefore $f_{td} = (Y- X^{**}(-1.0*S))*(R_x - R_0)/(1.0 - X^{**}(-1.0*S)) + R_0$.

3.7.9 Physical Dynamic Process Adjustment

To better estimate ice thickness, it is necessary to consider ice dynamic processes such as ridging, rafting, and hammocking, in addition to the energy balance at the ice/atmosphere interface. This is becoming extremely important when ice is moving towards coastal areas and has accumulated to form thick ice. To explicitly express ice dynamic processes in OTIM, a parameterization scheme was developed where the estimated ice thickness is adjusted by a factor, called physical-dynamic factor f_{pd}. This physical-dynamic factor f_{pd} is a function of location, wind, and season. This improvement is now applied to the ice thickness retrieval in the coastal areas along Canadian Archipelago.

Wind can play role in the ice thickness by physical dynamic process such as rafting and ridging. First, the wind adjustment factor f_{wind} is estimated by $f_{wind} = (30 - W)/30$, where W is wind speed. Second, the date adjustment factor f_{day} is calculated by $f_{day} = (f_0*d_1 - f_1*d_0)/(d_1 - d_0) + ((f_1 - f_0)/(d_0 - d_1))*d_x$, where d_o and d_1 are the two days with known adjustment factors f_0 and f_1, and d_x is the Julian day number. Third, the location adjustment factor f_{loc} is estimated by $f_{loc} = (f_0*L_1 - f_1*L_0)/(L_1 - L_0) + ((f_1 - f_0)/(L_0 - L_1))*L_x$, where L_o and L_1 are the two locations with known adjustment factors f_0 and f_1, and L_x is the location. Finally, the overall physical dynamic factor f_{pd} can be obtained by $f_{pd} = f_{wind}*f_{day}*f_{loc}$.

3.8 Theoretical Description: Cloud Detection

3.8.1 Physical and Mathematical Description

Methods of detecting clouds in satellite data range from simple thresholding procedures to complex neural networks. No attempt is made here to survey the tremendous breadth of this field; instead, a few examples from the literature are given. Ebert (1987) described one of the first polar-specific cloud retrieval algorithms, one that utilized a variety of spectral and textural measures. Key and Barry (1989) implemented a high-latitude method similar to that used in the global algorithm of the International Satellite Cloud Climatology Project (ISCCP) (Rossow and Garder, 1993) based on spectral, spatial, and temporal variations of clouds. A number of studies have exploited the high reflectivity of liquid water clouds at 3.7 μm during the day (e.g., Allen et al, 1990; Welch et al., 1992; Sakellariou et al., 1993), while only a few have been developed specifically for nighttime retrievals (e.g., Yamanouchi et al., 1987). Most of the cloud detection algorithms are based on empirical relationships derived from a small sample of satellite data.

The cloud masking procedure presented here consists of thresholding operations that are based on modeled sensor radiances. The AVHRR radiances are simulated for a wide variety of surface and atmospheric conditions, and values that approximately divide clear from cloudy scenes are determined. Examples are given in Figures 7 and 8 where

the channel 3 reflectance and the thermal channel differences, respectively, are shown as a function of cloud optical depth. Clear sky is represented as having a cloud optical depth of zero.

3.8.1.1 Radiative Transfer Model

Cloud detection and the retrieval of cloud optical depth and particle effective radius rely heavily on modeled TOA albedo and brightness temperature. Before detailing those procedures, the radiative transfer model Streamer (Key and Schweiger, 1998) is briefly described. TOA radiances (intensities) are computed for use in the cloud property retrievals while irradiances (fluxes) are computed in order to examine the surface radiation budget. For radiances Streamer uses the discrete ordinate solver DISORT described in Stamnes et al. (1988). For irradiances the two-stream method following Toon et al. (1989) is employed. In both cases there are 24 shortwave and 105 longwave spectral bands. Gas absorption for water vapor, ozone, CO2 and oxygen is parameterized using an exponential sum fitting technique (Tsay et al., 1989).

Cloud optical properties are based on parameterization schemes from three different sources. For water clouds, the data are taken from Hu and Stamnes (1993). Effective radii range from 2.5 to 60 μm for shortwave and longwave portions of the spectrum. For ice clouds in the shortwave the parameterization of Fu and Liou (1993) is used. Longwave ice cloud optical properties are based on Mie calculations using spherical particles. This parameterization is unpublished but follows the methodology of Hu and Stamnes. Both the water and ice cloud parameterizations are based on the empirical relationship between the particle effective radius and extinction, single scatter albedo, and the asymmetry parameter.

3.8.1.2 Single-Image Masking

The underlying philosophy of the single-image cloud detection procedure is that it should work as well as possible without requiring ancillary information. The target user is one who has a few individual images that are not necessarily part of a time series, and no additional information such as model fields of surface temperature or an elevation database. The single-image cloud mask procedure could certainly be improved with such information, but it would be unreasonable to require it.

The single image cloud mask uses four primary spectral tests and an optional secondary test. Many of the cloud test concepts can be found in the Air Force SERCAA procedures (Gustafson et al., 1994); some appear in the NOAA CLAVR algorithm (Stowe et al., 1991); most were developed and/or used elsewhere but refined and extended for use in the polar regions. The application of the spectral tests is conceptually simple: initialize the cloud mask to clear, then apply the spectral cloud tests to label cloudy pixels. The primary spectral cloud tests are described in the following paragraphs. Only two of the four tests are applied under all solar zenith angle (SZA) conditions. One is used only when it is dark; the other is used only when it relatively bright. See Table 6 for SZA cutoffs.

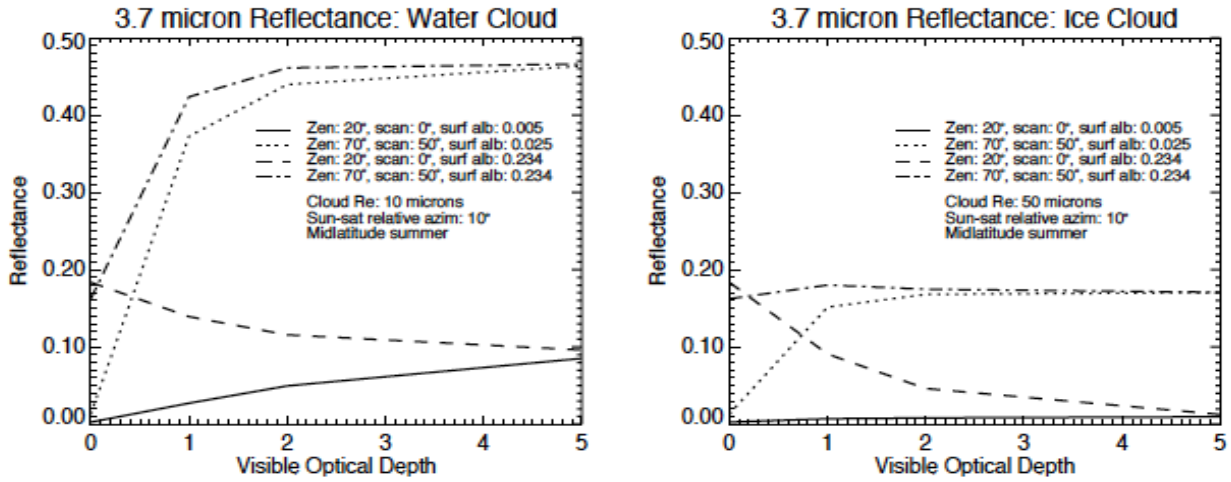

Figure 7. Channel 3 reflectance as a function of liquid (often simply "water") cloud optical depth for a variety of surface and viewing conditions.

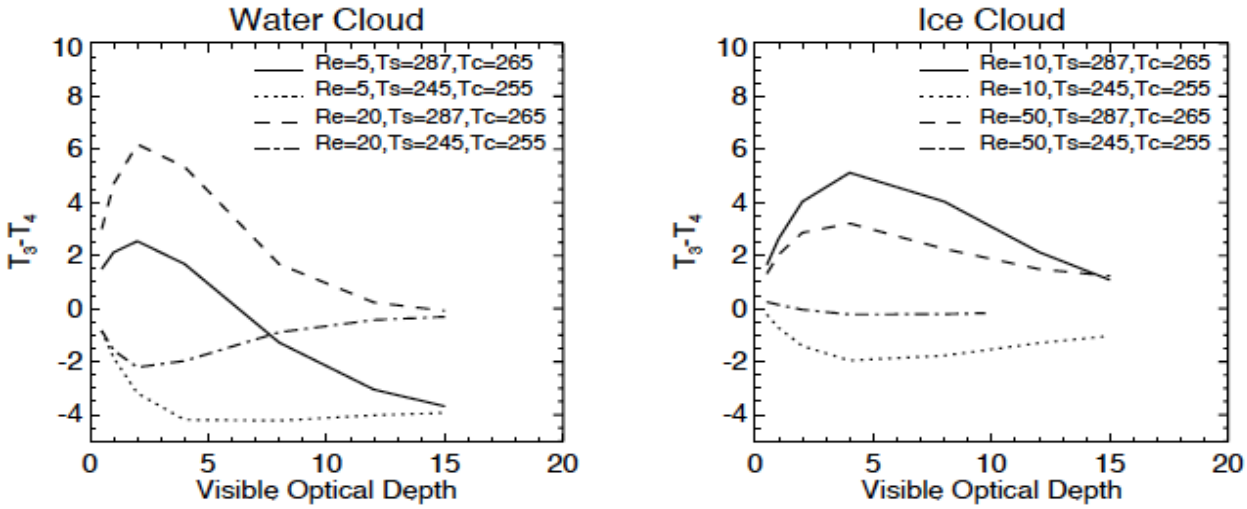

Figure 8. The brightness temperature difference (BTD) of AVHRR channels 3-4 as a function of cloud optical depth for water cloud (left) and ice cloud (right). T_c is the cloud top temperature, *Re* is the cloud particle effective radius.

3.8.1.3 Cloud Tests

Split-Window Cirrus test, 11-12 μm (all SZA) - Ice clouds absorb and scatter less at 11 μm than at 12 μm, so their transmittances are higher at 11 μm. Water clouds also absorb less at 11 μm but they scatter more. Nevertheless, both ice and liquid clouds have higher transmittances at 11 μm. For cold cirrus clouds and thin water clouds the result is higher brightness temperatures at 11 μm. However, water vapor affects this difference and must be considered. This is accomplished indirectly through the use of the scan angle and brightness temperature. The BTD45 differences are corrected for viewing angle

effects before being used in any of the cloud tests. Individual pixels are labeled as cloudy if the corrected btd45 is greater than the CT_THRESH thresholds (Tables 6, 7).

CT_THRESH values are from Saunders and Kriebel (1988) for temperatures of 260 K and greater, with minor adjustments at the low end of the temperature range. For lower temperatures the table was extended by simulating clear sky values with *Streamer* and adding a small offset to account for unmodeled effects. The nadir thresholds are shown in Figure 9. A function that adjusts for the scan angle dependence of BTD45 was then determined empirically, with the same functional form as that given by Yamanouchi et al. (1987):

$$BTD45' = BTD45 - \frac{(23.6 - ZC)(1 - \cos\theta)}{1 - 0.1589(1 - \cos\theta)}$$

where ZC is given in Table 7, BTD45 is the unadjusted brightness temperature difference, and θ is the scan angle. This effectively adjusts the raw brightness temperature difference to a nadir view. The angle adjustment functions are shown in Figure 10. Note that the sign of the correction changes at approximately 260 K. If BTD45' is greater than CT_THRESH then the pixel is cloudy. The model simulations assumed that the surface emissivities were the same at 11 and 12 μm. This is probably not the case for snow, so the thresholds are increased by 0.3 K if the surface is known to be snow. This correction should actually be done to radiances, as the emissivity effect is nonlinear in brightness temperature.

Warm clouds, 11-12 μm (all SZA) - The transmittance relationships described in the previous test hold true regardless of the relationship between the cloud and surface temperatures. For warm clouds BTD45 may be negative, so an additional test is required (cf., Yamanouchi et al., 1987). A pixel is considered to be cloudy if BTD45' < WT_THRESH (Table 7). Temperature inversions and warm clouds are ubiquitous during the polar night, but also occur at other times of the year and in other locations outside of the polar regions; e.g., over cold ocean currents. The CT_THRESH and WT_THRESH are the threshold values to be used with the BTD45' to determine if a pixel is cloud covered or not for cirrus and warm clouds, respectively.

Water cloud test, 1.6 and 3.7 μm (SZA < NOREFZEN) - The single-scattering albedo of small droplets at 1.6 and 3.7 μm (AVHRR channels 3A and 3B) is considerably larger than that of ice crystals, including snow on the surface. Therefore, the 1.6 and 3.7 μm reflectances are very high relative to snow, open water, and vegetation. For sunlit scenes the application of reflectance tests depends on the solar zenith angle. For solar zenith angles less than DAYZEN (Table 6) constant thresholds in channels 1 and 3 are applied. A pixel is considered cloudy if REF3 > REF3_OCEAN and REF1 > REF1_OCEAN or REF3

> REF3_LAND and REF1 > REF1_LAND, where REF1 and REF3 are the channels 1 and 3 reflectances. There are actually REF3_OCEAN and REF3_LAND variables for the 3.7 and

1.6 μm channels, channels 3B and 3A, respectively: REF3A_OCEAN, REF3B_OCEAN, REF3A_LAND, and REF3B_LAND. The channel referenced by "3B" is channel 3 through NOAA-15 and channel 3B on NOAA-16 and beyond. The visible reflectance test reduces the mislabeling of clear snow-free land and silty water (near mouths of rivers) pixels that have relatively high reflectances at 3.7 microns.

If the zenith angle is between DAYZEN and NOREFZEN then these thresholds are scaled, increasing as a function of the zenith angle. A function was derived empirically:

$$REF3' = REF3 + \left(a\frac{REF3ADD}{b}\right)$$

where REF3' is the adjusted threshold, REF3 and REF3ADD correspond to ocean or land types (Table 6; REF3_*_ADD), a=(SZA-DAYZEN)^3, and b=(90-DAYZEN)^3. The same adjustment is done for the channel 1 reflectance. A pixel is cloudy if it's reflectance is greater than REF3' or REF1'. No reflectance tests are applied to for zenith angles between NOREFZEN and NIGHTZEN. Note: This effect is still under investigation.

Low stratus-thin cirrus tests, 3.7-11 μm (SZA >= NIGHTZEN) - Both ice and water clouds have lower emissivities at 3.7 μm than at 11 or 12 μm. Additionally, small droplets scatter much more efficiently at 3.7 μm than at 11 or 12 μm. For optically thick water clouds, where transmittance is small, this translates into a lower brightness temperature in channel 3. Stratus clouds often exhibit this effect, as do thin, warm clouds (less frequent). For thin, cold clouds the brightness temperature at 3.7 μm can be greater than that at 11 μm because of transmitted radiation from the warm surface in the shorter wavelength band. This is typical of cirrus clouds. A pixel is cloudy (low stratus) if BTD34 <= LSTTCI_34LO(a,b), where BTD34 is the brightness temperature difference between channels 3 and 4. This is a temperature dependent test (T11): temperatures less than 235 use a threshold of LSTTCI_34LOa, LSTTCI_34LOb is for temperatures greater than 265, and temperatures in between use a threshold between these two values. Also, a pixel is cloudy (cirrus) if BTD34 >= LSTTCI_34HI. Due to the large amount of noise in channel 3 at low temperatures, this test is only performed for temperatures greater than MINTEMP. The LSTTCI_34LOa, LSTTCI_34LOb, and LSTTCI_34HI are the threshold values to be used with the BTD34 to determine if a pixel is cloud covered or not for low stratus, thin cirrus, and cirrus clouds, respectively.

Cold clouds - Surface Temperature Tests, 11 μm or T_s (all SZA regions) - These tests are intended to detect very cold clouds by comparing the 11μm brightness temperature to either a climatological surface temperature or a surface temperature estimate. The cold cloud over oceans test is most useful during the summer months at night. It has little effect in the winter or during the daytime, when reflective tests work well. In some sense it performs in a manner similar to the MODIS CO2 high cloud test. It tends to find the cold, optically thick clouds that the think cirrus, warm cloud, and low stratus tests miss. It is a simple threshold test that utilizes a monthly climatological estimate of the lowest expected

surface temperature over the ocean (frozen or unfrozen). If the 11 μm temperature is less than the climatological minimum surface temperature, the pixel is cloudy.

The other cold clouds - surface temperature test relies on an estimate of the surface temperature input by the user, and is only performed if an estimate of the surface temperature (or 11 μm brightness temperature, both are treated equally) is provided. It is a simple threshold test such that any pixel with an 11 μm brightness temperature less than 20 K below the surface temperature estimate is considered to be cloudy. This is most useful at night during the winter when some optically thick, cold clouds are misidentified as clear sky.

3.8.1.4 Clear Tests

To account for potential problems with the cloud tests, particularly the 11-12 μm BTD, tests that confidently identify clear pixels are used. The clear tests are only applied to those pixels labeled CLOUDY by the cloud tests.

Low NIR reflectance test (DAY and HISZA regions): This test is the complement of the reflectance cloud test, where pixels with 1.6 or 3.7 μm reflectances less than REF3*0.4 are considered clear.

NDSI test (DAY and HISZA regions): The Normalized Difference Snow Index (NDSI; Hall et al.) is used in conjunction with the NIR reflectance for the AVHRR/3 with the 1.6 μm channel (NOAA-16 and higher). If NDSI is large and the NIR reflectance is small, then the pixel is clear. NDSI is calculated as

$$NDSI = \frac{\rho_1 - \rho_3}{\rho_1 + \rho_3} .$$

3.8.1.5 Rethresholding

The secondary threshold test is a rethresholding operation using only the channel 4 brightness temperatures. It is not employed by default in CASPR, but is available as an option. Using pixels labeled as clear by the primary tests, an average channel 4 temperature image is constructed with a kriging procedure for small regions (200 km over land; 300 km over ocean). During the day (SZA <= NOREFZEN) the 95th percentile clear sky temperature is used; during dim and dark conditions (SZA > NOREFZEN) the median is used. During the day, if the channel 4 temperature is more than DEL4DAY degrees and less than the clear temperature then it is cloudy. While this test works well in identifying thin cirrus, it results in some false detections near coastlines, and in areas with large variability in elevation it may actually create more problems than it solves. During dim and dark conditions when temperature inversions and warm clouds are common, the test is two-sided. If the channel 4 temperature is more than DEL4LO degrees and less than the clear temperature or if it is DEL4HI degrees greater than the clear temperature then it is cloudy.

At night this rethresholding can be important for two reasons: (1) there is less spectral information available and (2) AVHRR channel 3 tends to be noisy at low temperatures, common during the polar night. Concerning the available spectral information, under most conditions optically thick clouds simply cannot be distinguished from clear sky with the three thermal channels alone. This is illustrated for a few cases in Figure 11. The result is false clear detections, i.e., cloudy pixels labeled as clear. Concerning noise in channel 3, it generally results in predictable errors - false cloud detections - so that those pixels not labeled as cloudy by the primary cloud tests are usually clear. So the primary spectral cloud tests at night are expected to result in some false detections for noisy pixels and for optically thick clouds.

The thresholds can be adjusted collectively through the *threshadj* keyword to the procedures **caspr** and **cloudmask_1**. This keyword allows the user to adjust the algorithm to be "cloud-conservative" or "clear-conservative". The cloud/clear-conservative decision is necessary because there will always be partly cloudy pixels, mixed phase clouds, mixed clear pixels, etc. that do not fall neatly into one class or the other. However, this is a somewhat crude in that not all thresholds scale linearly. For best results, change the individual thresholds until the desired results are achieved. The *threshadj* keyword is used in the single-image cloud masking mode when clear parameters are computed. A second, clear-conservative mask is generated to increase the likelihood that those pixels labeled as clear actually are clear.

It is assumed here that we have no a priori knowledge of surface characteristics (e.g., surface temperature from the previous day) and no a priori knowledge of the location of snow/ice. In fact, the only distinction between surface types is land and ocean. Land may be snow-free or snow-covered. Ocean can be open water or sea ice. Additionally, the nighttime procedure does not incorporate any surface type distinction. This severely limits single-image cloud masking accuracy. Having such information would allow the use of additional spectral cloud tests (e.g., the channel 2/1 ratio over snow-free land), and would allow "tighter" thresholds.

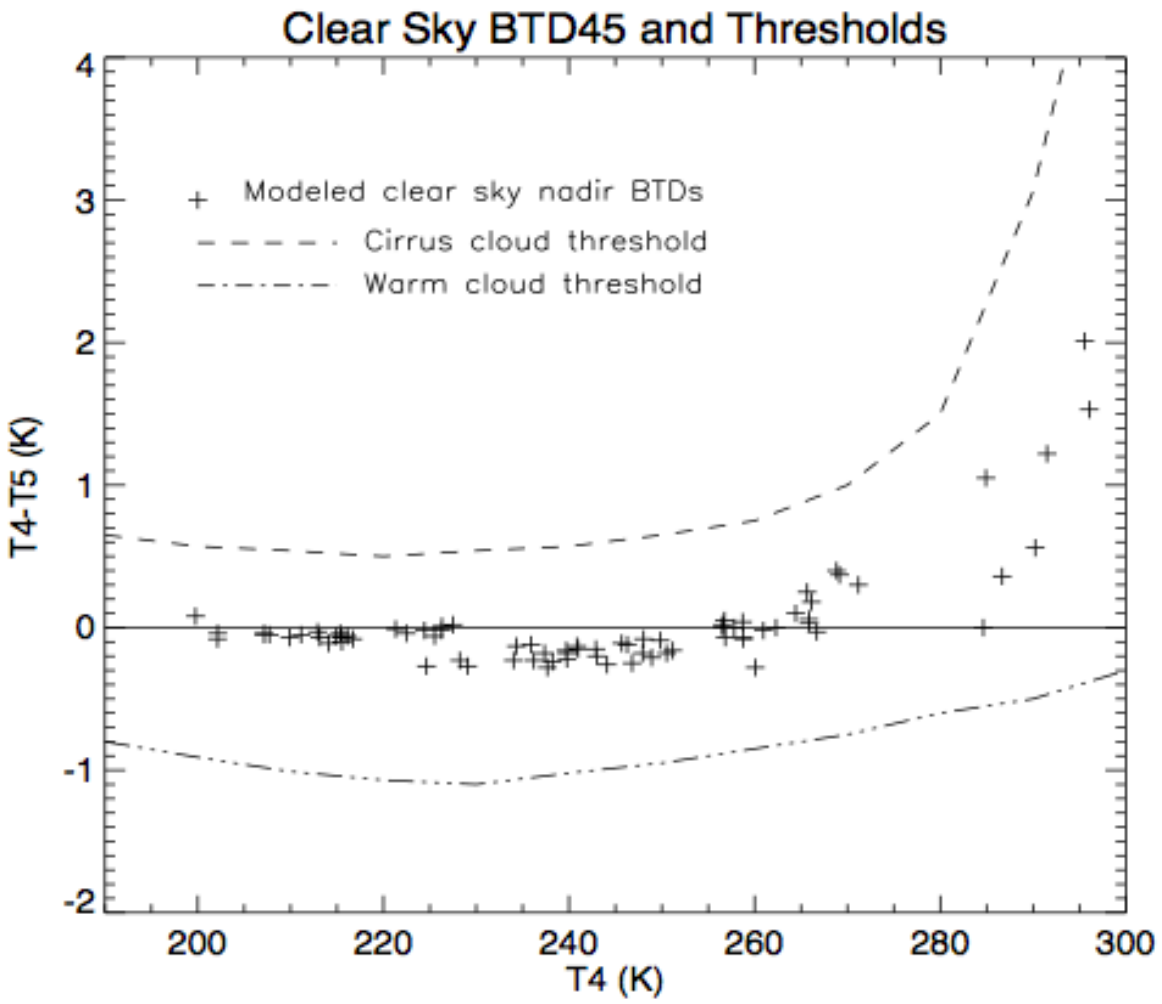

Figure 9. Modeled (*Streamer*) clear sky brightness temperature differences (plus signs) and the cirrus and warm cloud test thresholds (dashed and solid lines, respectively).

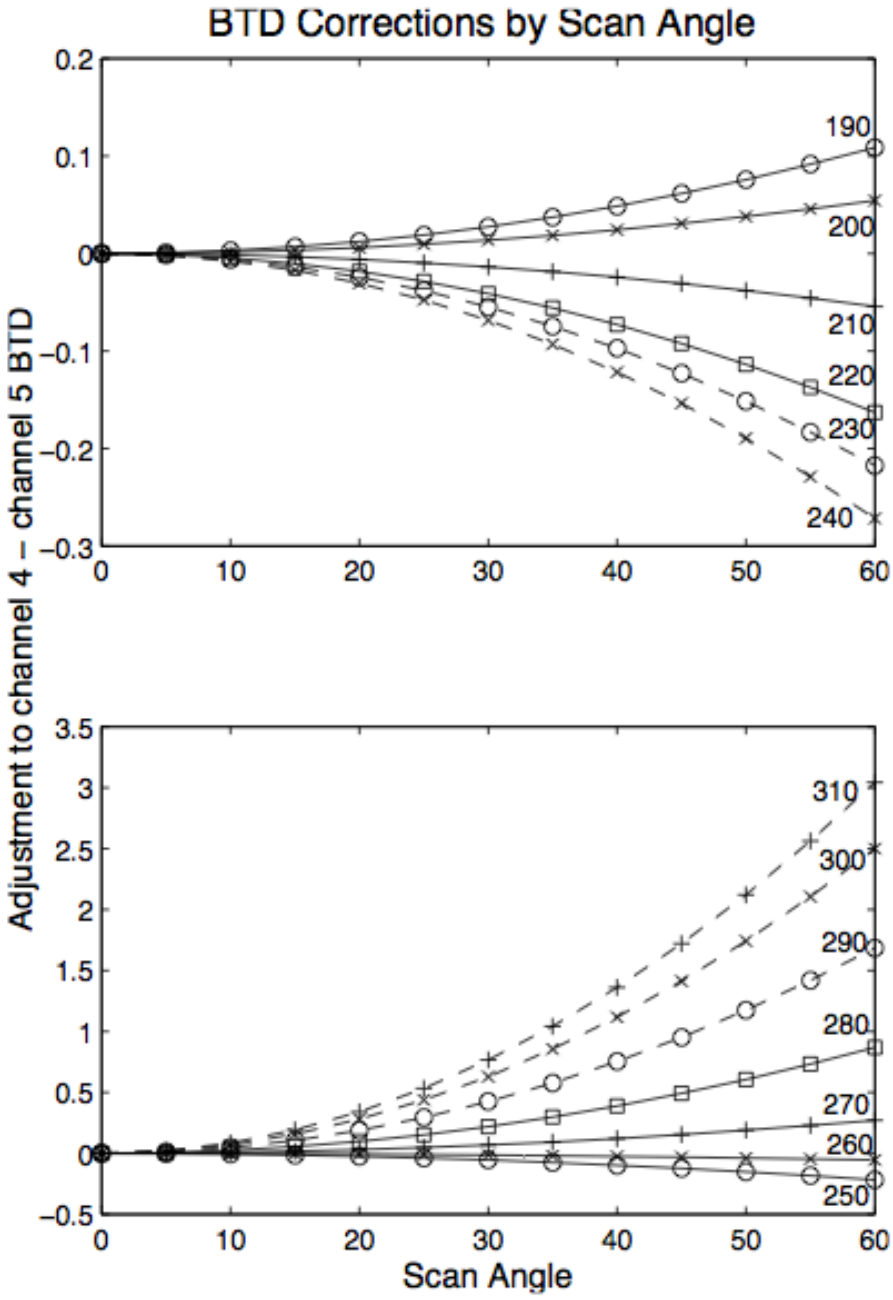

Figure 10. Brightness temperature difference dependence on scan angle. These functions are used to adjust brightness temperature differences before application of the cirrus and warm cloud tests.

Table 6. Thresholds used in cloud detection.

Threshold Variable	Value
DAYZEN	60
NOREFZEN	85
NIGHTZEN	88
DEL4DAY	8.0
DEL4LO	4.0
DEL4HI	4.0
REF3A_OCEAN	0.04
REF3B_OCEAN	0.1
REF1_OCEAN	0.35
REF3A_LAND	0.40
REF3B_LAND	0.09
REF1_LAND	0.35
REF3A_OCEAN_ADD	0.0
REF3B_OCEAN_ADD	0.0
REF3A_LAND_ADD	0.15
REF3B_LAND_ADD	0.15
REF3A_SNOW_ADD	0.5
REF3B_SNOW_ADD	0.5
REF1_OCEAN_ADD	0.10
REF1_LAND_ADD	0.15
LSTTCI_34LOa	0.3
LSTTCI_34LOb	-0.7
LSTTCI_34HI	3.5

Table 7. Brightness temperature difference thresholds for the cirrus cloud test as a function of temperature (K).

	190	200	210	220	230	240	250	260	270	280	290	300	310
CT_THRESH	0.45	0.37	0.34	0.34	0.34	0.40	0.50	0.75	1.00	1.50	3.06	5.77	9.41
WT_THRESH	-0.8	-0.91	-1.01	-1.07	-1.1	-1.02	-0.95	-0.85	-0.75	-0.6	-0.5	-0.3	-0.15
ZC	23.4	23.5	23.7	23.9	24.0	24.1	24.0	23.7	23.2	20.5	19.7	19.0	18.0

3.8.1.6 Time Series Masking

The time series cloud masking procedure operates on a sequence of images acquired on consecutive days at approximately the same solar time. It first applies spectral tests for an initial labeling of cloudy and clear pixels, then further refines the identification of clear pixels by examining changes in spectral characteristics from one day to the next. The clear pixels that result from these spectral and temporal tests are used to construct clear sky radiance statistics over some number of days for various spectral channels. The statistics are then used in a final thresholding operation to label/relabel pixels as either clear or cloudy. More specifically the steps are:

1. Apply the single-image cloud mask procedure to identify pixels that are likely to be cloudy. This alleviates the problem of persistent cloud being labelled as clear in the time tests.

2. Examine the time change in spectral characteristics between pairs of days. A pixel is clear if the spectral tests (step #1) say it not cloudy and if it varies little from one day to the next. The channel 4 brightness temperature and the adjusted brightness temperature difference (4-5) are used in the dark parts of the image; these plus the channel 1 reflectance, and the channel 3 reflectance are used in the sunlit portions. Table 8 gives the thresholds used in this step.

3. Clear sky statistics are compiled for each pixel using all clear values within some distance of the pixel and over some number of days (typically 150x150 km cells and 5 days). Medians of the channels 1 and 3 reflectances (day only) and the channel 4 temperature (day and night) are computed. If a cell occurs along a coastline, only pixels with the same surface type (LAND or NOTLAND) as the center pixel are used. Pixels in the clear sky composite that did not have medians assigned due to the lack of clear values are filled with a kriging interpolation scheme. The probability of finding clear pixels can be increased by enlarging the cell size or using more days but doing so also increases the variability and may adversely affect the next step.

4. The clear sky composite statistics are used in a final threshold operation to label or relabel all pixels as clear or cloudy. A pixel can be labeled as cloudy if its

brightness temperature is higher or lower than its mean clear value plus or minus, respectively, some value that reflects the natural variability for clear sky, or if its reflectance in either channel 1 or 3 (daytime) is higher than its mean clear reflectance plus (not minus) some value (DEL* in Table 8). However, the single-image spectral tests are run again in cloud-conservative mode and those pixels labeled as cloudy will also be cloudy in the final mask. This implies higher confidence in the spectral tests (with cloud-conservative thresholds) than in the final thresholding operation.

Table 8. Time and final thresholds used in cloud detection.

Threshold Variable	Value
TIMETHRESH3A	0.06
TIMETHRESH3B	0.04
TIMETHRESH1	0.07
TIMETHRESH4_LAND	3.0
TIMETHRESH4_OCEAN	2.0
TIMETHRESH45_LAND	0.40
TIMETHRESH45_OCEAN	0.35
DEL4LO_OCEAN	3.0
DEL4HI_OCEAN	3.0
DEL4LO_LAND	4.0
DEL4HI_LAND	4.0
DEL4LO_SNOW	6.0
DEL4HI_SNOW	6.0
DEL1	0.07
DEL3A_OCEAN	0.06
DEL3A_LAND	0.08
DEL3B_OCEAN	0.045
DEL3B_LAND	0.055

Cloud masks for images at the beginning and end of the time series have a much larger uncertainty than those at least ndays/2 places away from the ends. This results from the first and last few images being at the beginning or end of the ndays images on which the

clear sky statistics were based. For example, given ndays = 5, the cloud mask for the first image is determined from the final thresholding based on clear sky statistics over days 1-5. The cloud mask for the third image is based on statistics from the same period. Obviously, the statistics are more representative of the third image of the first.

3.8.2 Numerical Strategy

Not applicable.

3.8.3 Calculations

The AVHRR/VIIRS reflectances, brightness temperatures, and viewing and illumination geometry are input, as is a surface type mask. Cloud tests are executed sequentially. Time series cloud detection is applied as described above.

3.8.4 Look-Up Table Description

There are no look-up tables for cloud detection. The thresholds in the tables above are part of the code.

3.8.5 Parameterization

Parameterizations are described above.

3.9 Theoretical Description: Cloud Particle Phase

3.9.1 Physical and Mathematical Description

This section describes the algorithms used in the determination of cloud particle phase. In this algorithm, all clouds are composed of either liquid droplets ("water cloud") or solid ice crystals ("ice cloud"). No attempt is made to identify mixed-phase or multilayer clouds. The theoretical background for these procedures is detailed in Key and Intrieri (2000). Only a partial description is given here.

The determination of cloud particle phase, liquid or solid (generally referred to as "water" and "ice"), is based on both physical and spectral properties. Physically, liquid cloud droplets can exist at temperatures as low as -40 C, perhaps even lower, although clouds are likely to be of composed of both liquid droplets and ice crystals at temperatures below -10 C. The spectral difference between water and ice clouds occurs because of differences in absorption and scattering. Based only on the imaginary index of refraction, which is an indicator of absorption, more absorption will take place in ice clouds at 11 and 12 μm than in water clouds, so brightness temperature differences between 3.7 and 11 or 12 μm will be larger for ice clouds. However, absorption alone does not provide enough information to

explain observed spectral differences. The single scattering albedo indicates how effective a volume of particles are at scattering incident radiation. Unlike the imaginary index of refraction, it applies to size distribution of particles. Scattering is greater at 3.7 μm than at 11 or 12 μm and the smaller the particle, the greater the scattering. But for typical ice crystals sizes there is very little difference in scattering across this portion of the spectrum. Furthermore, the single scattering albedo indicates that during the day, ice clouds will exhibit a lower reflectance at 3.7 μm than water droplets. At visible wavelengths, the single scattering albedo of both water and ice clouds is near unity and absorption is near zero.

For optically thick clouds, where the transmittance is near zero and the surface contribution to upwelling radiance is small, absorption and scattering define the spectral characteristics of a cloud. We expect the brightness temperature difference between channels 3 and 4 (BTD34) to be negative for water clouds with small effective radii. For thick ice clouds with particle effective radii of 30 μm or larger, the single scattering albedo indicates that BTD34 would be near zero. This is, in fact, the case, as demonstrated by the model calculations (Streamer) presented in Figure 11. Both plots show that for visible optical depths τ greater than 5, water cloud BTD34 is negative while ice cloud differences tend to be positive, at least for smaller water droplets and larger ice crystals. For larger optical depths BTD34 for ice clouds decreases. For optically thin clouds the transmissivity is not negligible and the surface temperature influences the brightness temperature measured at the satellite. BTD34 for cold, water clouds (surface is warmer than the cloud) is positive when the optical depth is small. BTD34 for ice clouds takes on larger positive values in these cases. The opposite occurs for warm ice clouds, where BTD34 is negative.

The brightness temperature difference between 11 and 12 μm, BTD45, is much smaller than BTD34 for both water and ice clouds, and there is considerable overlap in BTD45 for the two phases (Figure 11). The absolute value of BTD45 increases as cloud optical depth decreases (not shown). Therefore, large BTD45 differences (positive or negative) indicate thin clouds.

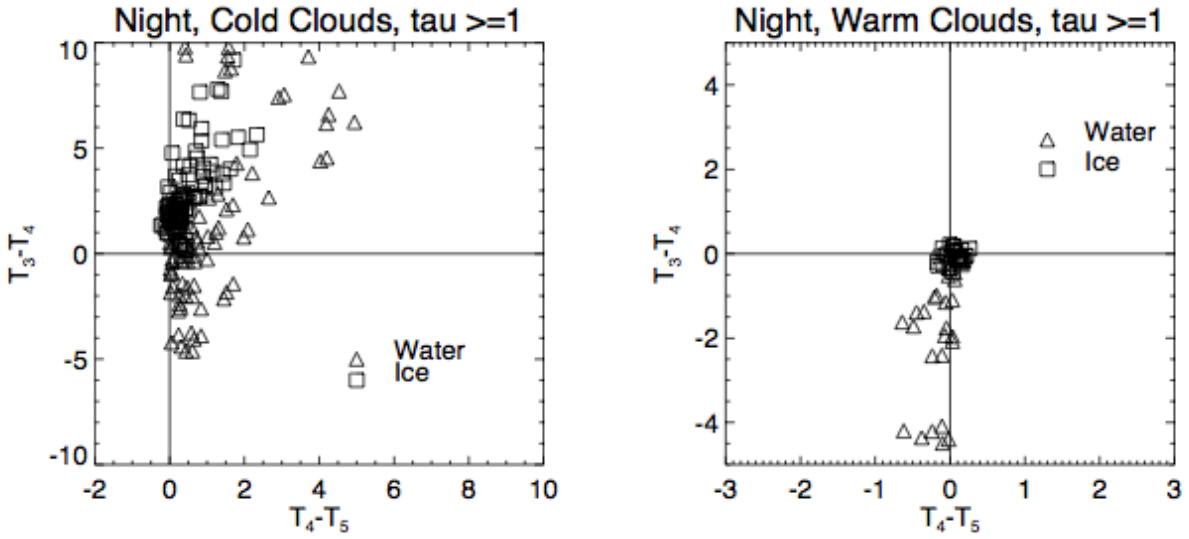

Figure 11. Modeled brightness temperature differences for AVHRR channels 3 minus 4 (3.7 minus 11 μm) and channels 4 minus 5 (11 minus 12 μm) for water and ice clouds. The visible optical depth for the data shown is one or greater. Water clouds have top temperatures greater than 250 K; ice clouds are less than 270 K. Calculations were done for tropical, midlatitude, and arctic conditions.

In the presence of solar radiation, the single scattering albedo at 3.7 or 1.6 μm is the primary spectral feature used in distinguishing ice and water cloud. Ice particles do not scatter as efficiently as water droplets at this wavelength, due to both their indices of refraction (the real part) and the fact that ice clouds are typically composed of larger particles, which scatter less efficiently, than water clouds. However, the actual reflectance depends not only on particle phase, but also on viewing and illumination geometry and surface reflectance. This is illustrated in Figure 12, which shows the 3.7 μm (NOAA-15 and earlier) and 1.6 μm (NOAA-16 and later) modeled reflectances as a function of the scattering angle. The scattering angle ψ is the angle between the incident and reflected beams:

$$\psi = 180 - \text{acos}(\cos\theta_{sun}\cos\theta_{sat} + \sin\theta_{sun}\sin\theta_{sat}\cos\phi)$$

where θ_{sun} is the solar zenith angle, θ_{sat} is the satellite zenith angle, and φ is the relative azimuth angle (where 0 is looking away from the sun and 180 is looking into the sun); all angles are in degrees. A scattering angle of 0^o implies forward scattering; 180^o means backscattering. The figure gives reflectances for cloud visible optical depths between 2 and 5, and for snow and vegetation surfaces. These two surface types exhibit somewhat different 3.7 μm clear sky reflectances and very different clear sky reflectances at

1.6 μm. However, their effect on the reflectance of thick clouds is minimal. The smooth curves represent approximate upper limits for ice cloud reflectance at each wavelength, valid for ψ values between 0^o and 160^o and for optically thick clouds. In the case of strong backscattering ($\psi > 160^o$), and in the case of thin clouds, the separation between water and ice cloud is less clear.

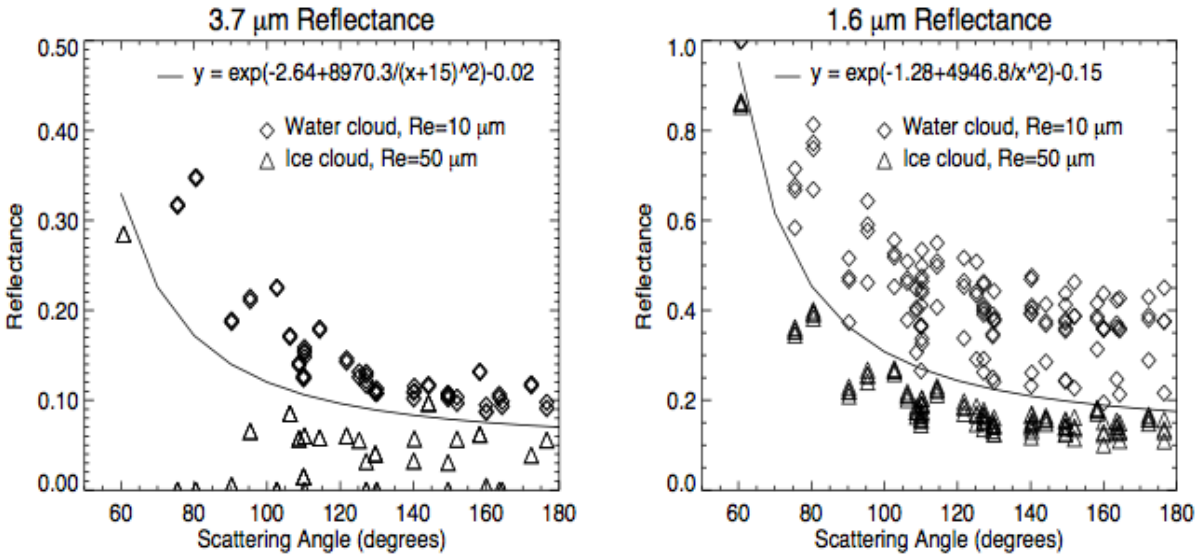

Figure 12. AVHRR channels 3 (3.7 μm) and 3A (1.6 μm) modeled reflectances as a function of scattering angle for water (diamond) and ice (triangle) clouds. All clouds have visible optical depths in the range 5-10. Also shown are the functions that approximately divide water and ice clouds at each of the two wavelengths. Calculations were done using midlatitude summer conditions.

The phase algorithm starts by exploiting the physical property that only ice crystals will exist below some threshold temperature and only liquid droplets will exist above some other threshold temperature. For optically thick clouds the 11 μm brightness temperature will be very close to the kinetic temperature and simple temperature thresholds can be used to distinguish particle phase. For example, if T_4 were less than some minimum value, γ_{min} = 243 K (-30°C), then an optically thick cloud would almost certainly be composed of ice crystals. Similarly, if T_4 were greater than some maximum value, γ_{max} = 273 K (0°C) then the cloud would be liquid. But for optically thin clouds surface emission is a significant part of the measured radiance, and the relationship between the surface temperature and T_4 must be considered. Using the two thresholds above there are four relationships between the surface temperature T_s and T_4 that can be exploited to determine the phase, as listed in Table 9.

‘

Table 9. Phase assignment based on temperature relationships.

Condition	Phase
T_s-δ < γ_{max} and $T_4 > \gamma_{max}$	Liquid
T_s-δ > γ_{max} and $T_4 > T_s$	Liquid
T_s-δ > γ_{min} and $T_4 < \gamma_{min}$	Ice
T_s-δ < γ_{min} and $T_4 < T_s$	Ice

The clear sky temperature can be used as a proxy for T_s, although T_s will generally be somewhat lower than the clear sky value during the day (negative cloud radiative effect) and somewhat higher at night. The clear sky surface temperature can therefore be adjusted by a small amount δ. At night δ = −2 K and during the day δ = +2K in this study. The application of these four conditions constitutes the first step of phase determination. The tests in Table 9 do not handle water clouds with temperatures less than γ_{max} or less than T_s, and ice clouds with temperatures greater than γ_{min} or greater than T_s.

If no estimate of T_s is available then an alternate, though less robust, method would be to simply simple thresholds; e.g., if T4 is less than 243 K (-30°C) then the cloud is ice and if T4 is greater than 303 K (+30°C) then the cloud is liquid. Hutchison et al. (1997) use -40°C for the lower threshold but suggest that -30°C is probably a reasonable lower bound. They do not suggest an upper bound for liquid clouds.

The second step employs the spectral properties described in the previous section and is different for day and night conditions. It is applied to the cloudy pixels that were not labeled in the first step. At night the tests are intended to identify optically thick ice cloud, thick water cloud, and most thin water cloud. The tests are: (a) if T3-T4 is less than -0.5 K then it is a water cloud and (b) if T3-T4 is greater than +1 K and T4-T5 is between 0 and 1 K then it is an ice cloud.

During the day the tests in the second step are based on the 3.7 or 1.6 μm reflectance characteristics, utilizing the two reflectance functions shown in Figure 12. Only pixels with ψ less than 160 degrees and T4–T5 less than 1 K are evaluated, as reflectances for strong backscattering and thin clouds are ambiguous. Observed 3.7 or 1.6 μm reflectances less than the threshold function values indicate ice cloud; those greater than the function values are water cloud.

The last step is to label any pixels that where not handled by the previous two steps. A simple temperature threshold is employed: if the 11 μm brightness temperature is less than 258.16 K (-15° C) then the cloud phase is ice, otherwise it is liquid. Because of the low precision and high uncertainty in T3 (and therefore T3-T4) when temperatures are very low, all pixels with T4 less than 230 K are labeled as ice.

3.9.2 Numerical Strategy

Not applicable.

3.9.3 Calculations

The AVHRR/VIIRS reflectances, brightness temperatures, and viewing and illumination geometry are input. Cloud particle phase is retrieved based on the tests described above.

3.9.4 Look-Up Table Description

There are no look-up tables for the cloud particle phase algorithm.

3.9.5 Parameterization

There are no parameterizations for the cloud particle phase algorithm.

3.10 Theoretical Description: Cloud Optical Depth and Particle Effective Radius

3.10.1 Physical and Mathematical Description

The retrieval of cloud optical and microphysical properties from the AVHRR or AVHRR-like wavelengths has a long history; only a sample of the literature is given here. Hunt (1973) demonstrated the sensitivity of cloud emittance to changes in optical depth and particle size at thermal wavelengths. Liou (1974) showed that cirrus optical properties varied between 11 and 12 μm. Arking and Childs (1985) describe a technique for extracting a microphysical model parameter from AVHRR data. Inoue (1985) used the split-window channels to estimate cloud optical depth with an implicit particle size, while d'Entremont (1986) detected low clouds and fog at night using the variation of the 3.7-11 μm difference with particle size. Using a radiative transfer model and ground-based lidar for validation, Stone et al. (1990) discuss the problem of retrieving cirrus cloud optical depth from radiance measurements. Lin and Coakley (1993) used AVHRR channels 4 and 5 to simultaneously solve for the emittance and cloud fraction. Ou et al. (1993) developed a method to derive optical depth, cloud top temperature, and effective radius from nighttime observations in AVHRR channels 3 and 4. Baum et al. (1994) modeled brightness temperature differences for liquid and ice clouds over the ocean. A review of cloud observations using satellites was given by Rossow (1989).

The importance of cloud optical depth τ and the particle effective radius re for remote sensing lies in the fact that the optical properties of clouds used in the calculation of radiative fluxes, the single scattering albedo, the asymmetry parameter, and the extinction

coefficient, are proportional to the optical depth and effective radius. Cloud optical depth (unitless) is a measure of the cumulative depletion of radiation as it passes through the cloud. It is related to the transmissivity *t* via,

$$t = e^{-\tau}$$

and is a product of the volume extinction coefficient and the physical thickness of the cloud.

The particle effective radius for liquid droplets is the ratio of the third to second moments of the drop size distribution *n(r)*:

$$r_e = \frac{\int_0^\infty r^3 n(r)dr}{\int_0^\infty r^2 n(r)dr}.$$

For ice crystals the size parameter is better termed the "mean effective size". It is based on the parameterization of Fu and Liou (1993), which was developed from ray tracing calculations for scattering by randomly-oriented hexagonal crystals. The mean effective size is defined as:

$$D_e = \left(\int_{L_{min}}^{L_{max}} D^2 L n(L)dL\right) / \left(\int_{L_{min}}^{L_{max}} DL n(L)dL\right)$$

where *D* is the width of an ice crystal, L is the length, n(L) is the size distribution, and L_{min} and L_{max} are the minimum and maximum lengths of ice crystals, respectively. In CASPR, "effective radius" refers to these two size parameters.

Cloud optical depth retrievals are done using a comprehensive database of modeled reflectances and brightness temperatures covering a wide range of surface and atmospheric conditions (Key, 1995). Figures 13 and 14 give a few examples of the modeled data used in the retrieval of cloud optical depth and particle effective radius.

The basic approach for daytime retrievals of water (liquid) cloud follows that of Nakajima and King (1990) as illustrated in Figure 13. In the presence of solar radiation, the retrieval is done using the reflectance in channels 2 and 3 (or 3A for NOAA-16 and later). For ice clouds under solar illumination the channel 3 reflectance is so small that it is unreliable. Therefore, channels 4 and 5 are used to obtain a range of possible solutions and channel 2 is used to constrain the solution. A valid solution exists if the observed brightness temperatures and BTDs fall within the range of the modeled data. If no valid solution was found, MISSING values are assigned.

At solar zenith angles greater than about 75-80 degrees over bright surfaces, uncertainties in modeled radiances and in the calibration of AVHRR channels 1 and 2 are large. When the solar zenith angle is greater than 80 degrees but less than 90 degrees, and when the surface clear sky channel 2 reflectance is high, only channels 4 and 5 are used in the retrieval. Solutions are obtained for all cloud top temperatures in the modeled data, and the effective radius/optical depth pair for the lowest cloud (arbitrary) that had a valid solution is given as the result. If no valid solution was found, MISSING values are assigned. Figure 5 shows the latitudes and times of the year where solar zenith angles greater than 75 degrees are experienced.

For nighttime retrievals, brightness temperature differences for channels 3 (or 3B) and 4 and 4 and 5 are employed (Figure 14). Both methods are based on the fact that the optical properties of clouds are different at each of the wavelengths examined. All three thermal channels are used for both liquid or ice clouds. The lookup table of brightness temperature differences is constructed for three different cloud top heights: 850, 650, 500 mb for liquid clouds and 700, 500, and 300 mb for ice clouds. The retrieval is done for each cloud top in both thermal channel combinations (3, 4 and 4, 5). The solution is the channel 4, 5 retrieval where the difference between the retrievals from both channel pairs is smallest.

In the lookup table procedure, interpolation to the observed values of solar zenith angle (0-85 degrees), precipitable water (2987-29,879 g m^{-2}), and surface visible albedo (daytime; 0.06-0.99) or temperature (nighttime; 228-283 K). Single values of aerosol optical depth (0.06) and total column ozone (325 Dobson units) are used in all cases. Bilinear interpolation is done between effective radius and optical depth value pairs in the lookup tables; i.e., between the four points of each polygon in Figures 13 and 14. Effective radii for liquid clouds are 2.5, 6, 10, 14, 20 μm and for ice clouds are 20, 40, 60, 90, 120 μm.

Optical depth values are 0, 1, 2, 4, 10, 20, 50, 80, and 150, with a maximum nighttime value of 15 and an ice cloud maximum of 50. The optical depth maximum for ice clouds is a result of their relatively low water contents. All clouds are modeled as either water or ice, with no mixed-phase clouds or overlapping combinations. Of course, it is entirely possible to have a liquid cloud under an ice cloud with a total optical depth greater than 50.

For the daytime retrievals the reflectance of the surface under the cloud is assumed to be known. Similarly, the surface temperature under the cloud is needed for the nighttime retrievals. Neither can be measured directly from the AVHRR/VIIRS so they must be estimated. The relationship between the clear and cloudy sky reflectances depends on the cloud optical depth, phase, and the particle size distribution, and the anisotropic and spectral reflectance characteristics of the surface. The cloudy sky surface temperature is related to the clear sky temperature through the cloud base temperature, the residence time of the cloud, and the turbulent fluxes. Given the complexity of these relationships, no attempt is made to relate clear and cloudy temperatures or reflectances. A kriging procedure is used to create relatively smooth surfaces from the existing clear sky reflectances and temperatures for each surface type in the image. These clear sky surfaces are used as proxies to the actual surface reflectance and temperature in the optical depth/effective radius retrievals. The effect of using the clear sky values in place of the

cloudy sky values is probably minimal for the daytime retrievals. At night, however, the effect can be significant, generally resulting in a positive bias in optical depth (i.e., the optical depths are too large) because clear sky surface temperatures may be considerably lower than cloudy sky temperatures.

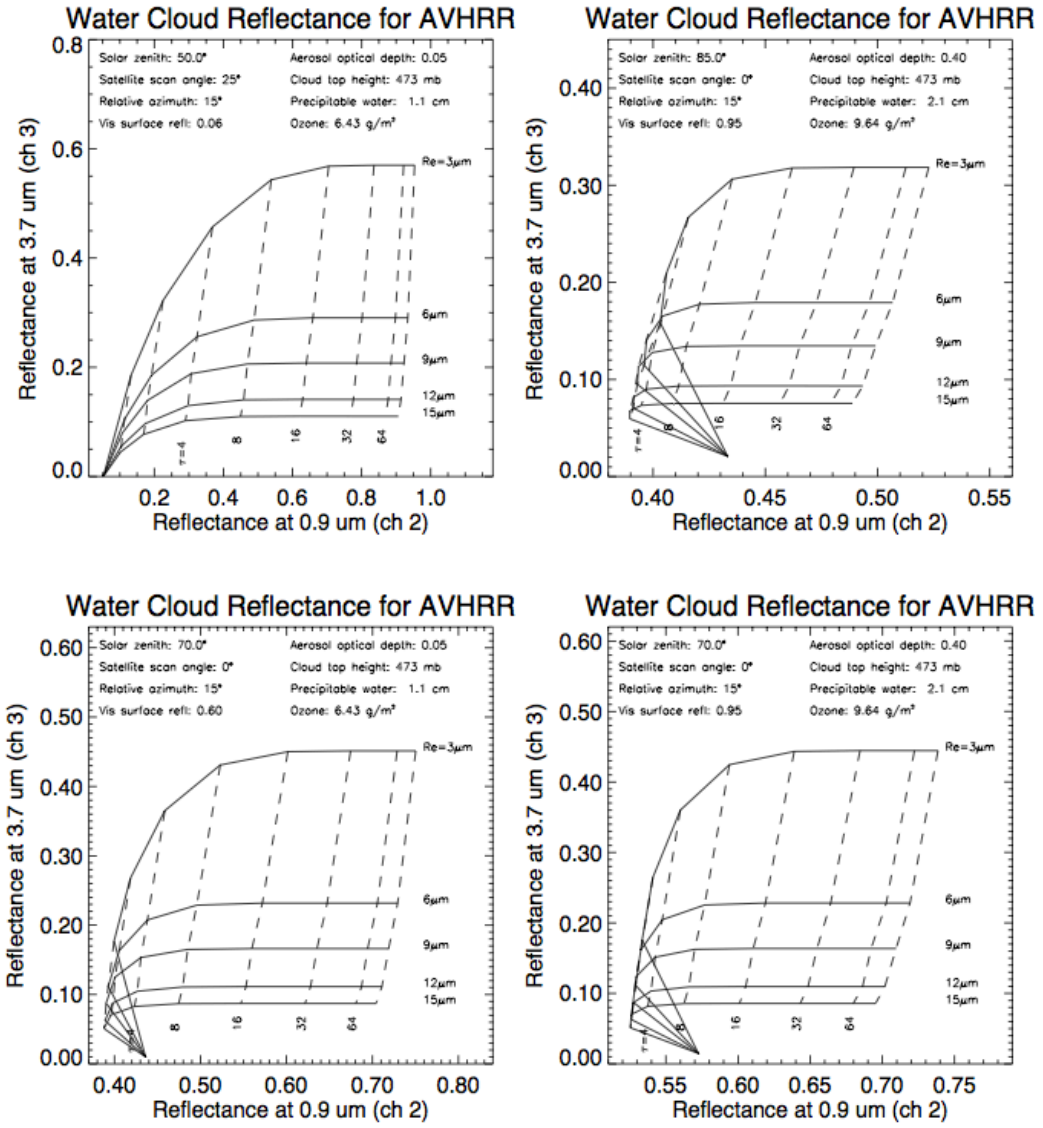

Figure 13. The relationship between two AVHRR reflective channels (2 and 3) as a function of water cloud optical depth and droplet effective radius over different surface types.

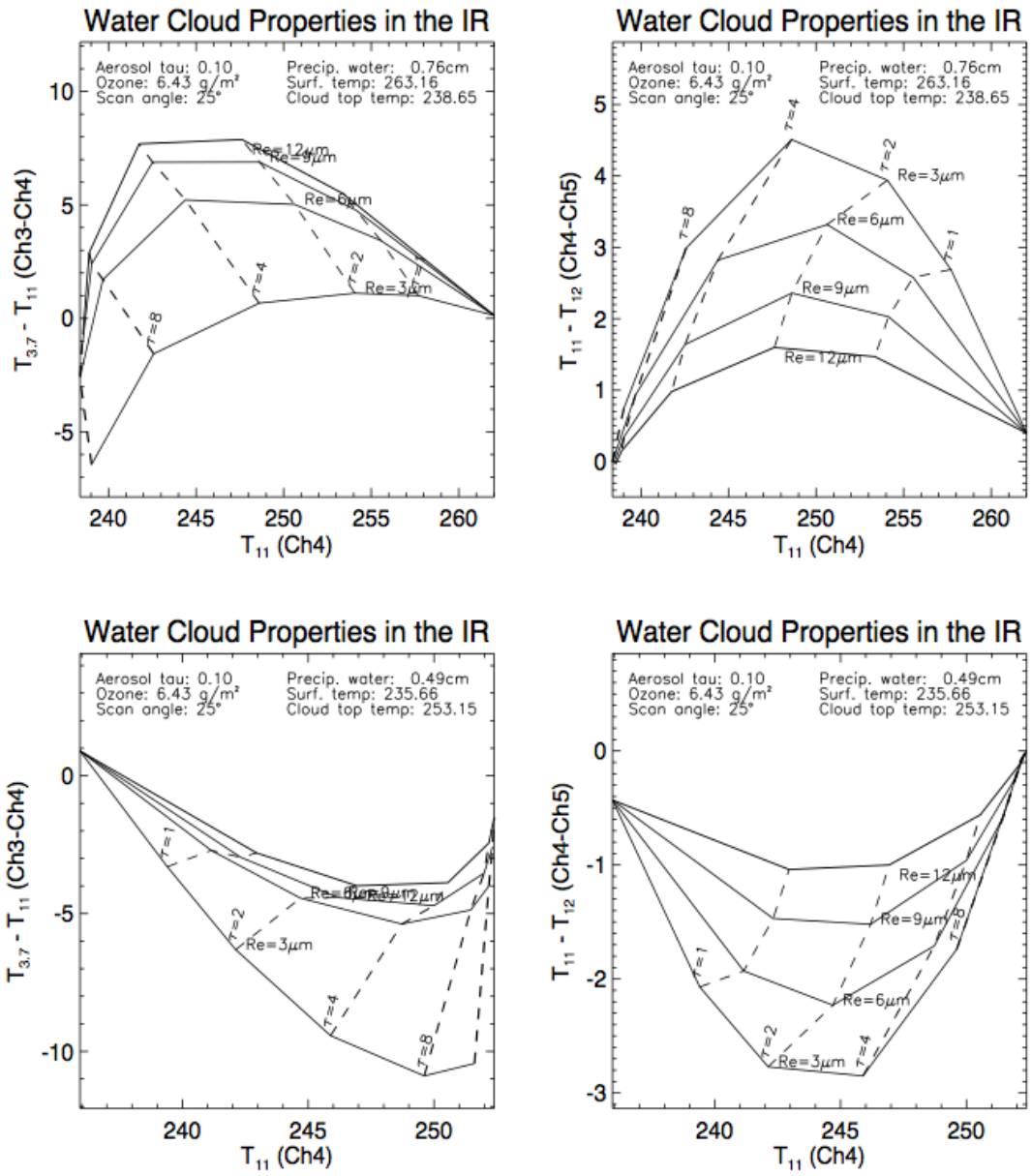

Figure 14. The relationship between the AVHRR channel 4 brightness temperature and the channels 4-5 difference as a function of water cloud optical depth and effective radius.

3.10.2 Numerical Strategy

Not applicable.

3.10.3 Calculations

The AVHRR/VIIRS reflectances, brightness temperatures, and viewing and illumination geometry are input. Previously calculated surface albedo, surface temperature, and cloud

particle phase are used. Cloud optical depth and effective radius are retrieved simultaneously.

3.10.4 Look-Up Table Description

A look-up table of simulated AVHRR reflectances and brightness temperatures was generated with the Streamer radiative transfer model. Channel data are stored as a function of sensor scan angle, solar zenith angle, sun-satellite relative azimuth angle (5 degree bins), surface albedo, and surface temperature.

3.10.5 Parameterization

There are no parameterizations for the cloud optical depth and effective radius algorithm.

3.11 Theoretical Description: Cloud Temperature and Pressure

3.11.1 Physical and Mathematical Description

The cloud temperature is determined from the channel 4 brightness temperature, the clear sky brightness temperature (not corrected for the atmosphere), and the visible cloud optical depth. The infrared optical depth is determined from the visible optical depth using parameterizations of cloud optical properties. The thermal cloud optical depth, which in the retrieval is a nadir (vertical) optical depth, is converted to an optical depth along the slant (viewing) path by dividing it by the cosine of the sensor scan angle. If this adjusted cloud optical depth is less than some threshold, the brightness temperature is assumed to be a function of both the cloud temperature and the upwelling radiation from the surface and atmosphere below the cloud. The threshold is taken from the ISCCP processing scheme, chosen such that clouds with optical depths greater than the threshold have transmittances of less than 1% (equivalent to an optical depth of 4.6) and are considered opaque. For opaque clouds the cloud top temperature is simply the channel 4 temperature. If the cloud is not opaque, then the cloud temperature is determined by first computing the cloud transmittance t from the infrared optical depth, then calculating the cloud radiance that would be required to produce the observed radiance of the cloudy pixel, given the cloud optical thickness and the observed clear sky radiance (as an approximation of the surface radiance under the cloud):

$$L_c = \frac{L_4 - tL_{clear}}{1 - t}$$

where L_c is the cloud radiance, L_4 is the channel 4 radiance, and L_{clear} is the clear sky radiance. If the estimated surface temperature is too low and the cloud is thin, then the

cloud top temperature will be too high and vice versa. If the adjusted cloud top temperature is either lower than the tropopause temperature or higher than the maximum temperature from 950 mb to the tropopause, then it is reset to either the minimum or maximum temperature, as appropriate.

This scheme does not necessarily determine the cloud top temperature, but rather the effective radiating cloud temperature. While this may be close to the top temperature, it will generally represent a temperature somewhere beneath the cloud top. The differences between the retrieved cloud temperature and the actual cloud top temperature are illustrated in Figure 15 for two cases. For thin clouds the difference is greatest. Fortunately, the effect of this "error" on longwave radiative fluxes is small, because the thinner the cloud, the less is its influence.

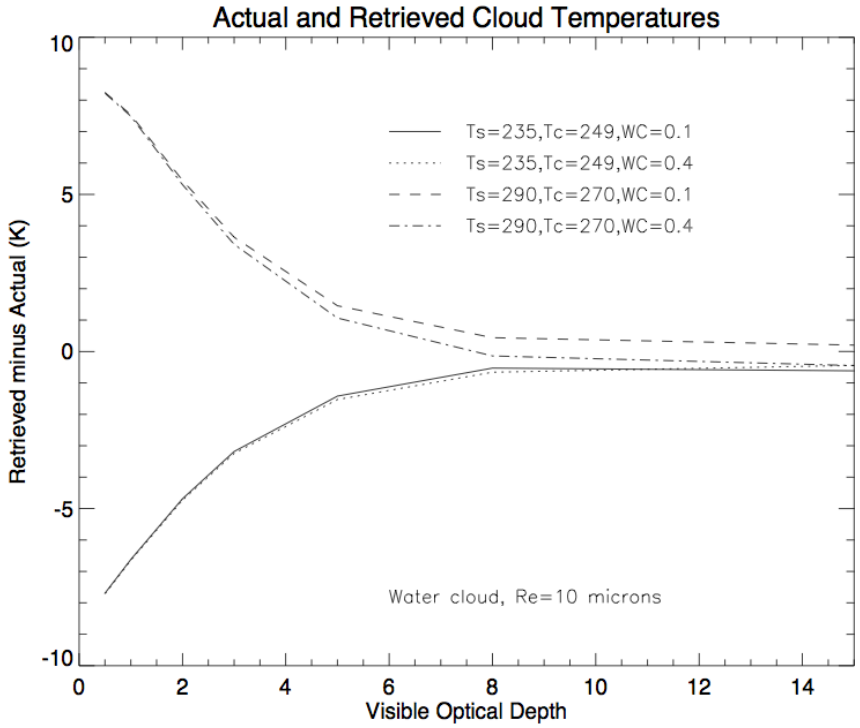

Figure 15. The difference between the retrieved cloud temperature and the actual cloud top temperature as a function of cloud optical depth. Differences are based on model simulations (Streamer) for two cloud-surface temperature relationships and for two cloud water contents (g m^{-3}).

The vertical location of the cloud, expressed as the cloud pressure, is determined by searching the temperature profile from the tropopause (or top of profile if below the tropopause) down. With this scheme, if a cloud has a temperature that could be either within or above an inversion, it will be placed below, i.e., closer to the surface (arbitrary). The physical thickness and cloud base height are determined from the cloud top height, the optical thickness, and an assumed cloud water content of 0.2 g m^{-3} for liquid clouds and 0.07 g m^{-3} for ice clouds.

3.11.2 Numerical Strategy

Not applicable.

3.11.3 Calculations

The AVHRR/VIIRS channel 4 brightness temperature, the clear sky brightness temperature (not corrected for the atmosphere), and the visible cloud optical depth are input to the algorithm. Cloud temperature is calculated as described above, and the temperature is located in a temperature profile (input model data) to retrieve the cloud top pressure.

3.11.4 Look-Up Table Description

There are no look-up tables for the cloud top temperature/pressure algorithm.

3.11.5 Parameterization

There are no parameterizations for the cloud top temperature/pressure algorithm.

3.12 Theoretical Description: Radiative Fluxes and Cloud Forcing

3.12.1 Physical and Mathematical Description

Upwelling and downwelling shortwave and longwave fluxes at the surface are computed with a neural network trained to simulate a radiative transfer model. The neural network, called FluxNet (Key and Schweiger, 1998), is also available as a stand-alone program. The radiative transfer model that FluxNet is trained to simulate is Streamer Key and Schweiger, 1998). FluxNet v4.0 is used in CASPR. Relative differences between the neural network and the radiative transfer model for surface radiative fluxes are shown in Figure 16. Errors in top-of-atmosphere fluxes are similar. FluxNet is 100 to 10,000 times faster than Streamer, and is nearly as accurate. See the web pages at http://stratus.ssec.wisc.edu for more information.

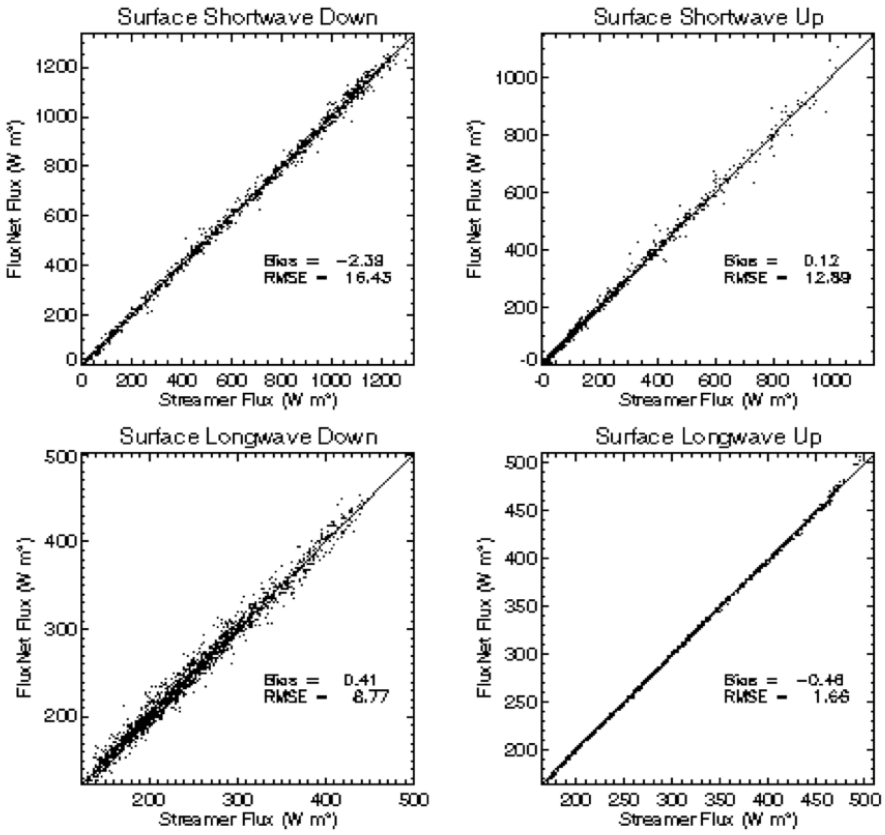

Figure 16. Comparison of FluxNet and Streamer fluxes for a wide range of atmospheric conditions.

The cloud radiative effect, more commonly called "cloud forcing", is computed from the net shortwave and longwave fluxes at the surface and TOA. It is defined as

$$CF_{\lambda,z} = \int_0^{A_c} \frac{\partial F_{\lambda,z}}{\partial a} da = F_{\lambda,z}(A_c) - F_{\lambda,z}(0)$$

where $F_{\lambda,z}$ is the net flux (W m^{-2}) for shortwave or longwave radiation at the surface and A_c is the cloud fraction in the scene. The net flux is equal to the downwelling minus the upwelling fluxes. Because pixels are assumed to be either completely cloudy or completely clear, the right side of the equation is simply the net flux (shortwave or longwave) for a cloudy pixel minus the net flux if the pixel were clear. The clear sky net flux for cloudy pixels is calculated with FluxNet by simply setting the cloud fraction to zero and other cloud properties to values used in training FluxNet for clear sky conditions. Analogous to net radiation, the all-wave net cloud forcing can be calculated from

$$CF_z = CF_{shortwave} + CF_{longwave}$$

3.12.2 Numerical Strategy

Not applicable.

3.12.3 Calculations

The surface and cloud parameters described earlier in this document are input to FluxNet, which calculated the surface and TOA radiative fluxes and cloud radiative forcing. AVHRR/VIIRS channel information is not used.

3.12.4 Look-Up Table Description

There are no look-up tables for radiative flux retrieval.

3.12.5 Parameterization

There are no parameterizations for the radiative flux retrieval, other than the fact that FluxNet is itself a parameterization of a radiative transfer model.

4. Test Datasets and Outputs

4.1 Test Input Datasets

The primary input dataset for the generation of Polar Pathfinder - Extended is Polar Pathfinder FCDR. Two examples of Polar Pathfinder FCDR are shown in Figures 17 and 18. Polar Pathfinder FCDR is described in detail in a separate C-ATBD.

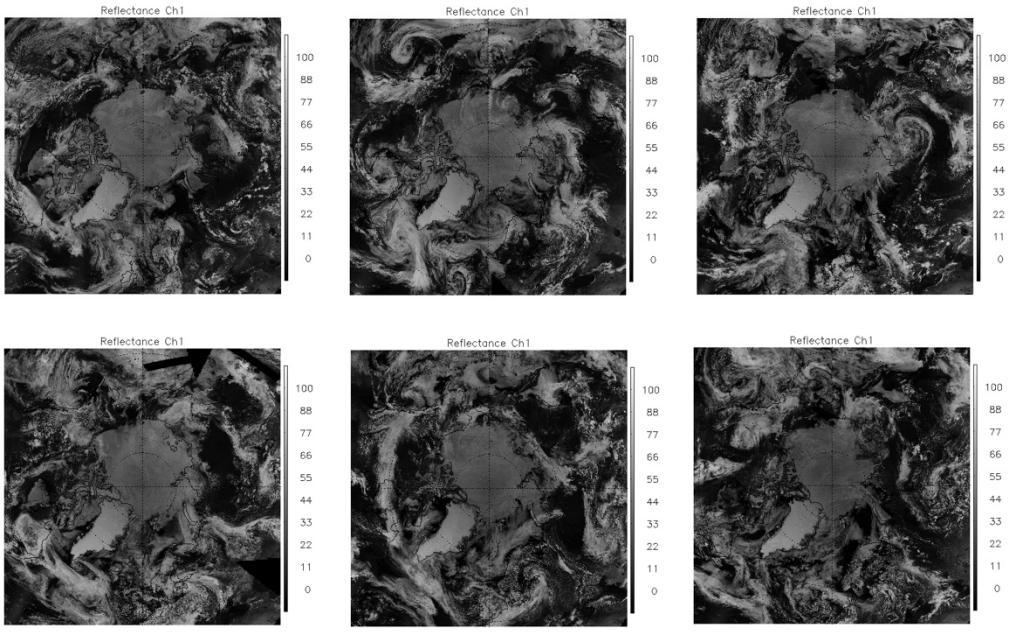

Figure 17: Polar Pathfinder FCDR channel 1 reflectance (%) at 1400 SLT of north pole on July 1st of the year 1982, 1986, 1989, 1996, 2002, and 2007.

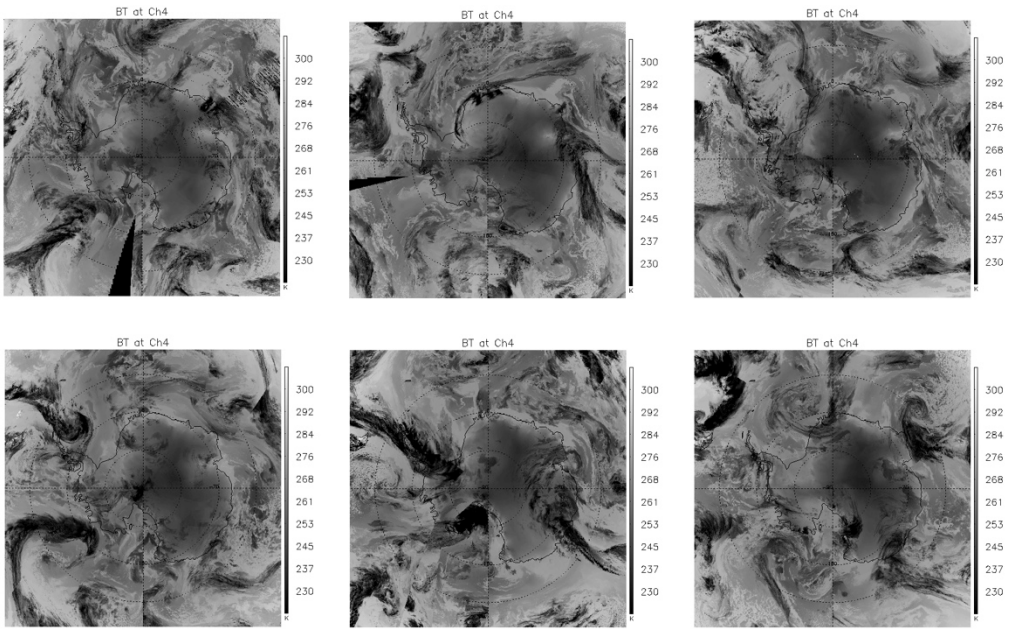

Figure 18: Polar Pathfinder FCDR channel 4 BT (K) at 1400 SLT of south pole on January 1st of the year 1982, 1986, 1989, 1996, 2002, and 2007.

4.2 Test Output Analysis

4.2.1 Reproducibility

Reproducibility is monitored and ensured by three methods. Extraction of validation matchups during reprocessing, comparison to same day reference data from other resources like a Pan-Arctic Ice-Ocean Modeling and Assimilation System (PIOMAS) (Zhang and Rothrock, 2001, 2003) and CryoSat-2, and finally trend analysis of the product with time. An example is provided here only for sea ice thickness (SIT).

For each day or month, a vector of zonal averages of SIT data can be computed. When the SIT time series are complete, these vectors are assembled to construct a Hovmöller diagram to ensure consistency of the SIT CDR. At the end of a given processing run, a Hovmöller diagram is produced that allows trends in latitude and time to be analyzed.

4.2.2 Precision and Accuracy

To estimate the performance of the OTIM, we have used the comprehensive numerical model simulations, submarine and moored Upward Looking Sonar (ULS) measurements, and meteorological station measurements to assess and validate the OTIM. Figure 19 shows an example of OTIM retrieved sea ice thickness with APP-x data in comparison with PIOMAS simulated sea ice thickness for March 21, 2014.

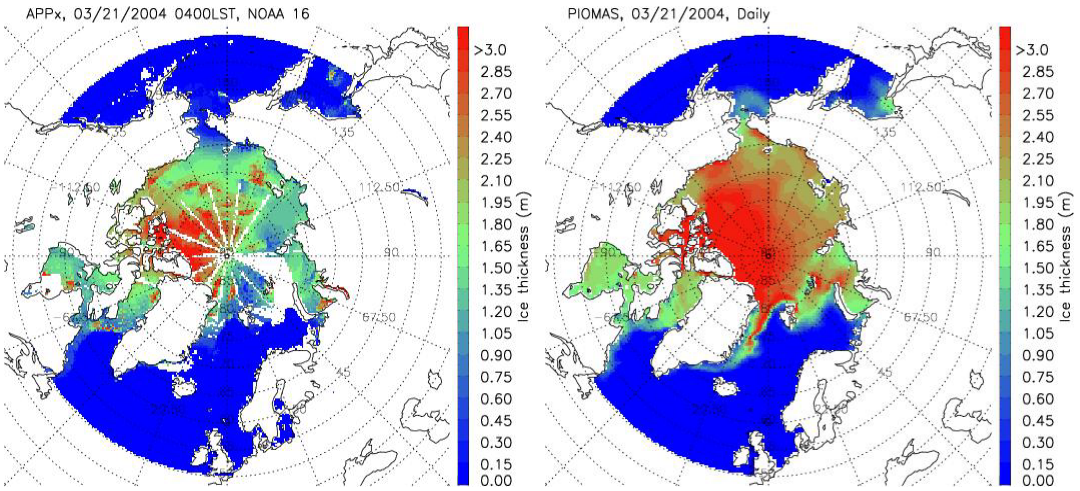

Figure 19. OTIM retrieved ice thickness with Polar Pathfinder - Extended data (left) and PIOMAS simulated ice thickness (right) for March 21, 2004 under all -sky condition.

Table 10, 11, and 12 list the comparisons of OTIM retrieved sea ice thickness with submarine measurements, mooring site measurements, and stations measurements, respectively, in terms of sea ice thickness mean, bias mean, bias absolute mean, bias standard deviation, and accuracy.

Table 10. OTIM validation results against submarine measurements made during Scientific Ice Expeditions (SCICEX-99) in 1999.

	OTIM	Submarine
Thickness Mean (m)	1.73	1.80
Bias Mean (m)	-0.07	
Bias Absolute Mean (m)	0.31	
Bias Standard Deviation	0.42	
Accuracy	83%	

Table 11. OTIM validation results against mooring measurements made from Beaufort Gyre Exploration Project (BGEP) over 2003-2004.

Mooring Location OTIM	Thickness mean (m)	Bias mean (m)	Bias absolute mean (m)
Site A (75°0.499'N, 149°58.660'W)	1.24	-0.02 (-1.2%)	0.19 (15.3%)
OTIM	1.22		

Site B (78°1.490'N, 149°49.203'W)	1.32	-0.15 (-11.4%)	0.29(21.9%)
OTIM	1.17		
Site C (76°59.232'N, 139°54.562'W)	1.32	-0.12 (-9.1%)	0.28 (21.2%)
OTIM	1.20		
ALL MOORING AVERAGE	1.29	-0.09 (-6.9%)	0.25 (19.4%)
OTIM AVERAGE	1.20		

Table 12. OTIM validation results against station measurements made at 8 Canadian meteorological stations starting from 2002 at the Canadian Ice Service (CIS)

OTIM Station Name	OTIM ALERT LT1	OTIM ALERT YLT	OTIM CAMBRIDGE BAY YCB	OTIM CORAL HARBOUR YZS	OTIM EUREKA WEU	OTIM HALL BEACH YUX	OTIM RESOLUTE YRB	OTIM YELLOWKNIFE YZF
Thickness Mean (m)	1.17 1.23	1.21 1.26	1.48 1.51	1.17 1.20	1.36 1.54	1.37 1.46	1.21 1.50	0.91 0.93
Bias Mean (m)	-0.06 (-4.8%)	-0.06 (-4.8%)	-0.04 (-2.6%)	-0.03 (-2.5%)	-0.18 (-11.7%)	-0.07 (-4.8%)	-0.29 (-19.3%)	-0.01 (-1.1%)
Bias absolute Mean (m)	0.14 (11.4%)	0.16 (12.7%)	0.58 (38.4%)	0.32 (26.7%)	0.27 (18.0%)	0.32 (32.0%)	0.31 (20.7%)	0.31 (33.3%)

4.2.3 Error Budget

The Polar Pathfinder - Extended data set is created from Polar Pathfinder FCDR data set that is based on the AVHRR/VIIRS 5 channel data. The uncertainties in AVHRR/VIIRS channel data will inevitable propagate into Polar Pathfinder – FCDR data set, and eventually affect Polar Pathfinder - Extended data set as well. Table 13 lists the estimated AVHRR 5 channel estimated uncertainties from different authors. Brest and Rossow (1997) estimated the uncertainties for AVHRR five channels for both visible and infrared channels.

Table 13. Relative uncertainties in AVHRR channels reported in the literature.

	Visible Channels (1, 2)	Thermal Channels (3, 4, 5)
Rao and Chen (1994, 1995, 1999)	0.7% (1), 1.5% (2)	---
Walton et al. (1998)	---	0.37 K, 0.15 K and 0.17 K.
Brest and Rossow (1997)	±3-5%	±1-2 K

Most of APP-x parameters were compared with field campaign and meteorological station measurements as shown in Table 14 in terms of bias and uncertainty (root-mean-square error) for quantitative information of error budget.

Table 14. Biases and uncertainties (root-mean-square error) for Polar Pathfinder - Extended

variables.

Quantity*	***Bias**#*	***RMSE**$*
Surface temperature	0.20 K	1.98 K
Surface broadband albedo	-0.05 (absolute)	0.10 (absolute)
Downwelling shortwave radiation flux at the surface	9.8 W/m^2	34.4 W/m^2
Downwelling longwave radiation flux at the surface	2.1 W/m^2	22.4 W/m^2
Upwelling shortwave radiation flux at the surface	4.4 W/m^2	26.6 W/m^2
Upwelling longwave radiation flux at the surface	1.9 W/m^2	9.4 W/m^2
Cloud fraction	0.14 (absolute)	0.26 (absolute)

**: Satellite-derived quantities are for the 25 x 25 km^2 area centered on the SHEBA ship.*
Bias is defined as difference between satellite-derived quantities and SHEBA ship measurements.
RMSE stands for Root Mean Square Error.

In estimation of ice thickness by using the OTIM, many factors affect the accuracy of ice thickness. The uncertainties from all of the input controlling variables in the OTIM will finally propagate into ice thickness through the ways of parameterizations and model algorithms. In the OTIM model we used parameterization schemes as described in previous sections to calculate radiative fluxes. Therefore in essence, ice thickness is actually the function of 12 controlling variables that are ice and snow broadband albedo (α_s), ice transmittance (i_0), surface downwelling shortwave radiation flux (F_r), surface skin and air temperatures (T_s, T_a), surface air pressure (P_a), surface air relative humidity (R), ice temperature (T_i), wind speed (U), cloud amount (C), snow depth (h_s), and residual heat flux (F_a).

$$\hat{h}_i = f(\hat{\alpha}_s, \hat{i}_0, \hat{F}_r, \hat{T}_s, \hat{T}_i, \hat{T}_a, \hat{P}_a, \hat{R}, \hat{U}, \hat{C}, \hat{h}_s, \hat{F}_a) \tag{4.1}$$

where the variables with carets "^" stand for the variables with estimated values, other than the variables with "true" values. Then the partial derivative of ice thickness against each of the controlling variables can be used for the calculation of the sensitivity of the ice thickness to the error in the controlling variable.

Tables 15 and 16 list the controlling variables used in ice thickness sensitivity study for daytime and nighttime cases with aforementioned uncertainties in controlling variables and their impacts for typical ice thickness of 1 meter.

Table 15. Sensitivity of ice thickness estimates to uncertainties in the controlling variables during daytime case with reference ice thickness of 1 meter.

Name	*Ref. Value*	*Error (Dx)**	*IceThk_Dh**	*IceThk_Dh/h*	*IceThk_Dh/Dx*
T_s *(K)*	253.23	+2.000 -2.000	-0.235 +0.245	-0.235 +0.245	-0.117 -0.122
T_i *(K)*	253.23	+5.000 -5.000	-0.008 +0.008	-0.008 +0.008	-0.002 -0.002
h_s *(m)*	0.20	+0.100 -0.100	-0.654 +0.654	-0.654 +0.654	-6.544 -6.544
R (%)	90.00	+9.000 -9.000	+0.024 -0.024	+0.024 -0.024	+0.003 +0.003
U (m/s)	5.00	+1.000 -1.000	+0.316 -0.208	+0.316 -0.208	+0.316 +0.208
P_a *(hPa)*	1000.00	+50.00 -50.00	+0.066 -0.063	+0.066 -0.063	+0.001 +0.001
α_s *(0~1)*	0.85	+0.100 -0.100	-0.757 +2.195	-0.757 +2.195	-7.566 -21.953
T_r *(0~1)*	0.05	+0.050 -0.050	-0.086 +0.092	-0.086 +0.092	-1.711 -1.848
F_r *(w/m²)*	101.44	+20.288 -20.288	+0.395 -0.295	+0.395 -0.295	+0.019 +0.015
F_a *(w/m²)*	0.00	+2.000 -2.000	-0.212 +0.260	-0.212 +0.260	-0.106 +0.130
C (0~1)	0.50	+0.250 -0.250	+0.297 -0.639	+0.297 -0.639	+1.189 +2.555

**Dx stands for the uncertainty of the controlling variable, IceThk_Dh is the corresponding sea ice thickness uncertainty, and h is the reference sea ice thickness that is 1 m.*

Table 16. Sensitivity of ice thickness estimates to uncertainties in the controlling variables during nighttime case with reference ice thickness of 1 meter.

Name	*Ref. Value*	*Error (Dx)*	*IceThk_Dh*	*IceThk_Dh/h*	*IceThk_Dh/Dx*
T_s *(K)*	241.09	+2.000 -2.000	-0.172 +0.179	-0.172 +0.179	-0.086 -0.090
T_i *(K)*	241.09	+5.000 -5.000	-0.008 +0.008	-0.008 +0.008	-0.002 -0.002
h_s *(m)*	0.20	+0.100 -0.100	-0.667 +0.667	-0.667 +0.667	-6.666 -6.666
R (%)	90.00	+9.000 -9.000	+0.006 -0.006	+0.006 -0.006	+0.001 +0.001
U (m/s)	5.00	+1.000 -1.000	+0.166 -0.133	+0.166 -0.133	+0.166 +0.133
P_a *(hPa)*	1000.00	+50.00 -50.00	+0.043 -0.041	+0.043 -0.041	+0.001 +0.001
F_a *(w/m²)*	0.00	+2.000 -2.000	-0.137 +0.155	-0.137 +0.155	-0.068 0.078
C (0~1)	0.50	+0.250 -0.250	+0.248 -0.476	+0.248 -0.476	+0.992 +1.903

5. Practical Considerations

5.1 Numerical Computation Considerations

Polar Pathfinder - Extended is implemented sequentially, as many there are a number of parameter dependencies. For example, the calculation of ice surface temperature requires a cloud mask, and the calculation of radiative fluxes and cloud forcing requires all cloud and surface properties (Figure 2).

The Polar Pathfinder - Extended effective pixel size of 25 km, which is based on sampling the 5 km Polar Pathfinder – FCDR data rather than averaging, was chosen for computational reasons only. Generating a 5 km Polar Pathfinder - Extended product is possible, but would be computationally time consuming.

5.2 Programming and Procedural Considerations

Not applicable.

5.3 Quality Assessment and Diagnostics

The following procedures are recommended for diagnosing the performance of the Polar Pathfinder - Extended:

- Monitor the percentage of pixels retrieved for ice thickness, and check the value uniformity over the small and smooth area without cracks, melting ponds, and leads.
- Periodically image the individual test results to look for artifacts or non-physical behaviors.
- Maintain a close communication and/or collaboration with users using the sea ice thickness product in their studies.

5.4 Exception Handling

The Polar Pathfinder - Extended processing includes checking the validity of input data (APP/VPP) before using it. The main processing system (CASPR) flags any pixels with missing geo-location or viewing geometry information, or out-of-range reflectances or brightness temperatures.

5.5 Algorithm Validation

In this section algorithm biases and uncertainties (root-mean-square differences) are estimated through comparisons of satellite retrievals and in situ measurements.

Surface Temperature

Comparisons with SHEBA surface observations were done by inverting measurements of the upwelling longwave flux to obtain temperature. Details are given in Key et al. (1997). An example of the comparison is shown in Figure 20. Results over all-sky conditions (i.e., clear and cloudy) yielded a bias (mean error) of –1.6 K and a root-mean-square-error (RMSE) of 6 K for the all-sky surface temperature. A negative bias indicates that the satellite retrieval is less than the surface observation. Comparisons to three International Arctic Buoy Program (IABP) buoys located from approximately 20 km to 450 km from the SHEBA icebreaker Des Groseilliers in April-July 1998 show that the AVHRR temperatures track the buoy temperatures quite well, with mean monthly differences typically less than 2 K. Retrievals for clear sky conditions have much smaller uncertainties than for all-sky conditions, on the order of -0.3 K for the bias and 1-2 K for the RMSE (Key et al., 1994).

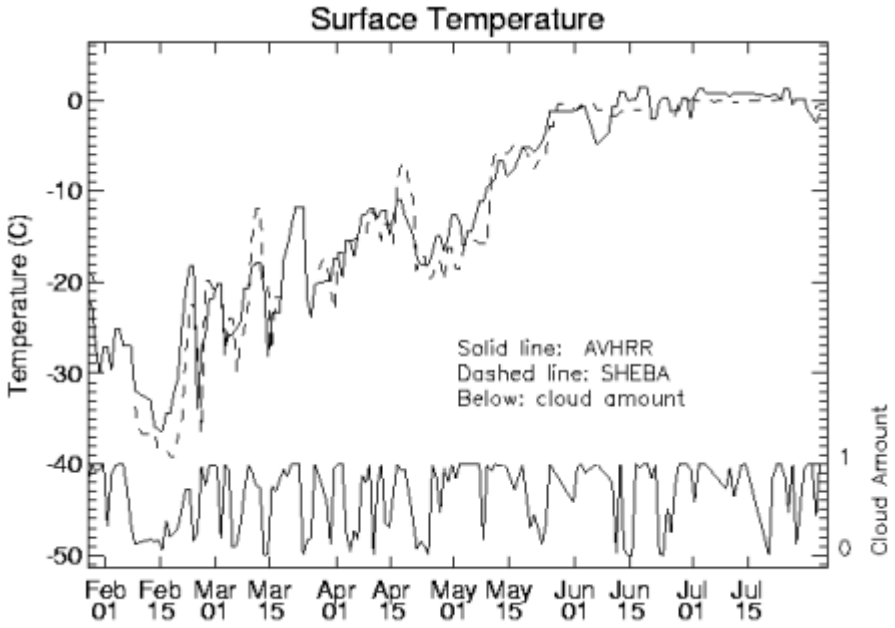

Figure 20. Comparison of satellite-derived and surface measurements of the surface skin temperature during SHEBA. Cloud amount is also shown.

Surface Albedo

Measurements of the upwelling and downwelling shortwave flux measured at the SHEBA camp were used to compute an all-sky albedo. Satellite-derived and surface measurements are shown in Figure 21. This comparison yields a bias of –0.028 and a RMSE of 0.08 for the all-sky surface albedo. Retrievals for clear sky conditions have smaller uncertainties than for all-sky conditions.

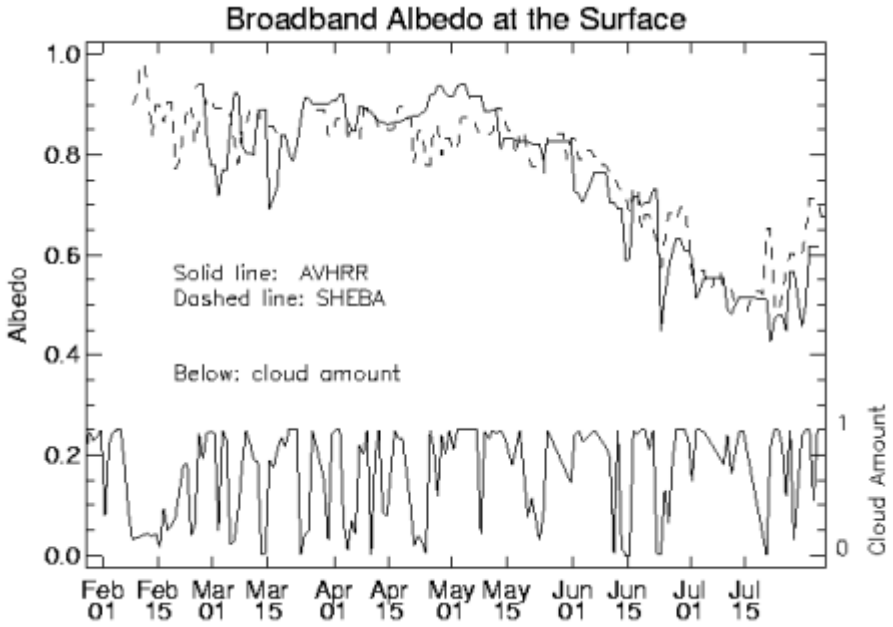

Figure 21. Comparison of satellite-derived and surface measurements of the surface broadband albedo during SHEBA. Cloud amount is also shown.

Cloud Detection

Cloud amount at the SHEBA camp is based on three-hourly synoptic observations (human observer). Comparisons with satellite-derived cloud amount for 25 x 25 km area centered on the SHEBA ship (not shown) from September 1997 through August 1998 yield a bias of 0.1 and a RMSE of 0.3. Additional details are given in Key et al. (2001).

Cloud Particle Phase

The Depolarization and Backscatter Unattended Lidar (DABUL) instrument was deployed as part of SHEBA. Small raindrops, water cloud droplets, and fog are considered spherical and have depolarization ratios that theoretically approach 0. Non-spherical particles such as ice crystals and snowflakes contain a cross-polarized component produced by internal reflections and refractions and can exhibit depolarization ratios greater than 0.30. By data point inspection and comparisons with the microwave radiometer liquid water column measurements, it was determined that DABUL depolarization values of less than 0.11 indicate liquid water phase.

Figure 22 gives a comparison of AVHRR-derived cloud phase and lidar depolarization ratio during the SHEBA year. The lidar results are for the highest altitude layer detected. Multilayer, multiphase cases were excluded from the analysis. The AVHRR results are for a 50 x 50 km area around the lidar location were used, but only for scenes with a cloud fraction of at least 0.6 (60%). The AVHRR phase labeling is zero for water and one for ice; intermediate values correspond to scenes with both phases present in varying proportions. The figure illustrates that for homogeneous scenes there is almost perfect agreement

between the lidar and satellite determinations of phase; i.e., all cases labelled as water (ice) cloud by the AVHRR algorithms, day or night, are also labelled as water (ice) cloud by the lidar method. For the cases where the AVHRR algorithm found both phases present but more water than ice cloud - as indicated by an area average phase value less than 0.5 - the lidar cloud type was usually water. The results for the cases with more ice than water cloud show a similar pattern. Overall the satellite retrievals of cloud particle phase have an accuracy of approximately 95% (Key and Intrieri, 2000).

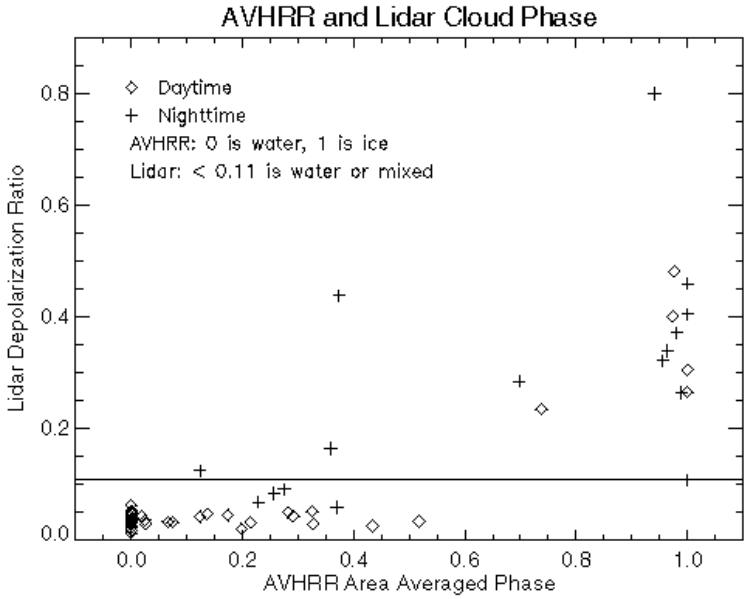

Figure 22. Cloud particle phase from the AVHRR and lidar depolarization ratio during the SHEBA year. Depolarization ratios less than 0.11 are primarily water or mixed-phase clouds. The AVHRR results use a value of zero for water and one for ice; intermediate values correspond to scenes with both phases present.

Cloud Optical Depth and Particle Size

Cloud optical depth and particle size retrievals have not been examined in detail due to the lack of in situ measurements. Some comparisons have been done with aircraft observations during SHEBA, particularly with the Canadian National Research Council (NRC) Convair. The effective radius for water (liquid) clouds from the AVHRR were comparable to those measured by the Convair, typically within 1-2 μm for clouds with effective radii in the 8-10 μm range. For ice clouds the differences are larger, on the order of 10 μm for particles with effective "radii" in the range of 30-100 μm (Gultepe et al., 2003). Figure 23 provides one example from SHEBA.

Cloud Top Pressure

Cloud top pressure is currently being validated with SHEBA lidar and radar measurements. Figure 24 shows the monthly mean cloud top pressure estimated with data from the TIROS Operational Vertical Sounder (TOVS), the AVHRR, and surface-based lidar. The two satellite

estimates are similar even though the retrieval methods are very different. The lidar estimate is considerably higher (estimated cloud top is at a lower altitude) during the summer, most likely because summertime clouds tend to be thicker on average, and the lidar cannot penetrate to the tops of clouds with optical thicknesses larger than approximately 3. It is difficult to provide an uncertainty with this limited comparison, but a value of 50-75 mb is probably reasonable.

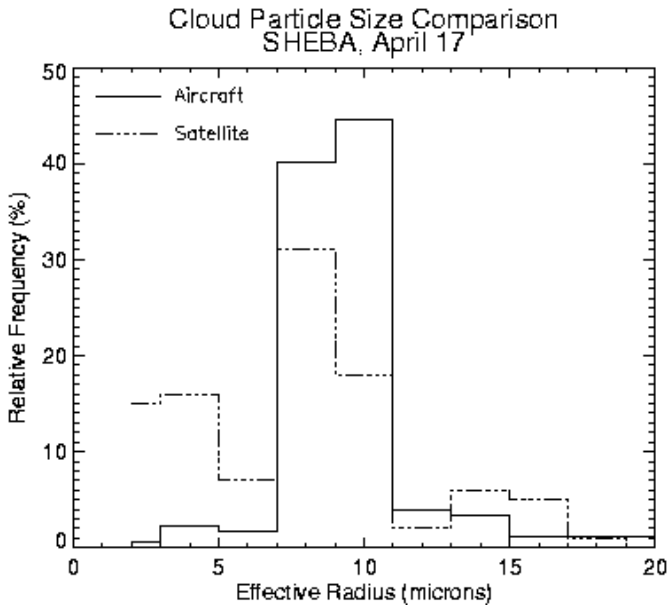

Figure 23. Relative frequency distribution of satellite-derived and aircraft measurements of liquid cloud particle effective radius for one case study from SHEBA.

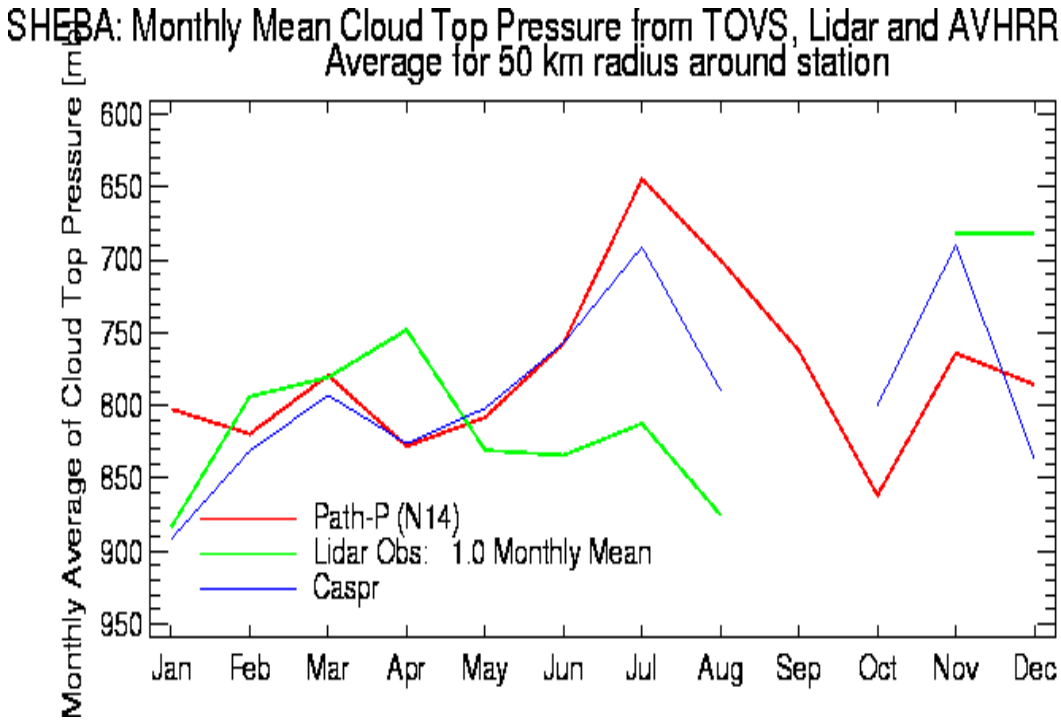

Figure 24. Monthly mean cloud top pressure from TOVS, AVHRR, and lidar during SHEBA.

Radiative Fluxes

Radiative fluxes are calculated with the neural network procedure called FluxNet. Root mean square differences between the neural network and the radiative transfer model for downwelling shortwave and longwave fluxes at the surface are on the order of 2-3% with biases near zero. Comparisons of instantaneous satellite-derived surface fluxes with SHEBA surface measurements yield a bias of 9.8 W m^{-2} and an RMSE of 34.4 W m^{-2} for downwelling shortwave radiation. For the downwelling longwave flux the bias and RMSE are 2.1 and 22 W m^{-2}, respectively. Figure 25 shows the results for SHEBA.

Comparisons of monthly mean values with measurements at Neumayer Station, Antarctica show differences of less than 10 W m^{-2} for the net shortwave flux and less than 8 W m^{-2} for the net longwave flux. For South Pole Station the longwave results are similar but the shortwave differences are somewhat higher. Figure 26 shows the results for Neumayer Station. See Pavolonis and Key (2003) for more information.

Key et al. (1997) address the combined uncertainties in satellite estimates of the surface radiation fluxes from a statistical perspective. The propagation of errors in the individual surface and cloud property retrievals is assessed as a function of the individual errors and the sensitivity of surface fluxes to changes in each variable. The method produced uncertainties in the range of 30-40 W m^{-2} for the downwelling shortwave flux, 9-15 W m^{-2} for the downwelling longwave flux, and 20-30 W m^{-2} for the net flux.

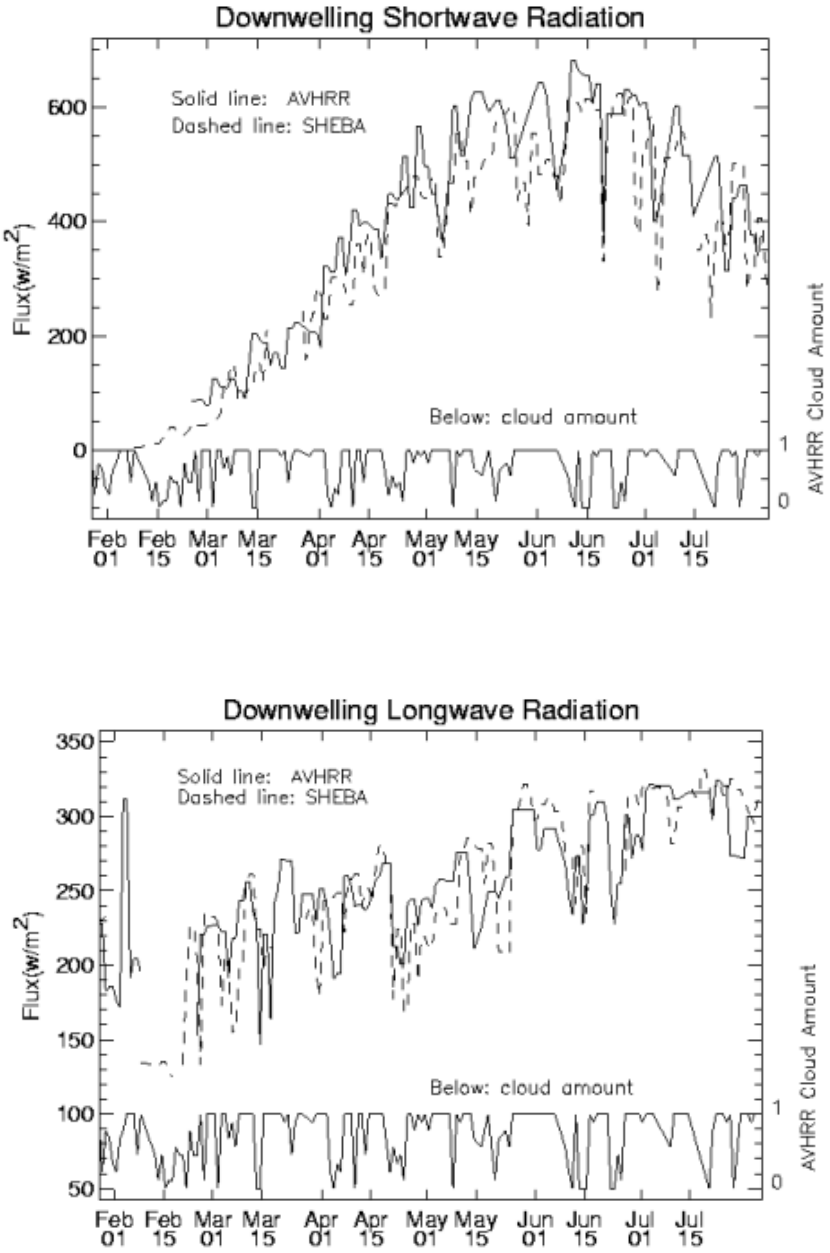

Figure 25. Comparison of satellite-derived and surface measurements of the downwelling shortwave flux at the surface (top) and the downwelling longwave flux at the surface (bottom). Cloud amount is also shown.

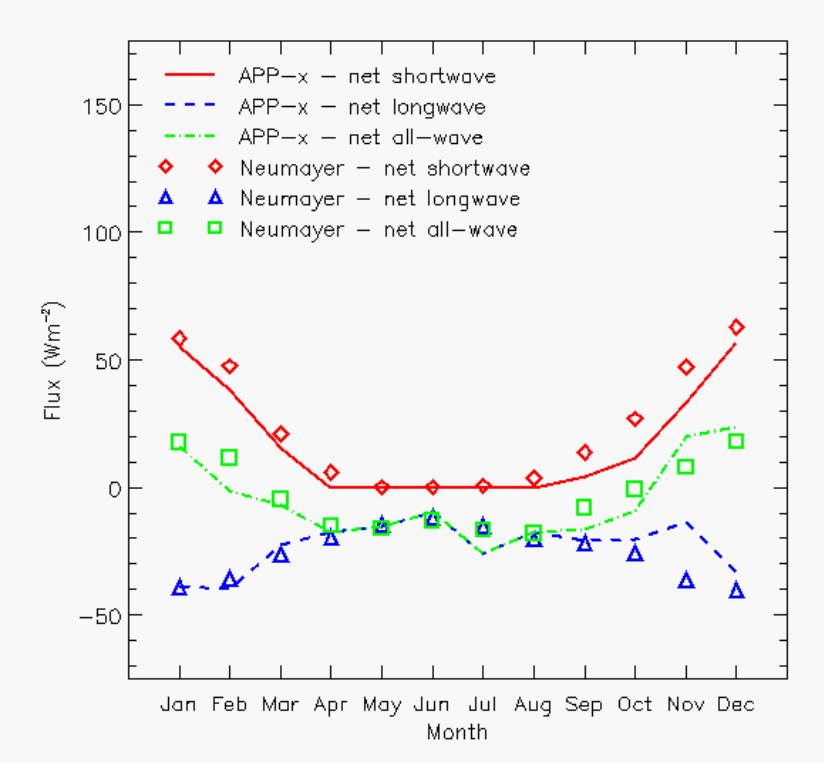

Figure 26. Comparison of monthly mean satellite-derived (APP-x) and surface measurements of the net radiative fluxes at Neumayer Station, Antarctic.

Day-Night Differences

Some algorithms use different spectral channels in the presence/absence of sunlight. Cloud detection, optical depth, effective radius, and particle phase all take advantage of reflective channels during the day. How consistent are the results for daytime and nighttime retrievals? Because these algorithms all use the AVHRR 3.7 μm channel in both day and night retrievals, a portion of the spectrum that includes both emitted thermal and reflected solar radiation, it is not possible to test the day-night differences simultaneously. Instead we provide the validation information detailed in the previous sections, and a few illustrations of retrievals for images that were part dark and part sunlit. Such comparisons are, of course, qualitative. Figure 27 shows retrievals for the cloud mask, cloud optical depth, particle effective radius, and particle phase for one winter day over the Arctic. The lower latitudes are sunlit; the area above approximately 80 degrees latitude is dark. There are no obvious day-night dependencies in the retrieval results.

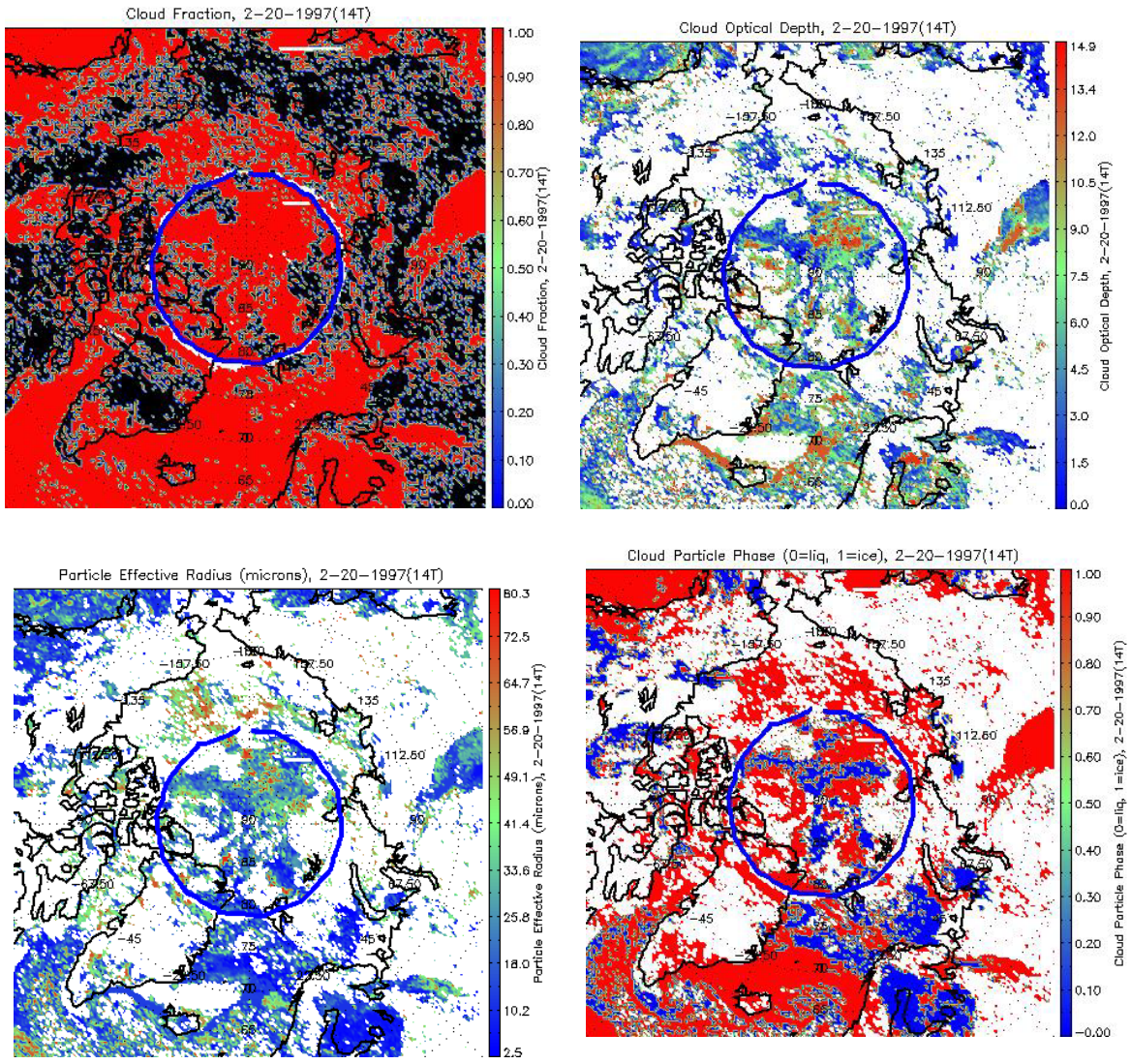

Figure 27. Retrievals for the cloud mask (upper left), visible cloud optical depth (upper right), particle effective radius (lower left), and particle phase (lower right) for one winter day over the Arctic. The lower latitudes are sunlit; the area above approximately 80 degrees latitude is dark, as denoted by the blue circle.

Validation is ongoing using data and methods such as those described above.

5.6 Processing Environment and Resources

The current computing environment is:

- Computer Hardware: MAC Pro 2 x 2.4 GHz Quad-Core Intel Xeon, 16GB memory
- Operating System: Mac OS X Lion 10.7.5
- Programming Language: IDL
- Compiler: IDL
- External Libraries: NetCDF 4.1.1
- Temporary Storage: ~500 GB for 36 years, uncompressed data for both Poles

6. Assumptions and Limitations

6.1 Algorithm Performance

The following list contains the current assumptions and proposed mitigation strategies.

- Atmospheric profile and wind speed data are available from MERRA or other reanalysis data products. In case no profile data available, it is valid assumption as used by other researchers that surface air temperature generally is about 0.5 ~ 2 degree higher than ice/snow surface temperature depending on the cloud condition, and relative humidity is about 90% over ice/snow, and wind speed of 5~10 m/s. But wind speed should be observed or simulated to guarantee to be realistic.

- Snow data including map and depth data need to be known beforehand. In case no snow data is available as it is now, climatological snow depth data or general assumption of 20 cm snow depth will be used over ice.

- Land mask maps are also needed to identify different surface types.

- All of the static ancillary data is available at the pixel level.

6.2 Sensor Performance

We assume the AVHRR/VIIRS sensors will meet their performance specifications and hence the input Polar Pathfinder FCDR product will be suitable for use in generating Polar Pathfinder - Extended. Issues with sensor calibration, particularly the drift of calibration for the visible channels, is described in the Polar Pathfinder FCDR C-ATBD.

7. Future Enhancements

Future enhancements include:

- Algorithm improvement, primarily for surface albedo, ice thickness, and cloud detection
- Possibly increase the spatial resolution from 25 km to 5 km.

8. References

Allen, Jr., R.C., P.A. Durkee, and C.H. Wash, 1990, Snow/cloud discrimination with multispectral satellite measurements. J. Appl. Meteorol., 29(10): 994-1004.

Arking, A. and J.D. Childs, 1985, Retrieval of cloud cover parameters from multispectral satellite images, J. Climate Appl. Meteorol, 24: 322-333.

Baum, B.A., R.F. Arduini, B.A. Wielicki, P. Minnis, and S.-C. Tsay, 1994, Multilevel cloud retrieval using multispectral HIRS and AVHRR data: Nighttime oceanic analysis, J. Geophys. Res., 99(D3): 5499-5514.

Bennett, T.J., 1982, A coupled atmosphere-sea ice model study of the role of sea ice in climatic predictability, *J. Atmos. Sci.*, 39, 1456-1465.

Brest, C.L., W.B. Rossow, and M.D. Roiter, 1997, Update of radiance calibrations for ISCCP. J. Atmos. Oceanic Tech., 14, 1091-1109.

Csiszar, I. and G. Gutman, 1999, Mapping global land surface albedo from NOAA AVHRR, J. Geophys. Res., 104(D6), 6215-6228.

d'Entremont, R.P., 1986, Low and mid-level cloud analysis using nighttime multispectral imagery, J. Clim. Appl. Meteorol., 25: 1853-1869.

DeAbreu, R.A., J. Key, J.A. Maslanik, M.C. Serreze, and E.F. LeDrew, 1994, Comparison of in situ and AVHRR-derived surface broadband albedo over Arctic sea ice. Arctic, 47(3): 288-297.

Dozier, J. and S.G. Warren, 1982, Effect of viewing angle on the infrared brightness temperature of snow,

Water Resources Res., 18(5), 1424-1434.

Ebert, E.E., 1987, A pattern recognition algorithm for distinguishing surface and cloud types in the polar regions, J. Climate Appl. Meteorol., 26: 1412-1427.

Ebert, E.E. and J.A. Curry, 1992, A parameterization of ice cloud optical properties for climate models, J. Geophs. Res., 97(D4): 3831-3836.

Fu, Q. and K.N.Liou, 1993, Parameterization of the radiative properties of cirrus clouds, J. Atmos.Sci., 50(13), 2008-2025.

Grenfell, T. C., 1979, The effects of ice thickness on the exchange of solar radiation over the polar oceans, *J. Glaciol.*, 22, 305-20.

Gultepe, I., G. Isaac, J. Key, T. Uttal, J. Intrieri, D. Starr, and K. Strawbridge, 2004, Dynamical and Microphysical Characteristics of Arctic Clouds Using Integrated Observations Collected Over SHEBA During the April 1998 FIRE-ACE Flights of the Canadian Convair, Meteorol. Atmos. Physics, 85, 235-263.

Gustafson, G.B. et al., 1994, Support of Environmental Requirements for Cloud Analysis and Archive (SERCAA), Phillips Laboratory, Hanscom Air Force Base, Scientific Report No. 2, PL-TR-94-2114,; 100 pp.

Hu, Y.X. and K. Stamnes, 1993, An accurate parameterization of the radiative properties of water clouds suitable for use in climate models, J. Climate, 6(4): 728-742.

Hunt, G.E., 1973, Radiative properties of terrestrial clouds at visible and infra-red wavelengths, Quart. J. Roy. Meteor. Soc., 99: 346-349.

Inoue, T., 1985, On the temperature and effective emissivity determination of semitransparent cirrus clouds by bi-spectral measurements in the 10 μm window region, J. Meteorol. Soc. Japan, 63: 88-99.

Jacobs, J.D., 1978: Radiation climate of Broughton Island. In: R. G. Barry and J. D. Jacobs, Energy budget studies in relation to fast-ice breakup processes in Davis Strait, Occas. Pap. 26,105-120. Inst. of Arctic and Alp. Res., Univ. of Colorado, Boulder, CO.

Jin, Z., K. Stamnes, and W.F. Weeks, 1994, The effect of sea ice on the solar energy budget in the atmosphere-sea ice-ocean system: A model Study, *J. Geophys. Res.*, 99, No. C12, 25,281-25,294.

Key, 2002, The Cloud and Surface Parameter Retrieval (CASPR) System for Polar AVHRR, NOAA/NESDIS/STAR, Madison, WI, available online at the http://stratus.ssec.wisc.edu.

Key, J. and A.J. Schweiger, 1998. Tools for atmospheric radiative transfer: Streamer and FluxNet. Computers and Geosciences, 24(5), 443-451.

Key, J., X. Wang, J. Stroeve, C. Fowler, 2001. Estimating the cloudy sky albedo of sea ice and snow from space. J. Geophys. Res., in press.

Key, J. and J. Intrieri, 2000, Cloud particle phase determination with the AVHRR, J. Appl. Meteorol., 36(10), 1797-1805.

Key, J. and A.J. Schweiger, 1998, Tools for atmospheric radiative transfer: Streamer and FluxNet. Computers and Geosciences, 24(5), 443-451.

Key, J., A.J. Schweiger, and R.S. Stone, 1997, Expected uncertainty in satellite-derived estimates of the high-latitude surface radiation budget. J. Geophys. Res., 102(C7), 15837-15847.

Key, J., J. Collins, C. Fowler, and R.S. Stone, 1997, High-latitude surface temperature estimates from thermal satellite data, Remote Sensing Environ., 61: 302-309.

Key, J., J.A. Maslanik, T. Papakyriakou, M.C. Serreze, and A.J. Schweiger, 1994, On the validation of satellite-derived sea ice surface temperature, *Arctic*, 47(3), 280-287.

Key, J. and M. Haefliger, 1992. Arctic ice surface temperature retrieval from AVHRR thermal channels. J. Geophys. Res., 97(D5), 5885-5893.

Key, J. and R.G. Barry, 1989, Cloud cover analysis with Arctic AVHRR, part 1: cloud detection, J. Geophys. Res., 94 (D15): 18521-18535.

Koepke, P., 1989, Removal of atmospheric effects from AVHRR albedos, J. Appl. Meteorol., 28: 1341-1348.

Li, Z. and L. Garand, 1994, Estimation of surface albedo from space: A parameterization for global application, J. Geophys. Res., 99(D4), 8335-8350.

Lin, X. and J.A. Coakley, Jr., 1993, Retrieval of properties for semitransparent clouds from multispectral infrared imagery data, J. Geophys. Res., 98: 18501-18514.

Lindsay, R.W. and D.A. Rothrock, 1994, Arctic sea ice albedo from AVHRR, J. Climate, 7(11): 1737-1749.

Maykut, G.A., and N. Untersteuner, 1971, Some results from a time-dependent thermodynamic model of sea ice, *J.G.R.*, Vol. 76, pp.1550-1575.

Nakajima, T. and M.S. King, 1990, Determination of the optical thickness and effective particle radius of clouds from reflected solar radiation measurements. Part I: theory, J. Atmos. Sci., 47(15): 1878-1893.

NOAA, 1991, NOAA Polar Orbiter Data User's Guide, U.S. Dept. of Commerce., National. Ocean. and Atmos. Admin., NESDIS, February.

Ohmura, A., 1981, Climate and energy balance of the Arctic tundra, Zürcher Geogr. Schr. 3, 448 pp., Geogr. Inst., Zürich, Switzerland.

Ou, S.C., K.N. Liou, W.M. Gooch, and Y. Takano, 1993, Remote sensing of cirrus cloud parameters using advanced very high resolution radiometer 3.7 and 10.9 μm channels, Appl. Opt., 32: 2171-2180.

Pavolonis, M. and J. Key, 2003, Antarctic cloud radiative forcing at the surface estimated from the AVHRR Polar Pathfinder and ISCCP D1 data sets, 1985-1993, J. Appl. Meteorol., 42(6), 827-840.

Rao, C.R.N., 1993, Degradation of the visible and near-infrared channels of the advanced very high resolution radiometer on the NOAA-9 spacecraft: assessment and recommendations for corrections. NOAA Technical Report NESDIS 70, U.S. Department of Commerce, 25 pp.

Rees, W.G., 1993, Infrared emissivities of Arctic land cover types, *Int. J. Remote Sensing*, 14, 1013-1017.

Rienecker, M.M., M.J. Suarez, R. Gelaro, R. Todling, J. Bacmeister, E. Liu, M.G. Bosilovich, S.D. Schubert, L. Takacs, G.-K. Kim, S. Bloom, J. Chen, D. Collins, A. Conaty, A. da Silva, et al. (2011), MERRA: NASA's Modern-Era Retrospective Analysis for Research and Applications. *J. Climate*, 24, 3624-3648, doi:10.1175/JCLI-D-11-00015.1.

Rossow, W.B., 1989, Measuring cloud properties from space: A review, J. Climate, 2: 201-213.

Rossow, W.B. and L.C. Garder, 1993, Cloud detection using satellite measurements of infrared and visible radiances for ISCCP, J. Climate, 6(12): 2341-2369.

Sakellariou, N.K., H.g. Leighton, and Z. Li, 1993, Identification of clear and cloudy pixels at high latitudes from AVHRR radiances, Int. J. Remote Sensing, 14(10): 2005-2024.

Saunders, R.W. and K.T. Kriebel, 1988, An improved method for detecting clear sky and cloudy radiances from AVHRR data, Int. J. Remote Sensing, 9(1), 123-150.

Stamnes, K., S.C. Tsay, W. Wiscombe and K. Jayaweera, 1988, Numerically stable algorithm for discrete-ordinate-method radiative transfer in multiple scattering and emitting layered media, Appl. Opt., 27: 2502-2509.

Stone, R.S., G.L. Stephens, C.M.R. Platt, and S. Banks, 1990, The remote sensing of thin cirrus cloud using satellites, lidar, and radiative transfer theory, J. Appl. Meteorol., 29(5): 353-366.

Stowe, L.L., E.P. McClain, R. Carey, P. Pellegrino, and G.G. Gutman, 1991, Global distribution of cloud cover derived from NOAA/AVHRR operational satellite data, Adv. Space Res., 11(3), 51-54.

Suttles, J.T., R.N. Green, P. Minnis, G.L. Smith, W.F. Staylor, B.A. Wielicki, I.J. Walker, D.F. Young, V.R. Taylor, and L.L. Stowe, 1988, Angular radiation models for Earth-Atmosphere system. Volume I-Shortwave radiation, NASA Reference Publication 1184, 144 pp.

Taylor, V.R. and Stowe, L.L., 1984, Atlas of reflectance patterns for uniform earth and cloud surfaces (NIMBUS-7 ERB-61 days), NOAA Technical Report NESDIS 10, U.S. Department of Commerce, 66 pp.

Toon, O.B. C.P. McKay, and T.P. Ackerman, 1989, Rapid calculation of radiative heating rates and photodissociation rates in inhomogeneous multiple scattering atmospheres, J. Geophys. Res., 94(D13): 16287-16301.

Tsay, S.-C., K. Stamnes and K. Jayaweera, 1989, Radiative energy budget in the cloudy and hazy Arctic. J. Atmos. Sci., 46: 1002-1018.

Wang, X., J. Key, and Y. Liu, 2010, A thermodynamic model for estimating sea and lake ice thickness with optical satellite data, *J. Geophys. Res.*, revision submitted, Sept. 2010.

Welch, R.M., S.K. Sengupta, A.K. Goroch, P. Rabindra, N. Rangaraj, and M.S. Navar, 1992, Polar cloud and surface classification using AVHRR imagery: An intercomparison of methods, J. Appl. Meteorol., 31: 405-420.

Yamanouchi, T., K. Suziki, and S. Kawaguchi, 1987, Detection of clouds in Antarctica from infrared multispectral data of AVHRR. J. Meteorol. Soc. Japan, 65(6): 949-961.

Zhang, J., and D.A. Rothrock, 2003, Modeling global sea ice with a thickness and enthalpy distribution model in generalized curvilinear coordinates, *Mon. Wea. Rev.*, 131(5), 681-697.

Zhang, J., and D.A. Rothrock, 2001, A thickness and enthalpy distribution sea-ice model, *J. Phys. Oceanogr.*, 31, 2986-33001.

Appendix A. Acronyms and Abbreviations

Acronym or Abbreviation	Meaning
APP	AVHRR Polar Pathfinder
APP-x	eXtended AVHRR Polar Pathfinder (APP)
AVHRR	Advanced Very High Resolution Radiometer
BGEP	Beaufort Gyre Exploration Project
CASPR	Cloud And Surface Parameter Retrieval system
C-ATBD	Climate Algorithm Theoretical Basis Document
CDR	Climate Data Record
CIMSS	Cooperative Institute for Meteorological Satellite Studies
CIS	Canadian Ice Service
CSIM	Climate Sea Ice Model
CSM	Climate System Model
EASE	Equal-Area Scalable Earth
ECMWF	European Centre for Medium-Range Weather Forecasts
EUMETSAT	European Organisation for the Exploitation of Meteorological Satellites
ESA	European Space Agency
IDL	Interactive Data Language
MERRA	Modern Era Retrospective-analysis for Research and applications
MODIS	Moderate-resolution Imaging Spectroradiometer
MSG	Meteosat Second Generation
NASA	National Aeronautics and Space Administration
NCDC	National Climatic Data Center
NCEI	National Centers for Environmental Information
NCEP	National Centers for Environmental Prediction
NESDIS	NOAA's Satellite and Information Service
NOAA	National Oceanic and Atmospheric Administration
PIOMAS	Pan-Arctic Ice-Ocean Modeling and Assimilation System
OTIM	One-Dimensional Thermodynamic Ice Model
SEVIRI	Spinning Enhanced Visible & InfraRed Imager
SIT	Sea Ice Thickness
STAR	The Center for Satellite Applications and Research
ULS	Upward Looking Sonar
UW-Madison	University of Wisconsin-Madison

VPP	VIIRS Polar Pathfinder
VPP-x	VIIRS Polar Pathfinder - Extended

Appendix B. Conductive heat flux for two-layer system with snow over ice

Consider a two-layer system, with a slab of ice overlaid by a layer of snow as shown below.

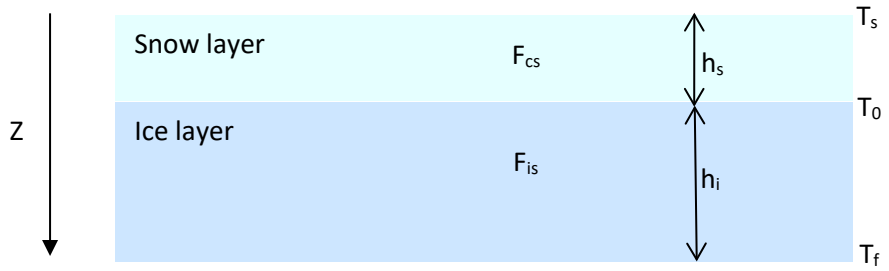

We assume the temperature gradients in the snow and ice are each linear and thus conductive heat flux is constant with depth. At the snow/ice interface, the conductive flux in the snow must equal the conductive flux in the ice, i.e., $F_{ci} = F_{cs.}$ As we define the direction to the snow/ice is positive, so we can derive the conductive heat flux for the two-layer system with a snow layer overlaid a slab of ice as shown below. Downward direction is defined positive, so $F_c=k\cdot dT/dh$, where dT is temperature difference, and dh is the snow/ice thickness.

$$F_c = k\frac{dT}{dZ}, \text{and so for the snow layer, we have } F_{cs} = k_s\frac{T_0 - T_s}{h_s}, \text{and the same for the ice slab,}$$

$$F_{ci} = k_s\frac{T_f - T_0}{h_i}, \text{ so we have } k_s\frac{T_f - T_0}{h_i} = k_s\frac{T_0 - T_s}{h_s}, \text{after series of derivation, we finally get}$$

$$T_0 = \frac{k_s h_i T_s + k_i h_s T_f}{k_i h_s + k_s h_i}, \text{therefore } F_{cs} = \frac{k_i k_s}{k_i h_s + k_s h_i}(T_f - T_s), F_c = F_{cs} = \frac{k_i k_s}{k_i h_s + k_s h_i}(T_f - T_s).$$

Appendix C. The Polar Pathfinder - Extended updates and improvements

This version 2 of the Polar Pathfinder - Extended dataset was generated with version 2 of the Polar Pathfinder – FCDR dataset along with the algorithm updates and improvements for Polar Pathfinder - Extended dataset processing as listed in Section 1.4. Therefore the changes from version 1 to version 2 in Polar Pathfinder - Extended dataset include the influences from the changes of the Polar Pathfinder FCDR version 2 dataset and the algorithm updates/improvements of the Polar Pathfinder - Extended version 2 as well.

The exclusive impacts of Polar Pathfinder FCDR version 2 changes on the Polar Pathfinder - Extended version 2 (this version) should be very small due to the adjustments of corresponding algorithms of the Polar Pathfinder - Extended dataset processing like cloud detection algorithms upon the changes in the Polar Pathfinder FCDR channel data that mainly happened in visible channels, i.e., Channel 1 & 2 (see APP C-ATBD version 2 document, reported separately). The examples below show the differences in cloud mask, surface broadband albedo, surface skin temperature, and ice thickness in Figure C-1, C-2, C-3, and C-4, respectively between two versions of the Polar Pathfinder - Extended dataset.

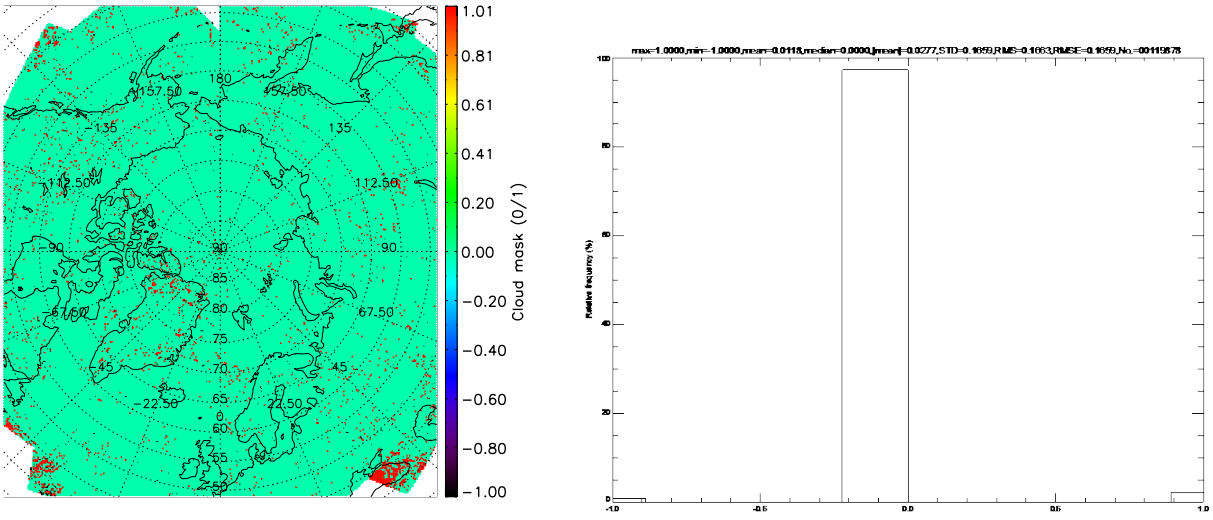

Figure C- 3: Image (left) and histogram (right) of cloud mask differences between Polar Pathfinder - Extended version 1 and Polar Pathfinder - Extended version 2 for the date of July 15,2016. In terms of the mean of absolute differences between the two Polar Pathfinder - Extended versions, cloud mask overall difference is 2.77%.

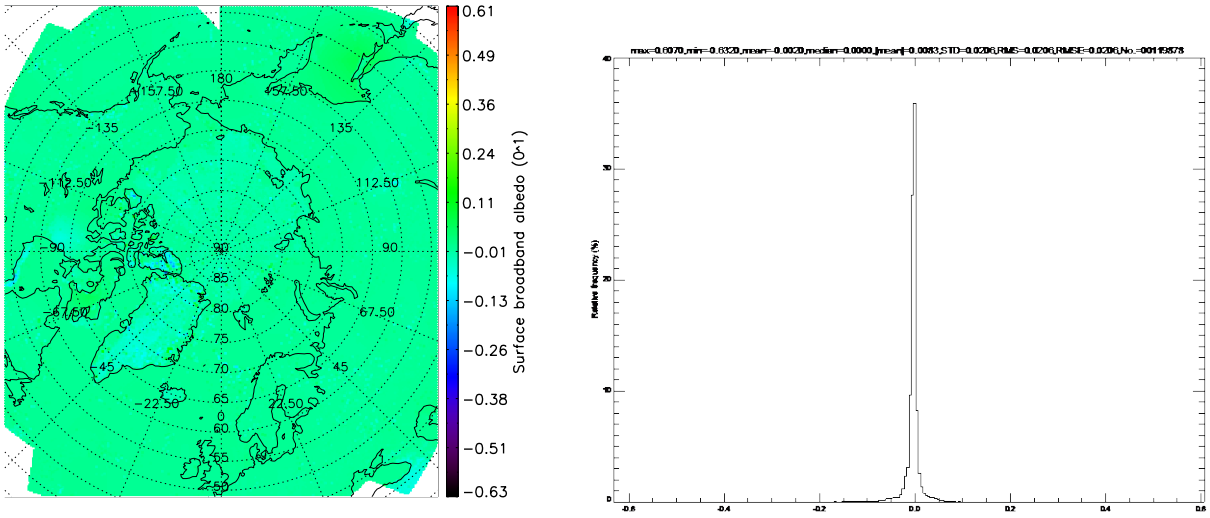

Figure C- 2: Same as Figure C-1, but for Surface broadband albedo. Surface broadband albedo overall difference is 0.83%, much less than its uncertainty. Differences could be up to 60% for few pixels because of differences in the cloud mask, (i.e., clear sky in one version and cloudy in the other version) as well as different channel 1 and 2 reflectances from the two Polar Pathfinder FCDR versions in two Polar Pathfinder FCDR versions.

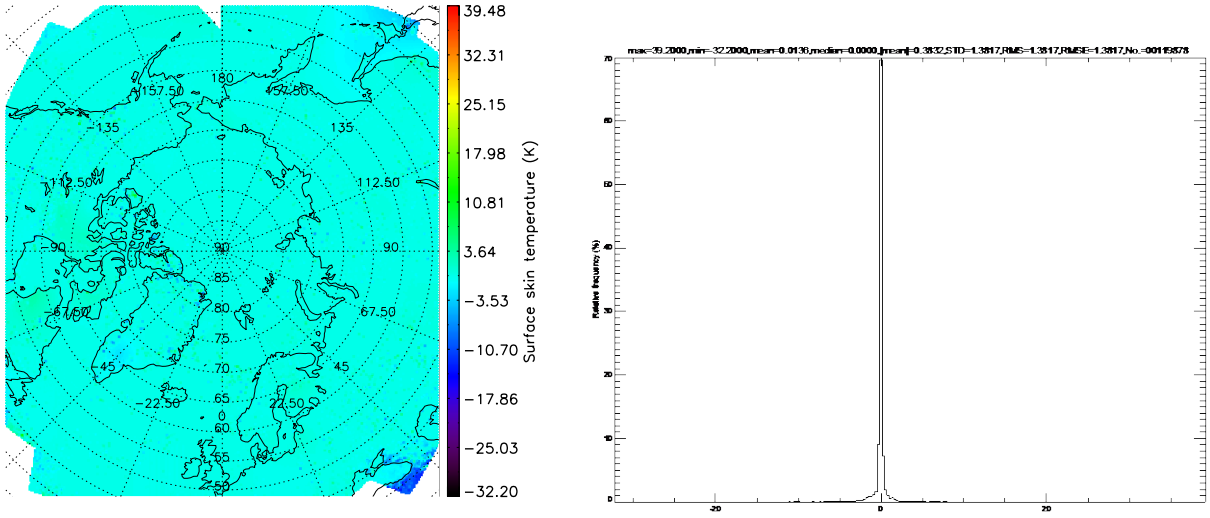

Figure C- 3: Same as Figure C-1, but for surface skin temperature. Surface skin temperature difference is 0.38 K. Differences could be up to 30 K for a few pixels due to differences in cloud mask (i.e., clear sky in one version and cloudy in the other version) as well as different channel 4 and 5 brightness temperatures from the two APP versions. Version 2 should have improved cloud mask algorithms with corrected surface type data than version 1.

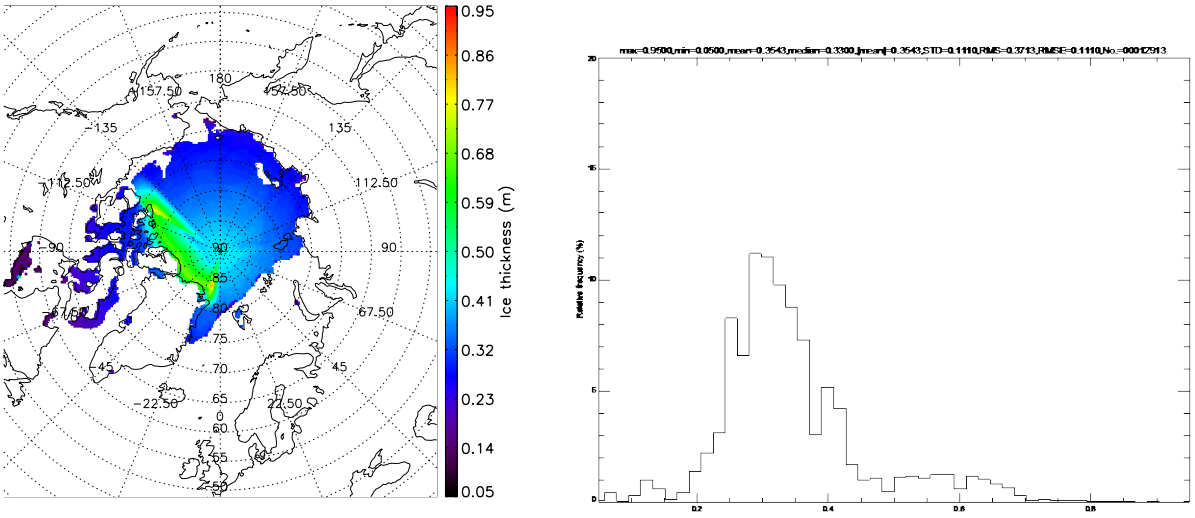

Figure C- 4: Same as Figure C-1, but for ice thickness. Ice thickness overall difference between version 2 and version 1 of Polar Pathfinder - Extended dataset is 0.35m. Differences could be up to 0.95 m along Canadian archipelago areas where ice physical dynamic processes (rafting, ridging, etc.) are now considered in version 2. Version 2 ice thickness provides an improved estimate as validated with ice thermodynamic processes (freezing and melting processes) being considered as well.

Appendix D. Intercalibration between APP-x and VPP-x

The selected VIIRS 5 bands are calibrated to NOAA-19 5 AVHRR channels to make APP and VPP compatible and consistent in value in order to apply current AVHRR channel data-based algorithms to VIIRS band data to generate VPP-x for the extension of currently APP and APP-x CDRs into VIIRS era without discontinuity and in consistence between them. To check and verify APP-x and VPP-x, they were compared to each other over overlapped locations and times to guarantee the combination of the two CDRs that can be used for climate study without problem regarding the uncertainty and consistence.

Figure D-1 shows surface broadband albedo from NOAA-19 AVHRR and VIIRS data on July 15 ,2017 at 14:00 local solar time for the Arctic region. For this case, the mean bias for the Arctic region north of 60 degrees between APP-x and VPP-x is 0.035, or 3.5%.

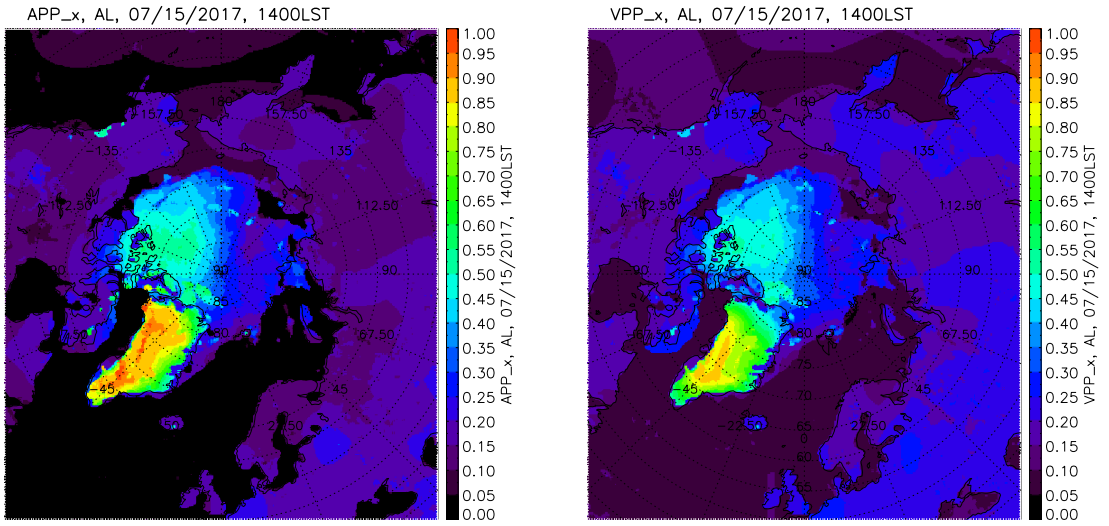

Figure D- 1: Surface broadband albedo from NOAA-19 AVHRR (left) and VIIRS (right) data on July 15 ,2017 at 14:00 local solar time for the Arctic region.

Figure D-2 shows the time series of surface broadband albedo from NOAA-19 AVHRR and VIIRS data over the year of 2017 for the Arctic region north of 60 degrees. The mean bias for the Arctic region north of 60 degrees between APP-x and VPP-x is -0.013, or 1.3%, which is less than surface broadband albedo retrieval uncertainty and reflects good match between APP-x and VPP-x in surface broadband albedo overall.

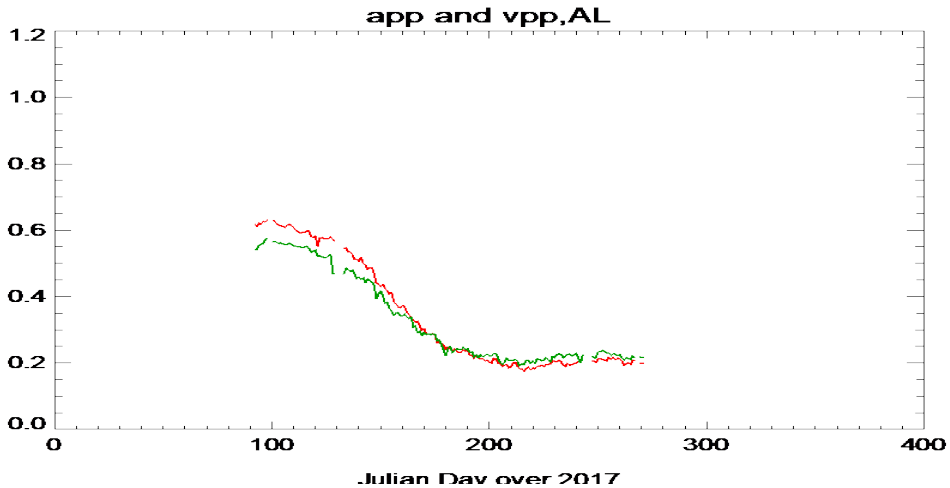

Figure D- 2: Time series of surface broadband albedo from NOAA-19 AVHRR (red) and VIIRS (green) data over the year of 2017 at 14:00 local solar time for the Arctic region north of 60 degrees.

Figure D-3 shows surface skin temperature from NOAA-19 AVHRR and VIIRS data on July 15 ,2017 at 14:00 local solar time for the Arctic region. For this case, the mean bias for the Arctic region north of 60 degrees between APP-x and VPP-x is 0.58 K.

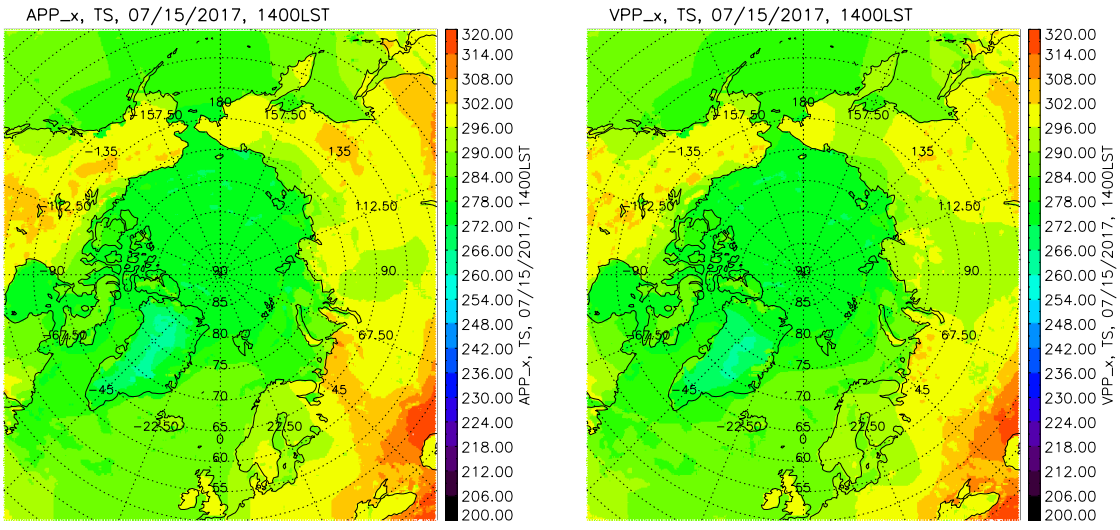

Figure D-3: Surface skin temperature from NOAA-19 AVHRR (left) and VIIRS (right) data on July 15 ,2017 at 14:00 local solar time for the Arctic region.

Figure D-4 shows the time series of surface skin temperature from NOAA-19 AVHRR and VIIRS data over the year of 2017 for the Arctic region north of 60 degrees. The mean bias for the Arctic region north of 60 degrees between APP-x and VPP-x is -0.22 K for the year of

2017, which is also less than the retrieval uncertainty and reflects good match between APP-x and VPP-x in surface skin temperature overall.

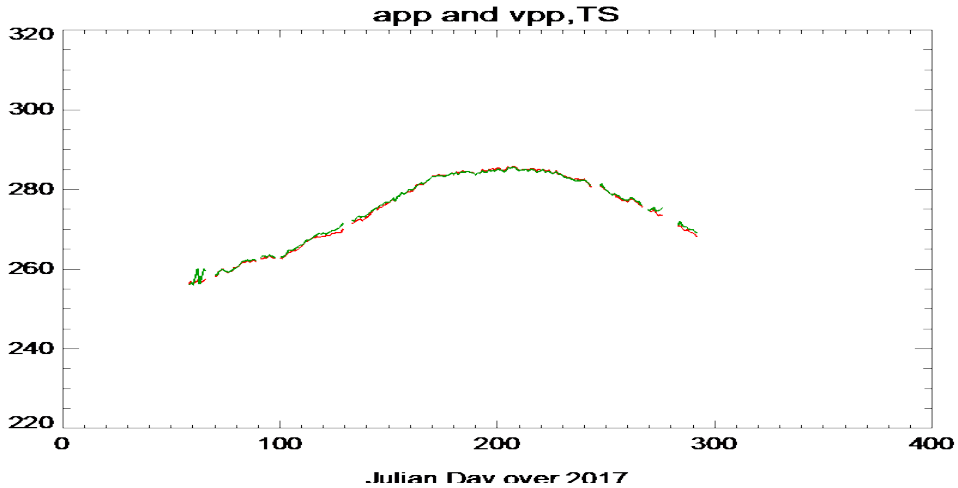

Figure D-4: Time series of surface broadband albedo from NOAA-19 AVHRR (red) and VIIRS (green) data over the year of 2017 at 14:00 local solar time for the Arctic region north of 60 degrees.

Figure D-5 shows the time series of sea ice thickness from NOAA-19 AVHRR and VIIRS data over the year of 2017 for the Arctic region north of 60 degrees. The mean bias for the Arctic region north of 60 degrees between APP-x and VPP-x is -0.028 m for the year of 2017, reflecting good match between APP-x and VPP-x in ice thickness overall.

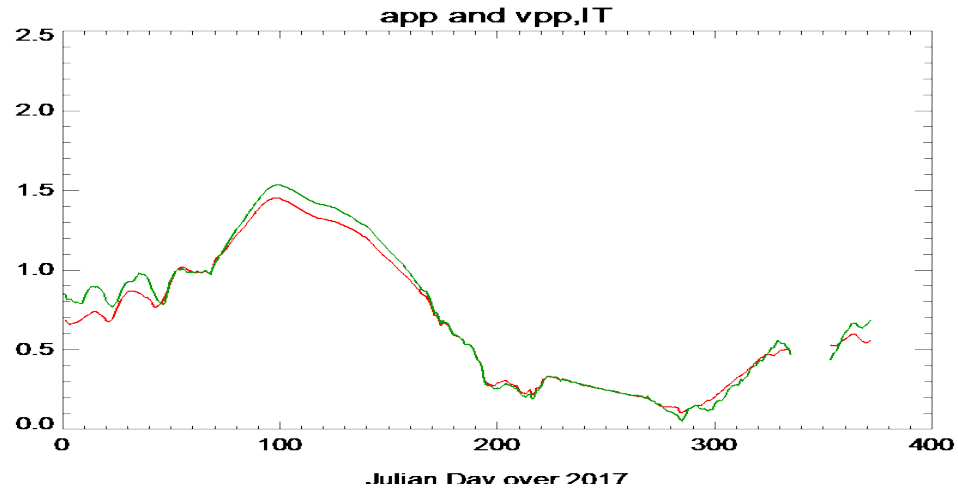

Figure D-5: Time series of sea ice thickness from NOAA-19 AVHRR (red) and VIIRS (green) data over the year of 2017 at 14:00 local solar time for the Arctic region north of 60 degrees.